

ANALYSIS OF SKYSHINE SPECTRAL MEASUREMENTS

by

Randall Robert Nason

B.S., Kansas State University, 1977

---

A MASTER'S THESIS

submitted in partial fulfillment of the  
requirements for the degree

MASTER OF SCIENCE

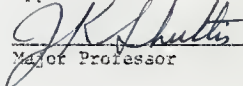
Department of Nuclear Engineering

KANSAS STATE UNIVERSITY

Manhattan, Kansas

1979

Approved:

  
Major Professor

Spec. Coll.  
LD  
2668  
.T4  
1979  
N37  
c.2

Table of Contents

	Page
LIST OF FIGURES . . . . .	iii
LIST OF PLATES . . . . .	vi
LIST OF TABLES . . . . .	vii
1.0 INTRODUCTION . . . . .	1
2.0 EXPERIMENTAL FACILITIES AND METHODS . . . . .	7
2.1 Gamma-Ray Spectroscopy System . . . . .	7
2.1.1 Choice of Spectrometer System Parameters . . . . .	8
2.1.2 Spectrometer Calibration . . . . .	11
2.1.3 System Response as a Function of Count Rate . . . . .	12
2.2 Detector Collimator Assembly . . . . .	18
2.2.1 Construction of Collimator Assembly . . . . .	19
2.2.2 NaI Crystal Positioning . . . . .	23
2.2.3 Environmental Control . . . . .	26
2.2.4 Detector Cavity/Collimator Performance . . . . .	28
2.3 Source Silo and Associated Components . . . . .	37
2.3.1 Source Silo . . . . .	37
2.3.2 Collimator Wedges . . . . .	40
2.3.3 Silo Roof Shields . . . . .	42
2.3.4 Source Irradiators . . . . .	45
2.4 Measurement Procedures . . . . .	49
2.4.1 Trailer Positioning . . . . .	49
2.4.2 Spectral Quality Control . . . . .	51
3.0 SPECTRAL ANALYSIS AND COMPARISONS . . . . .	52
3.1 Data Analysis Techniques . . . . .	52
3.1.1 Spectral Characteristics . . . . .	53
3.1.2 Theory of Unfolding . . . . .	59
3.1.3 Derivation of the SEGO Method . . . . .	62
3.1.4 Description and Construction of the Response Matrix . . . . .	67
3.1.5 Determination of Gain and Zero Channel . . . . .	82
3.2 Spectral Comparisons . . . . .	84
3.2.1 Comparison of Unshielded Spectra . . . . .	84
3.2.2 Comparison of Shielded Spectra . . . . .	93
4.0 MEASUREMENT AND COMPARISON OF EXPOSURE RATES . . . . .	102
4.1 Correction of Observed Exposure Rates . . . . .	103
4.1.1 Theoretical Considerations . . . . .	103

	Page
4.1.2 Calculation of the Correction Factor $\bar{f}$ . . . . .	114
4.1.3 Correction Factor Values for the Un- Shielded Source Configuration. . . . .	123
4.1.4 Correction Factor Values for the Shielded Source Configuration . . . . .	124
4.2 Comparison of Measured and Calculated Exposure Rate Values . . . . .	126
4.2.1 Comparison of Collimated Detector Results. . . . .	127
4.2.2 Comparison of $4\pi$ Geometry Exposure Rates . . . . .	130
5.0 CONCLUSIONS AND SUGGESTIONS FOR FURTHER STUDY. . . . .	144
ACKNOWLEDGEMENT . . . . .	147
REFERENCES. . . . .	148

## List of Figures

	Page
1. Map of shielding facility. . . . .	4
2. Block diagram of gamma-ray spectrometer. . . . .	9
3. Spectrometer calibration curve . . . . .	13
4. Photopeak position as a function of total spectrum count rate. . . . .	15
5. System resolution as a function of total spectrum count rate. . . . .	16
6. Results of the "ratio test". . . . .	17
7. Dimensions of original detector cavity . . . . .	20
8. Co-60 spectrum taken with original collimator assembly . . . . .	30
9. Dimensions of modified detector cavity . . . . .	33
10. Comparison of Co-60 spectra taken with old and new collimator assembly. . . . .	34
11. Results of vertical horizontal traverses of the collimator opening . . . . .	35
12. Dimensions of modified detector cavity showing crystal eclipse locations. . . . .	36
13. Cross sectional view of the source silo. . . . .	38
14. Dimensions of collimator wedges. . . . .	41
15. Vertical section of source silo showing roof shield stacking pattern . . . . .	44
16. Diagram of source irradiators. . . . .	48
17. Cs-137 Response function . . . . .	55
18. Secondary photon energy as a function of scattering angle. . . . .	58
19. Typical spectrometer response surface. . . . .	61

20.	Hyodo response function. . . . .	68
21.	Unfolded 70-cm response functions. . . . .	72
22.	Geometry for intrinsic efficiency calculation. . . . .	76
23.	Intrinsic efficiency for 4 x 5" NaI crystal for various source/detector distances. . . . .	78
24.	Unfolded 400-cm response functions . . . . .	79
25.	Comparison of unfolded Cs-137 spectrum using either the KSU or RRA Unfolding parameters. . . . .	83
26.	Comparison of unfolded NaI spectra for the unshielded source configuration . . . . .	85
27.	Comparison of energy spectra with and without in-silo scattering. . . . .	87
28.	Effect of in-silo scattering on skyshine exposure rate . . . . .	88
29.	Comparison of representative calculated and unfolded measured spectra for the unshielded source configuration . . . . .	92
30.	Comparison of unfolded NaI spectra for the 8" shielded source configuration . . . . .	94
31.	Comparison of unfolded NaI spectra for the 16" shielded source configuration. . . . .	95
32.	Unfolded NaI spectrum showing direct penetration plateau. . . . .	97
33.	Direct penetration exposure rate contribution. . . . .	98
34.	Comparison of representative calculated and unfolded measured spectra for the 8" shielded source configuration . . . . .	99
35.	Comparison of representative calculated and unfolded measured spectra for the 16" shielded source configuration. . . . .	101
36.	Energy sensitivity of the Reuter-Stokes high pressure ionization chamber . . . . .	107

37. Effect of non-ideal energy sensitivity on the distribution of exposure rate contribution for the unshielded source configuration. . . . .	111
38. Effect of non-ideal energy sensitivity on the distribution of exposure rate contribution for the 8" shielded source configuration. . . . .	112
39. Effect of non-ideal energy sensitivity on the distribution of exposure rate contribution for the 16" shielded source configuration. . . . .	113
40. Comparison of measured and calculated exposure rates for the collimated detector geometry . . . . .	128
41. Comparison of measured and calculated $4\pi$ geometry exposure rates . . . . .	132
42. Comparison of $4\pi$ geometry exposure rates for the unshielded source configuration. . . . .	135

## List of Plates

	Page
1. Detector shadow shield assembly . . . . .	21
2. Unshielded detector cavity/collimator assembly . . . . .	22
3. Shielded detector cavity/collimator assembly . . . . .	24
4. Lower portion of styrofoam detector cradle . . . . .	25
5. Rear of detector trailer showing collimator opening and trailer leveling system. . . . .	27
6. Complete truck/trailer mobile detection unit . . . . .	29
7. Installed inner collimator . . . . .	31
8. Completed source silo. . . . .	39
9. Source irradiator prior to placement in source silo. . . . .	46
10. Source irradiators being installed on movable platform . . . . .	47

## List of Tables

	page
1. Mean Thickness of Silo Roof Shields. . . . .	43
2. Measured Concrete Densities for Various Source Silo Structures . . . . .	45
3. Optimized 70-cm Unfolding Parameters . . . . .	74
4. Optimized 400-cm Unfolding Parameters. . . . .	80
5. Unfolding Parameters Used by Radiation Research Associates . . . . .	80
6. Data Used in the Construction of F(E). . . . .	118
7. Results of Preliminary $\bar{F}$ Calculations. . . . .	120
8. Published Values of the Energy Dependence Correction Factor for the Unshielded Source Configuration . . . . .	122
9. Comparison of Unshielded $\bar{F}$ Values. . . . .	124
10. Comparison of $\bar{F}$ Values for the 8" Shielded Source Configuration. . . . .	125
11. Comparison of $\bar{F}$ Values for the 16" Shielded Source Configuration. . . . .	125
12. Calculated Geometry Correction Factors . . . . .	131
13. $4\pi$ Geometry Exposure Rates for the Unshielded Source Configuration. . . . .	137
14. $4\pi$ Geometry Exposure rates for the 8" Shielded Source Configuration. . . . .	140
15. $4\pi$ Geometry Exposure Rates for the 16" Shielded Source Configuration. . . . .	142



## 1.0 Introduction

The ability to predict accurately the exposure rate at large distances from a gamma radiation source of known intensity is becoming increasingly important as the control of radiation levels in and around nuclear facilities becomes more stringent. Of particular concern are those sources of radiation which result in a relatively low exposure to a large population over an extended length of time. One such source of low level exposure is the reflection of gamma photons by the air above a radiation source. This air-scattered radiation is referred to as skyshine and may be an important consideration in the design of facilities from which gamma photons may escape into the atmosphere. For example, a reactor containment vessel or radioactive waste storage building will generally have less shielding in the roof than in the side walls and therefore, escaping radiation will have a preferential upward direction. In the design of such facilities, the accurate calculation of the skyshine radiation at large distances from the facility becomes very important.

The most accurate computational techniques available today for the calculation of gamma photon transport through the atmosphere are the multi-energy group and multi-dimensional transport theory codes. However, such transport codes are very complex and require extremely large computers. Consequently, the use of these photon transport codes for skyshine calculations is prohibitively expensive for routine analysis, often requiring several thousand dollars worth of computer time for a

single run if a high level of accuracy is required.

Because of the large financial burden associated with the routine use of these state-of-the-art transport codes, much effort has been expended in the development of simplified, approximate models to be used specifically in the calculation of skyshine exposure rates. The most popular of these simplified models are based on the point kernel technique which calculates a first collision source distribution in the atmosphere around the source. The angular distributions of the secondary photons are given by the Klein-Nishina cross-section. Buildup factors are then used to account for subsequent scattering between the location of the first interaction and the location at which the exposure rate is to be calculated.

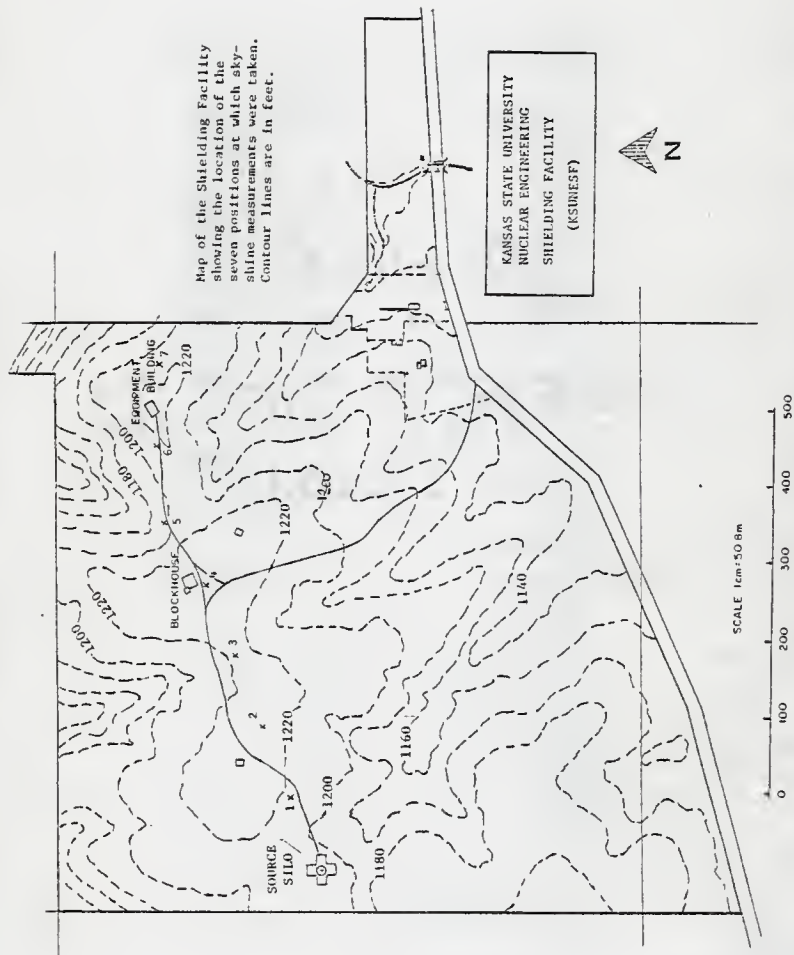
Although such simplified calculational models are quite inexpensive to use compared to the sophisticated transport codes, the accuracy of these models, particularly for large source/detector distances, is generally unknown. A working committee was recently formed by the Nuclear Safety Research Association of Japan (NSRA) because of renewed interest in the control of low level exposure to the general population<sup>1</sup>. The membership of this committee consisted of representatives from various Japanese utilities, consulting firms and research organizations. Skyshine exposure rate predictions for various point source configurations were calculated by members of this committee using several different point kernel schemes. The results obtained by this committee exhibited large discrepancies between the values calculated by the different schemes. Often a factor

of almost seventy would separate the extreme results at the same source/detector distance.

The large disagreement between many of these results obtained by the working committee indicated a large uncertainty in the ability to predict skyshine exposure rates. This uncertainty and the importance of the skyshine problem prompted the committee to design and sponsor a benchmark skyshine experiment to provide definitive data to compare with calculated predictions. Although other skyshine experiments have been previously performed, the source-detector geometries employed in these studies were generally so complex that three-dimensional skyshine models would be required for an accurate description of the experimental configurations<sup>1,2</sup>.

A benchmark skyshine experiment, designed and sponsored by the NSRA, was performed from May through November 1977, at the Kansas State University Nuclear Engineering Shielding Facility (KSUNESF) which is located approximately five miles west of the Kansas State University campus in Manhattan, Kansas. A map of the shielding facility, which is approximately 175 acres in extent, is shown in Fig. 1.

To obtain skyshine radiation fields of sufficient intensity to be measured over the 700 meter measurement baseline, three Co-60 sources with nominal strengths of 10, 250 and 5000 Ci were employed in specially fabricated skyshine irradiators. An approximately cylindrical concrete silo was built with walls sufficiently thick so that the direct penetration component of the exposed sources would be negligible. Measure-



ments of skyshine radiation fields from three different source configurations were made, first with the source radiation collimated into a  $150^\circ$  upward directed conical beam and later with the sources shielded by 8 and 16 inches of concrete.

Spectral measurements of the skyshine radiation field were taken with a NaI(Tl) scintillation spectrometer. The NaI crystal was housed in an eight ton, lead, steel and concrete collimator assembly to reduce the background count rate and define a collimation angle for the skyshine radiation. The collimator assembly along with the multi-channel analyzer and supporting electronics were contained in a weathertight metal shed and mounted on a twelve ton capacity, 8' by 29' semitrailer. The trailer and detection assembly were moved over the 700 meter measurement baseline by a five ton capacity tractor-truck. Additionally, total exposure rate measurements were made with a high pressure ionization chamber at source/detector distances ranging from 30 to 700 meters.

This work reviews and examines the experimental facilities, the experimental methods, and the original analysis of the benchmark data which was performed by Radiation Research Associates, Inc., of Fort Worth, Texas<sup>3</sup>. Due to the large magnitude of the necessary facilities, much effort (including the author's) was devoted to building the source silo and the detector collimator assembly. The author also played a major role in the integration, calibration, and implementation of the gamma spectrometer. These activities are described in Chapter 2.

An independent analysis of the skyshine spectral measurements is presented in Chapter 3. The measured spectra were unfolded with the SEGO<sup>4</sup> unfolding code and compared to the results of detailed transport theory calculations obtained with DOT-3.5<sup>5</sup> two-dimensional transport code. An estimate of the accuracy of the transport code's predictive abilities are obtained through this comparison.

The high pressure ionization chamber measurements must be corrected for the non-ideal energy sensitivity of the detector. Methods are presented for obtaining these corrections and the corrected measurements are then compared to predictions calculated from transport theory. These results and comparisons are presented in Chapter 4. Additionally, the unfolded NaI spectra are used for the first time to obtain an independent determination of the total skyshine exposure rate. These values are also compared to the high pressure ionization chamber measurements in Chapter 4.

## 2.0 Experimental Facilities and Methods

A great deal of effort was expended in the construction of the facilities necessary for this experiment. Because of the large distances over which skyshine measurement were to be taken, a wide range of source strengths were used. This necessitated a large irradiation unit to provide sufficient shielding of the sources and to accommodate the different source configurations utilized. The preparatory activities centered around three main projects:

- 1) the integration and calibration of the spectrometer,
- 2) the construction of the detector cavity and collimator, and
- 3) the construction of the source silo and its associated components.

This chapter will describe the above items and their fabrication.

### 2.1 Gamma-Ray Spectroscopy System

Due to the relatively large source detector distances over which skyshine measurements were to be made, the foreground to background signal ratio was expected to approach unity at the remote measurement locations. Because of this consideration, a NaI(Tl) gamma-detection system was chosen over a semiconductor. Although the resolution of a semiconductor based spectrometer generally exceeds that of a NaI spectrometer, the comparatively low efficiency of the former system precluded its use in measuring the anticipated low intensity radiation spectra. Supporting the five inch diameter by four inch deep cylindrical NaI crystal was an RCA model 4525 photomultiplier tube (PMT) plus an ORTEC model 276

preamplifier, amplifier (model 450) and high voltage supply (model 456)<sup>6</sup>. Additionally, a Canberra model 8180 multichannel analyzer (MCA) and a model 8531A tape control unit with a PERTEC model 7820-9 tape drive were used to collect and store the data. An ELCAR model 3000 line conditioner was used to supply a constant line voltage to the necessary components. The entire system is shown schematically in Fig. 2.

Although the Canberra MCA had a built-in amplifier and pile-up rejector circuit, these components were designed primarily for a CeLi based spectrometer system and did not perform adequately with NaI pulses because of the very different pulse shaping requirements for the two detectors. Consequently, an external amplifier with a variable pulse shaping feature was used and the internal amplifier of the MCA was bypassed. With the external amplifier a wide variety of time constants were available as well as a choice between unipolar and bipolar output pulses. All of the above parameters as well as the high voltage supplied to the PMT needed to be selected to accommodate a wide range of photon energies and count rates.

#### 2.1.1 Choice of Spectrometer System Parameters

The system operating parameters were chosen so that the NaI resolution would not be degraded while the system was experiencing a high count rate situation. With bipolar pulses under high count rate conditions both sides of a photopeak may become broadened as a result of pulse superposition, thus causing the resolution of the system to decrease. Alternatively, with unipolar pulses only the high energy side



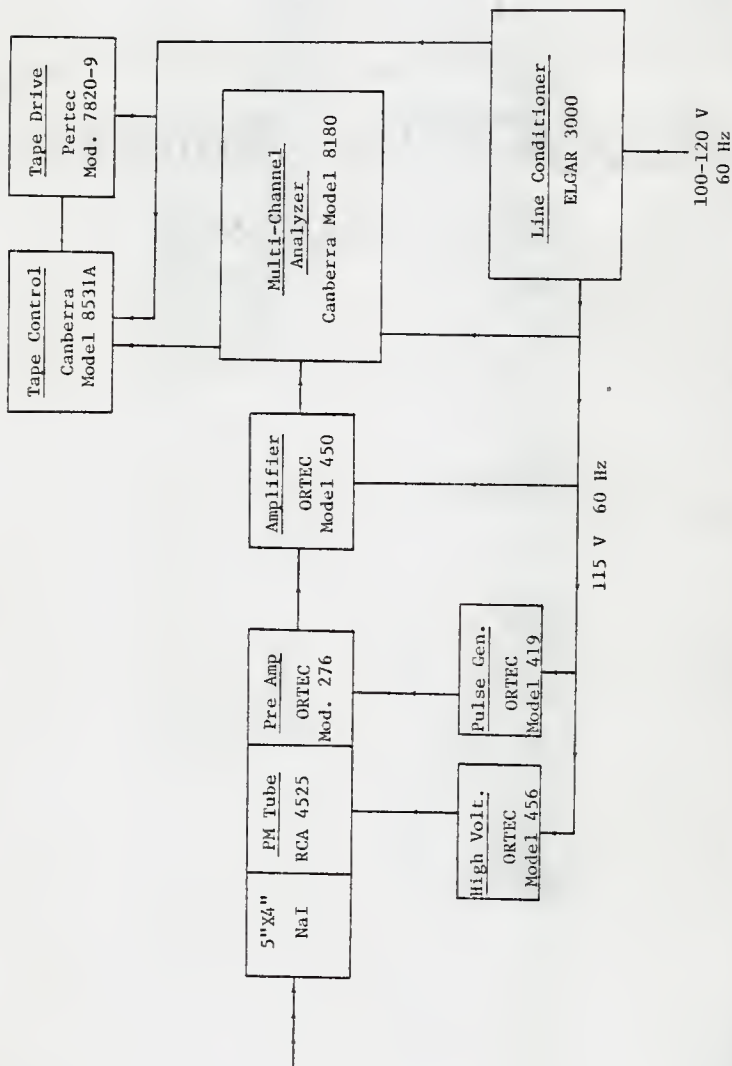


Fig. 2. Block diagram of gamma-ray spectrometer.

of the peak is broadened and is therefore more easily discernible by visual inspection. Furthermore, with unipolar pulses one has the choice of using a "base line restore" option in the amplifier. This option forces the trailing edge of the pulse to zero thus reducing the probability of a second pulse being superimposed on top of the trailing edge of the previous pulse and thereby giving too high an amplitude for the second pulse. For the high count rates expected in this experiment, the use of a pile up rejection circuit was most desirable.

The magnitude of the voltage applied to the PMT also affects the resolution of the system. In general, higher resolution is achieved with higher voltages although under high count rate conditions too high a PMT voltage will cause a voltage drop in the last dynode stages (because of the high current flow) which in turn causes a downward shift in the photopeak position towards lower energy. The 900 V PMT voltage chosen for this system was found not to degrade the spectrometer resolution significantly, while at the same time, spectral shifting was less than 1 channel for count rates up to  $3.0 \times 10^4$  counts per second (cps).

The time constant of the amplifier, which regulates the width and rise time of the amplifier output pulse, is an important parameter which can greatly affect the resolution of the spectrometer. It was determined experimentally that in general, the resolution of the system deteriorates as the value of the time constant increases. Also associated with the larger time constants is a significant increase in the dead time of the MCA. However, if too short a time constant is chosen the resolu-

tion of the system is adversely affected. It was observed that slightly more detail was discernible from spectra obtained with a 0.25  $\mu$ sec amplifier time constant than with other values, and it was this value that was chosen for normal operating conditions.

### 2.1.2 Spectrometer Calibration

For the resulting energy spectrum obtained by the MCA to be useful, the energy corresponding to any channel must be accurately known. For the present application an energy bin, or channel, width of 5 keV was specified for all spectra, which were to be 512 channels in length. Although a variety of combinations of the amplifier gain and MCA conversion gain will yield this desired result, the input pulses to the analyzer should be as small as possible to minimize dead time while using an MCA conversion gain value sufficiently large to obtain the desired spectral spread.

Since the gain of a scintillation system is affected by temperature, minor adjustments were necessary in the field. The amplifier fine gain adjustment was used to correct for these small temperature induced gain shifts. The gain shifts experienced in the field were generally less than one channel at 660 keV.

The preliminary calibration was performed using Am-241 (59.54 keV), Ba-133 (80 keV) and Cs-137 (661.6 keV) sources. These sources were used to determine the amplifier gain and the ADC baseline setting (which fixes the channel corresponding to zero energy). After the initial

calibration a mixed isotope source was used to confirm the linearity of the calibration over a large energy range. This energy range extended from 59.54 keV to 2.505 MeV. The result of this calibration test is shown in Fig. 3 where only slight deviations from the ideal linear model can be seen below 400 keV while above this point, the response is extremely linear.

### 2.1.3 System Response as a Function of Count Rate

In order to determine the maximum counting rate which could be tolerated by this system without adversely affecting its calibration or linearity, the response of the spectrometer to incident fluxes of varying intensities was studied in great detail. A nominal 3.8 mCi Cs-137 source was positioned at various distances from the detector face ranging from 122 to 1036 cm. A precision pulser, (ORTEC model 419) shown in Fig. 2, was also used to test the accuracy of the internal clock and dead time correction circuits of the analyzer. The pulser gain was adjusted so that the pulser peak fell well above the Cs-137 photopeak. The area of the pulser peak is then directly related to the true counting time.

Standard 512 channel spectra were taken at regular source-detector distances. A background spectrum was also measured during the experiment and was subtracted in a channel-by-channel fashion from each of the Cs-137 spectra after appropriate normalization to correct for different counting times. The background corrected Cs-137 photopeaks were then fitted in a least-squares manner to a Gaussian curve. This Gaussian fit

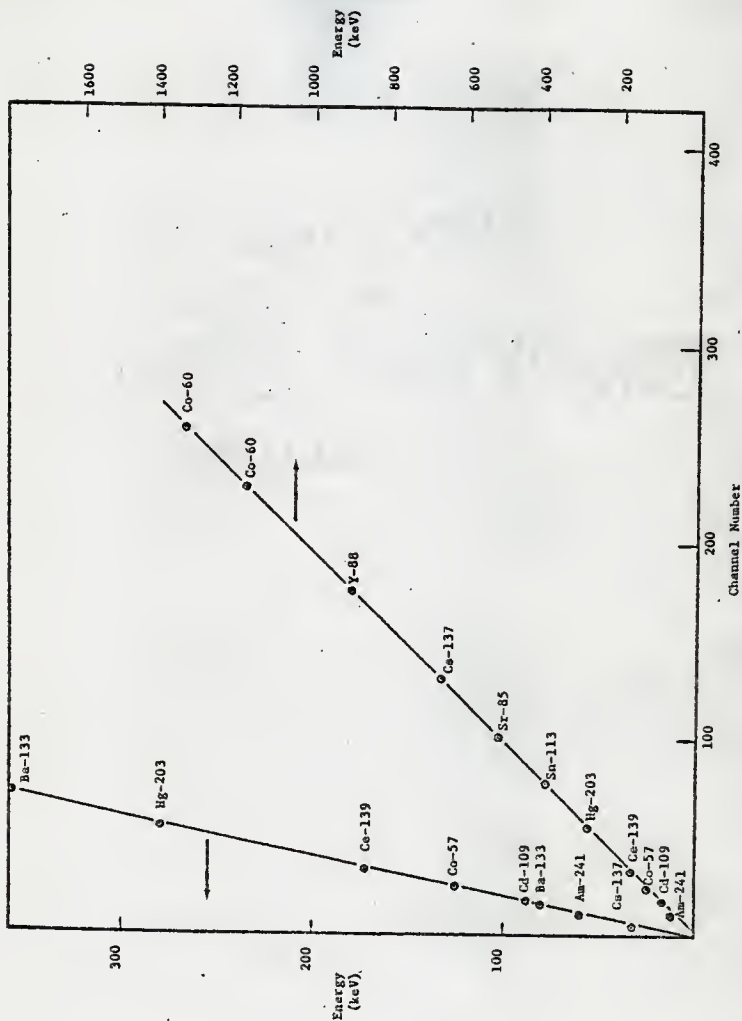


Fig. 3. Spectrometer calibration curve

yielded values for the photopeak centroid as well as the area of the fitted curve. Also evaluated for each spectra were the area of the total spectrum (neglecting the pulser peak) from which the total count rate is calculated, and the area of the pulser peak (including any pile-up tail) from which the true counting time may be found.

In Fig. 4 the centroid of the photopeak is shown as a function of the total counting rate. As can be seen, no significant gain shift occurred for total count rates below  $3.0 \times 10^4$  cps.

Another parameter of interest, the full-width-at-half-maximum (FWHM) is calculated from the least squares fitted Gaussian to the photopeak. For an ideal spectrometer, the resolution (or FWHM) should be independent of the count rate. The results for the present system are shown in Fig. 5 as a function of the total counting rate. Again, no significant degradation in the resolution is observed below count rates of  $3.0 \times 10^4$  cps.

Another method used to test for photopeak shifting under high count rate situations is to take a channel-by-channel ratio of the photopeaks, choosing one spectrum obtained with a low count rate as a reference. The results of this method of comparison are shown in Fig. 6 where a nonzero slope indicates a shift in the photopeak position. No significant shifting is observed below total count rates of  $3.0 \times 10^4$  cps.

Analysis of the pulser peak and its pile-up tail indicated that the error in the dead time correction was less than 2% in 15 out of 16 (94%) tests below  $3.0 \times 10^4$  cps. It was also verified that there was a definite

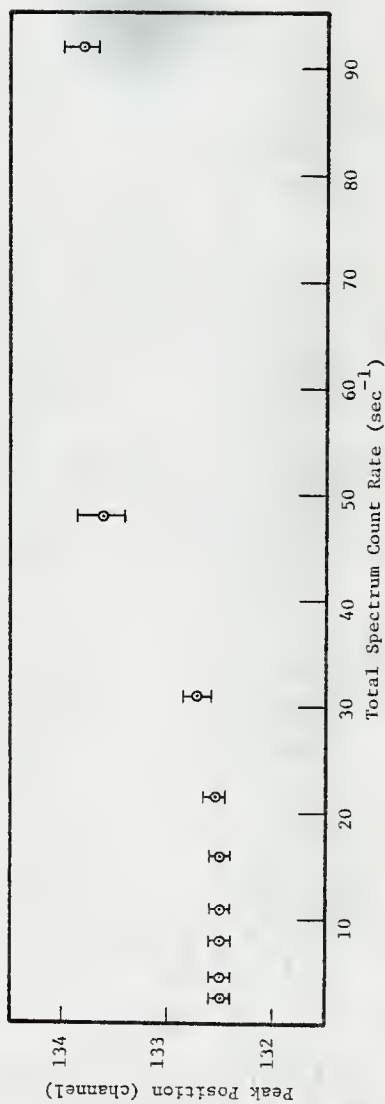


Fig. 4, Photopeak position as a function of total spectrum count rate. Abscissa annotations are in thousands.

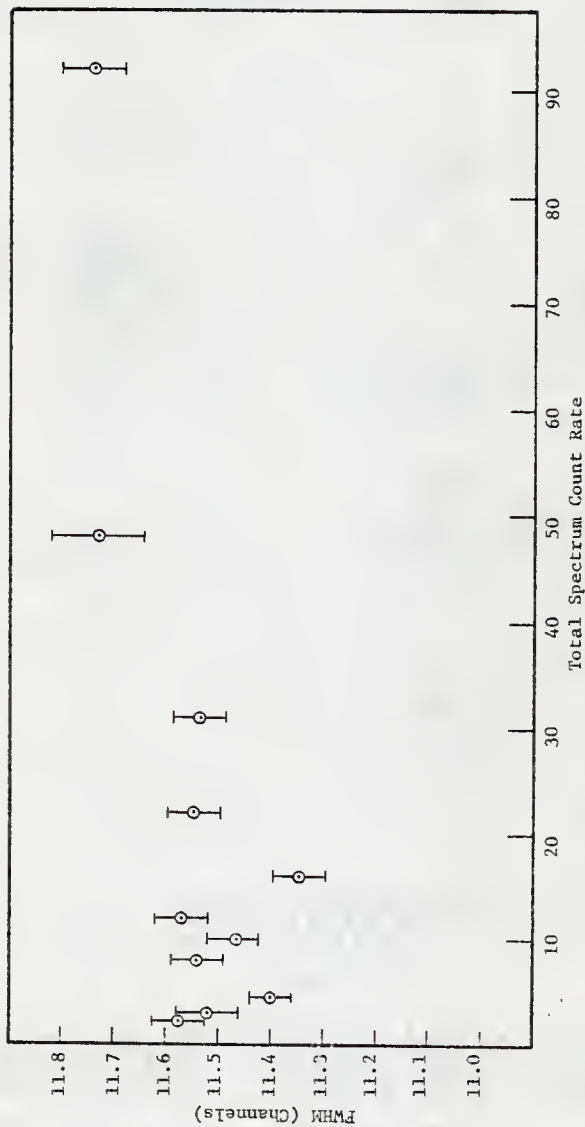


Fig. 5. System resolution as a function of total spectrum count rate. Abscissa annotations are in thousands.



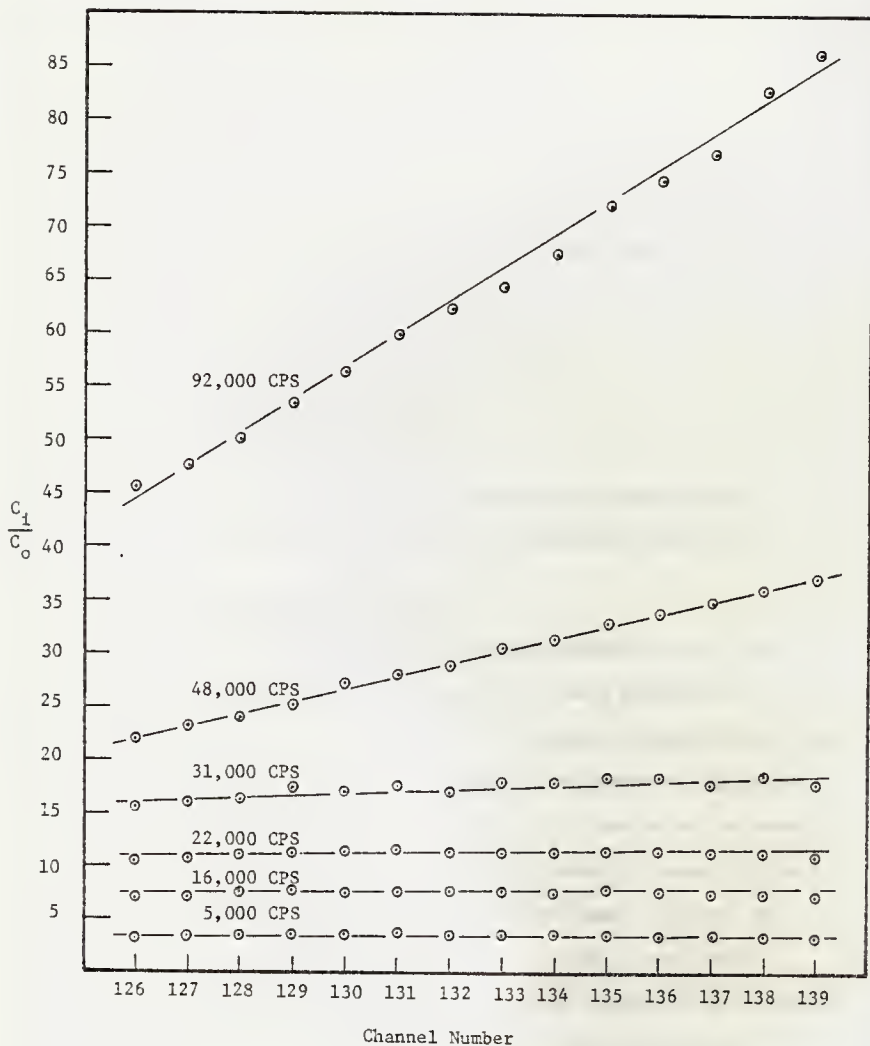


Fig. 6. Results of the "ratio test". Plotted on the ordinate is the total number of counts in a specific channel in spectrum 1 divided the total number of counts in the same channel in the reference spectrum.

linear relationship between dead time and the total count rate.

The various values of the operating parameters used in this experiment are listed below:

- 1) Unipolar amplifier pulses with 0.25  $\mu$ sec time constant
- 2) Base line restore (BLR) set to HI
- 3) Amplifier coarse gain at 100
- 4) Amplifier fine gain at 11.22 (variable)
- 5) PMT high voltage at 900 volts
- 6) MCA conversion gain at 1024/2
- 7) ADC baseline set at 4.96.

With these settings, stable system response can be expected from 30 KeV to 2.6 MeV and for total count rates less than 30,000 cps.

## 2.2 Detector Collimator Assembly

One of the major construction activities associated with this experiment was the design and fabrication of a well shielded detector cavity and collimator or shadow shield<sup>7</sup>. Although the reduction of the detector geometry from  $4\pi$  to the collimated configuration complicated the prediction and analysis of the results, this feature was necessary to increase the signal to background ratio in order to extend the baseline over which skyshine measurements could be taken. Moreover the collimated skyshine spectra were thought to provide a more severe test than  $4\pi$  spectra would have provided for the transport calculational models whose predictive abilities were the overall objective of this project.

To eliminate the need for long signal cables, the detector cavity/collimator and MCA systems were mounted on an 8' x 29' 12 ton capacity

flat bed trailer to be pulled by a 5 ton tractor truck. Since the estimated weight of the collimator assembly was well over 8 tons, equipment of this magnitude was necessary. Integration of the two systems in this manner provided the further advantage of requiring only one temperature control system to ensure the response stability of the spectrometer.

#### 2.2.1 Construction of Collimator Assembly

The collimator assembly consisted of two main chambers, the details of which are shown in Fig. 7. This assembly was constructed on the rear of a flat bed trailer with the cavity axis parallel to the trailer axis and the collimator opening oriented towards the rear of the trailer. The inner chamber or detector cavity was a 24" cube in which the NaI crystal was to be positioned. The outer chamber, to which the shadow shield was attached, was 3' square by 20" deep. The walls of both chambers were constructed of 5/16" steel plate and angle iron. The shadow shield was composed of standard sized lead bricks (2" x 4" x 8") in an angle iron frame as shown in Plate 1. An 8" square access port penetrated the rear face of the detector chamber to be used primarily as a cable conduit but was large enough to permit removal of the entire NaI crystal/PMT/preamplifier assembly if necessary. The detector cavity/collimator assembly is shown in Plate 2.

In an effort to eliminate any radiation entering the detector cavity except through the shadow shield aperture, nominal 8" lead slabs were placed on the top and bottom of the inner chamber while standard lead bricks were stacked around the sides and rear as shown

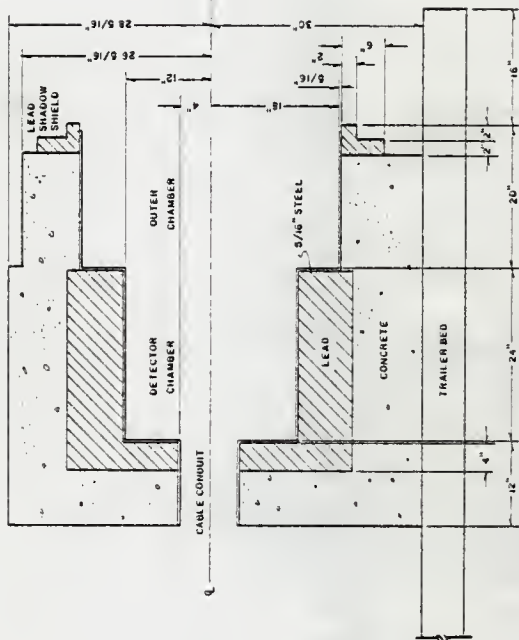


Fig. 7. Dimensions of original detector cavity.



Plate 1. Detector shadow shield assembly.



Plate 2. Unshielded detector cavity/collimator assembly.

in Plate 3. In addition to the lead shielding, concrete blocks were stacked around the sides and top of the cavity to a minimum thickness of eight inches. In order to hold the shielding materials in place during the course of the measurements, plywood panels were used to encase the sides of the assembly which were in turn held in place by circumferential cables.

The detector cavity/collimator assembly not only served to reduce the background radiation levels by a factor of five, but also proved useful in providing a large thermal inertia for the crystal/PMT/preamp assembly. Thus in the case of a failure of the environmental control system, the crystal assembly would be well insulated.

#### 2.2.2 NaI Crystal Positioning

Styrofoam was chosen to support the detector assembly inside the detector chamber because of its good thermal insulating properties, low density, and ability to isolate the crystal from minor vibrations. The crystal assembly was placed in a cradle made out of 3" thick styrofoam slabs, the bottom half of which is shown in Plate 4. Small styrofoam wedges were used to firmly fix the detector's position with respect to the shadow shield aperture. Finally, to protect the front face of the detector, a two-inch thick styrofoam cover which had been hollowed out to a thickness of less than one inch in the central portion was placed in the aperture of detector chamber. Thus, the detector system was completely insulated without significant attenuation of an incident radiation field.



Plate 3. Shielded detector cavity/collimator assembly.



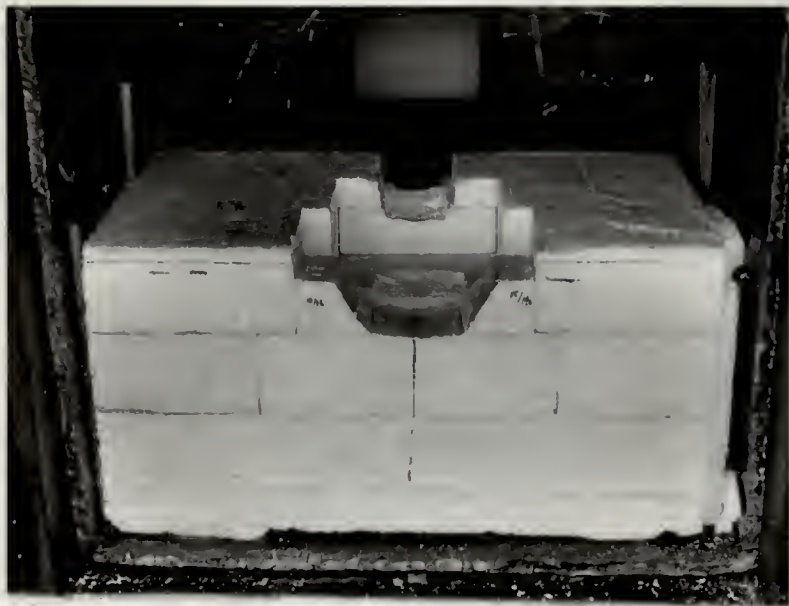


Plate 4. Lower portion of styrofoam detector cradle.

### 2.2.3 Environmental Control

Since the response of the spectrometer was affected by temperature, environmental control of the crystal assembly as well as the analyzer system was imperative. To accomplish this, two metal utility sheds were joined together and attached to the trailer in such a way as to cover the entire detector cavity/collimator assembly. There was also sufficient room behind the detector chamber for the supporting data acquisition instrumentation and its operating personnel. Large wooden doors were installed in the rear end of the shed so that when opened, the aperture of the shadow shield would be unobstructed.

Cooling for the instrumentation and detector assembly was provided by two thermostatically controlled air conditioning units with a total capacity of 10,000 Btu/hr. These were installed in the walls of the environmental shed as shown in Plate 5. To reduce the amount of heat flow into the shed, styrofoam panels were attached to the walls and roofs, all joints were caulked and weatherstripping was used around the entrance door. Finally a 2" thick styrofoam panel was placed in the shadow shield opening and plastic sheeting was stretched across the collimator door opening thereby completely sealing the rear portion of the shed. These features can be seen in Plate 5. With these measures, a constant temperature could be maintained on all but the hottest days. The shed besides providing temperature control also provided a dry and dust-free environment for the spectroscopy system.



Plate 5. Rear of detector trailer showing collimator opening and trailer leveling system.

The complete tractor-trailer detection assembly is shown in Plate 6.

#### 2.2.4 Detector Cavity/Collimator Performance

To test the performance of the collimator assembly, several energy spectra, or response functions, were taken using four National Bureau of Standards (NBS) calibration sources (Am-241, Hg-203, Cs-137, and Co-60). Figure 8 shows a Co-60 response function with the source located on the detector axis 69.85 cm from the crystal face. Although the high energy portion ( $>.8$  MeV) of the spectrum appears normal, one immediately notices several large scattering peaks below 400 KeV. These features are attributable to photons which have been multiply scattered from the steel walls of the detector cavity. Such low energy structures were highly undesirable since the skyshine spectra were expected to be composed of predominantly low energy photons.

To minimize the scattering within the detector collimator/shield assembly, two modifications to this assembly were made. First the walls of the detector chamber and the front portion of the outer chamber were lined with 1/2" lead sheeting in order to reduce the gamma-ray reflection from the walls. Secondly an inner lead collimator with a 12" square opening was placed in front of the aperture of the detector cavity in order to reduce the number of photons admitted to the detector cavity. This apparatus is shown in Plate 7. Also during these alterations, the crystal assembly was moved forward in the detector chamber to increase the collimation angle. The final detector



Plate 6. Complete truck/trailer mobile detection unit.

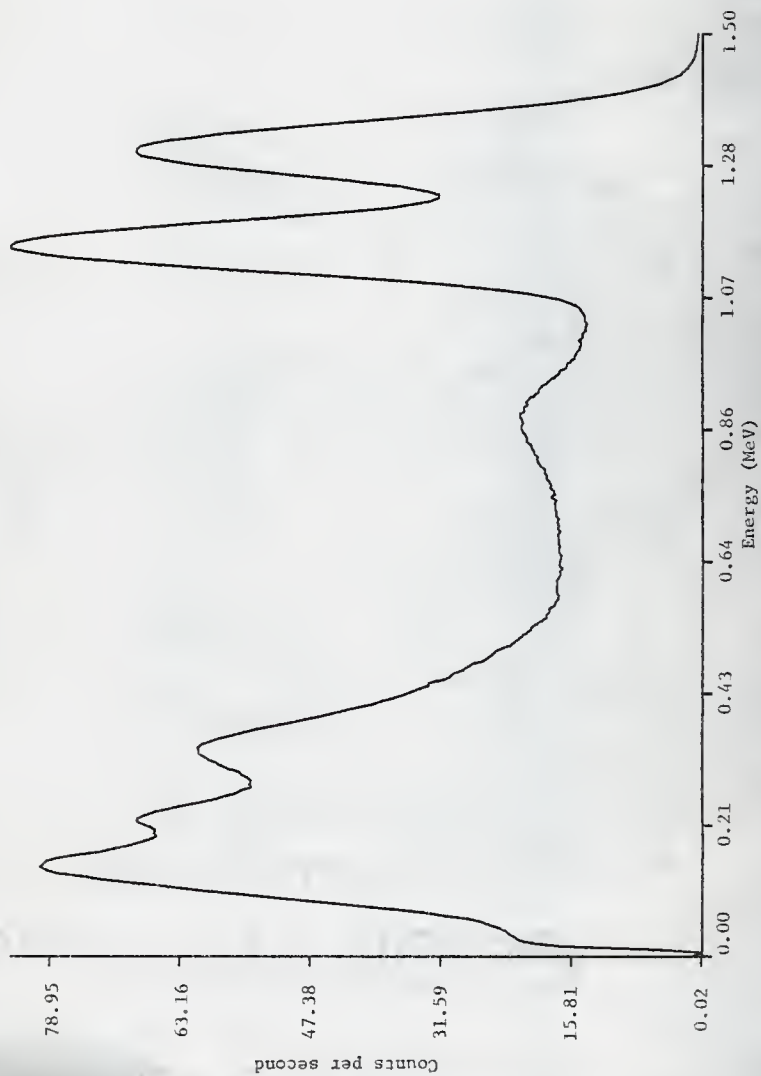


Fig. 8. Co-60 spectrum taken with original collimator assembly.



Plate 7. Installed inner collimator.

cavity/collimator is shown in Fig. 9. Figure 10 shows a Co-60 response function taken with the new collimator/shield assembly superimposed on Fig. 8 where the affect of the new collimator design and crystal position is apparent. The previous collimator scatter peaks are no longer present and the Compton plateau more nearly resembles the ideal NaI response.

To determine the effectiveness of the collimator in defining the detector geometry, a Cs-137 calibration source was moved vertically and horizontally away from the cavity axis parallel to the plane of the collimator. At various radial distances from the detector axis, response functions were measured. Ideally, as the source moves across the collimator opening neither the total count rate nor the spectral shape should change. However, as the source moves into positions where part or all of the crystal is blocked by the shadow shield (see Fig. 12), the total count rate should decrease dramatically and eventually approach that of background.

Some small deviations from the ideal behavior were noted and can be seen from the collimator traverse results shown in Fig. 11. Since the crystal size was relatively large compared to the source-detector distance, various portions of the crystal are shielded by the shadow shield at different positions as shown in Fig. 12. Consequently, the total count rate does not drop off as sharply as would be experienced with a point detector. A second non-ideal response contribution is that as the sources moves away from the detector axis a greater cross sectional area of the crystal is exposed causing the total count rate



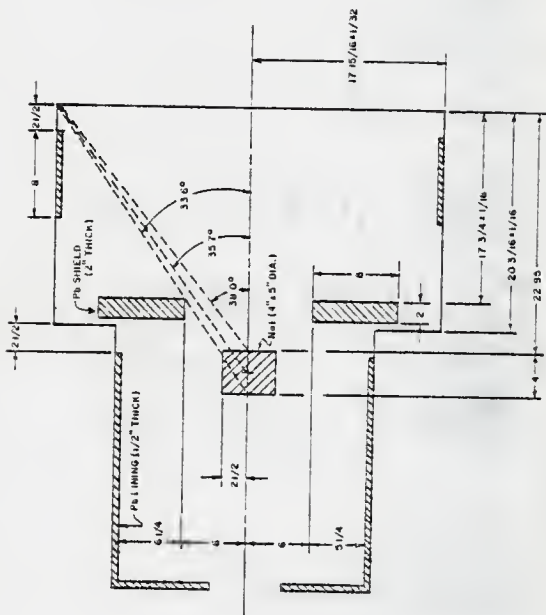


Fig. 9. Dimensions of modified detector cavity

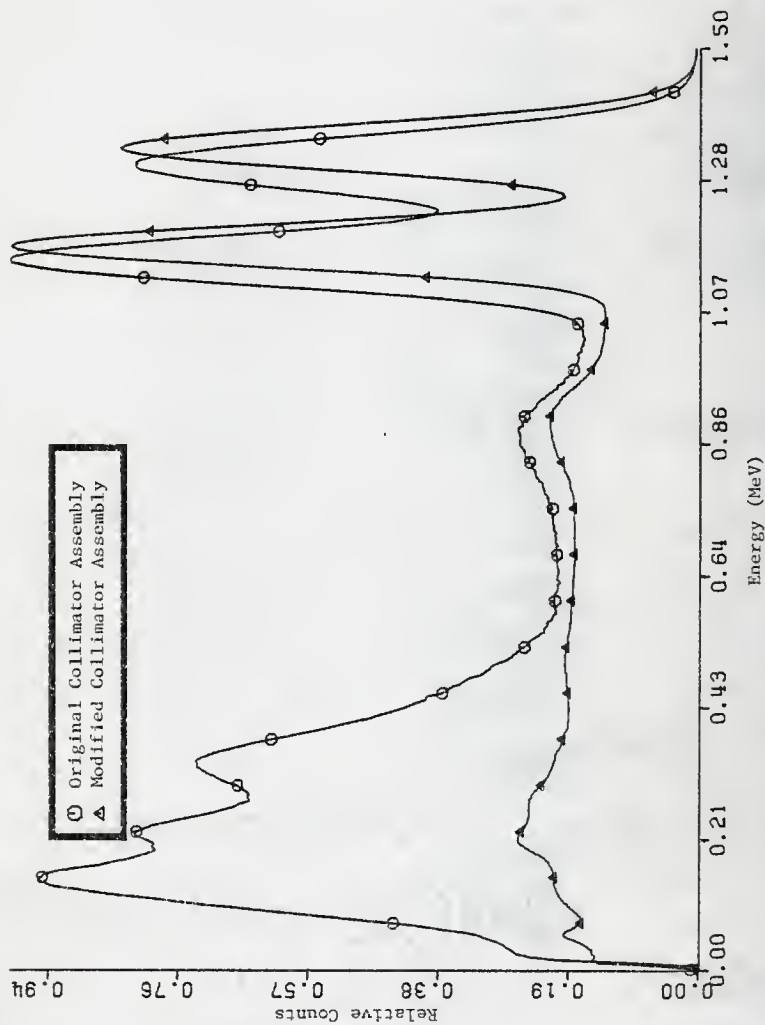


Fig. 10. Comparison of Co-60 spectra taken with original and modified collimator assembly.

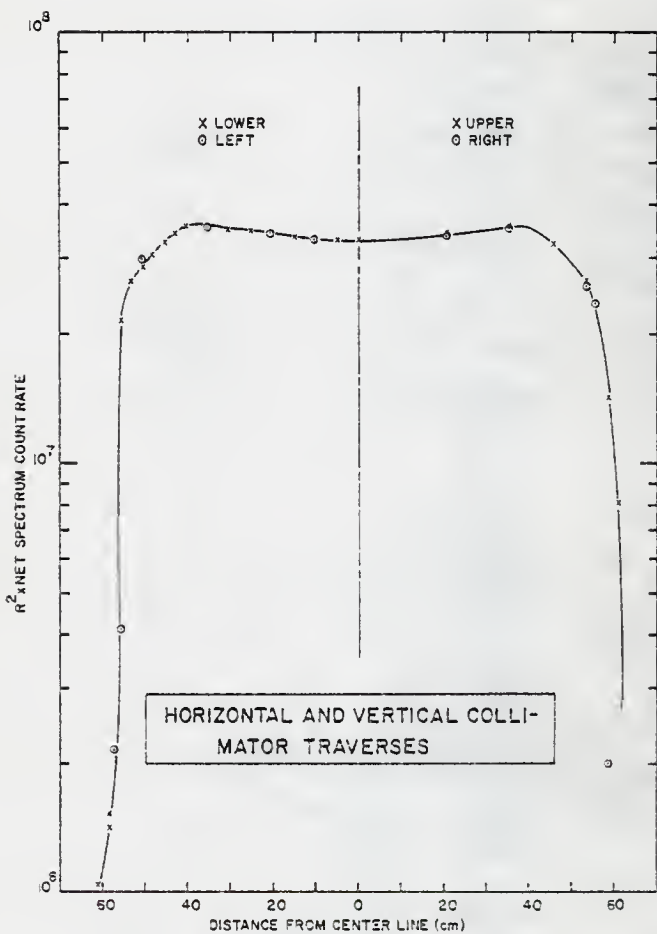


Fig. 11. Results of vertical and horizontal traverses of the collimator opening.

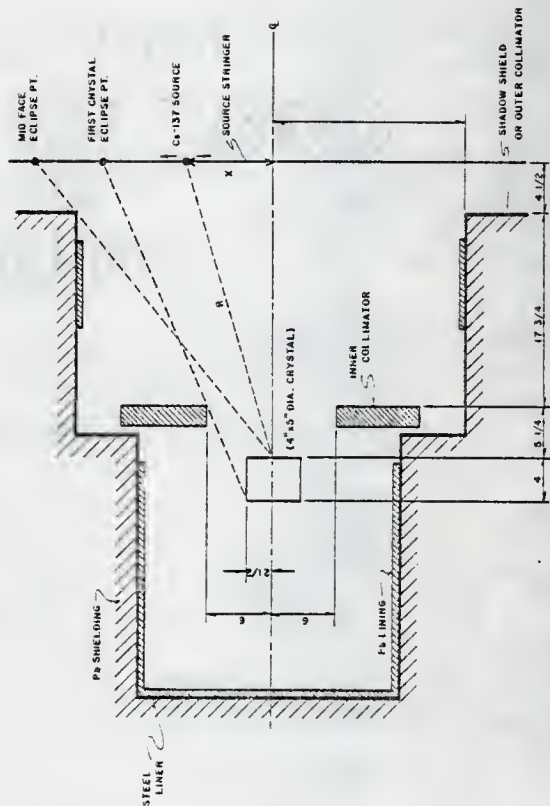


Fig. 12. Dimensions of modified detector cavity showing crystal eclipse locations.

to rise slightly. A correction factor for this phenomenon will be discussed in Chapter 4.

### 2.3 Source Silo and Associated Components

The second major construction endeavor undertaken for this project was the fabrication of the source silo and its supporting components<sup>8</sup>. The silo was designed to house the two Co-60 source irradiators used in the project and to provide sufficient shielding so that the component of radiation penetrating the walls would be negligible compared to the skyshine component. In addition to the silo, collimator wedges were fabricated and used to define the source collimation angle in the unshielded skyshine portion of the experiment. Concrete roof slabs were fabricated and employed in the two shielded measurement configurations.

#### 2.3.1 Source Silo

To facilitate the numerical modeling of the source configuration, a silo with approximately an annular cross section was desired. Practical considerations dictated the use of concrete forms with flat sides resulting in a silo in the shape of dodecagon as shown in Fig. 13. To support the mass of the silo and the source casks, a 9" thick base pad was poured containing large amounts of reinforcing steel and wire mesh. On the four sides of the base pad, 4" thick slabs were poured to provide easy access to the silo. The completed silo is shown in Plate 8.

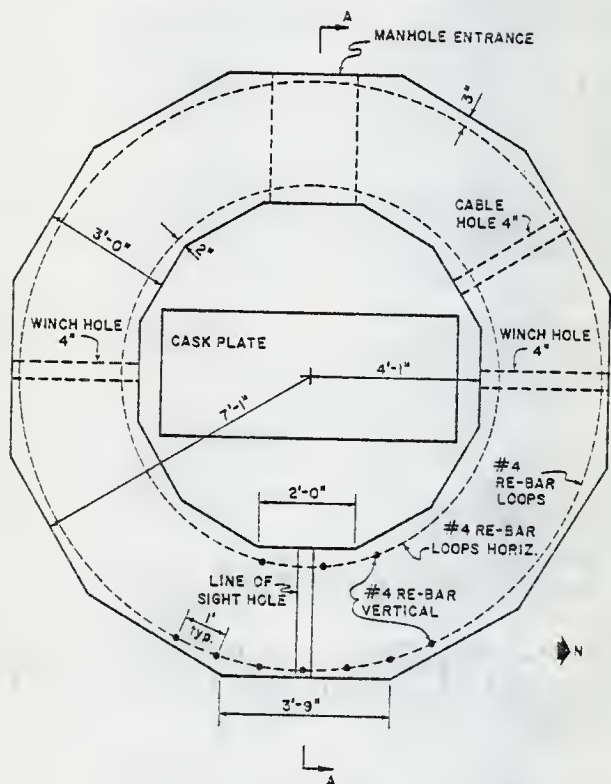


Fig. 13. Cross sectional view of the source silo



Plate 8. Completed source silo. A-frame crane is used for positioning of roof shields.

The top and bottom halves of the silo wall were poured in two distinct stages using step joints between both halves as well as at the wall base. The concrete was also thoroughly vibrated to reduce the possibility of voids within the wall. Several small penetrations at the bottom of the silo wall were made to provide access ports for electrical cables and positioning of the source irradiators.

A "line of sight" penetration was made in the top front side of the wall so that the Co-60 sources could be viewed directly from some of the closer measurement positions. Normally this opening was completely filled with standard sized concrete blocks which were removed only for the source calibration measurements.

### 2.3.2 Collimator Wedges

For the unshielded skyshine measurements it was required that the radiation field be collimated into an upward  $150^\circ$  conical beam. This was accomplished by positioning wedge shaped concrete blocks around the top of the source silo wall thus forming the perimeter of a cone with a  $150^\circ$  angle whose projected apex coincided with the position of the raised Co-60 sources. In this way the collimated beam strength could be changed by simply moving the desired source cask to the center position of the silo so that the raised source would be at the apex of the cone. With this technique, no adjustment of the collimator wedges would be required.

The dimensions of the collimator wedges, shown in Fig. 14, were chosen so that 48 of them would form an annulus with an 3'2" inside



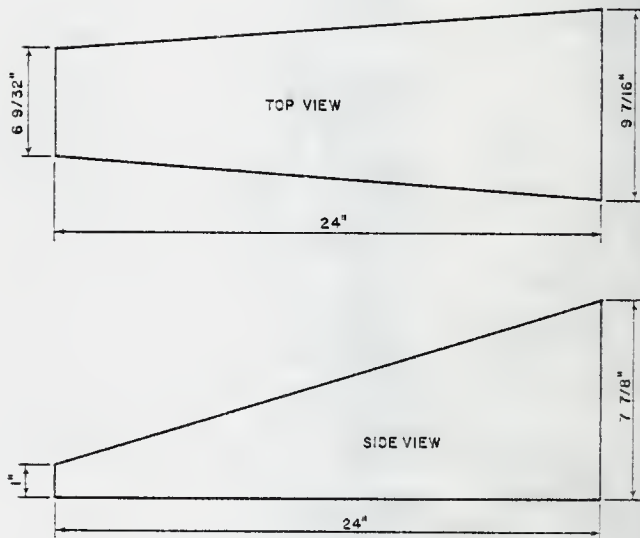


Fig. 14. Dimensions of collimator wedges.

diameter. Arranged in this manner, a collimation cone with a  $150^\circ$  angle would be obtained. To minimize radiation streaming between the wedges and direct penetration, concrete and lead bricks were placed around the outside of the wedges in such a way as to not affect the collimated radiation field. The final collimation angle was measured and found to be within  $0.2^\circ$  of the design value.

### 2.3.3 Silo Roof Shields

The shielded portion of the experiment called for the radiation sources to be covered by 20 and 40 cm thick shields of concrete. Consequently  $4' \times 12' \times 4''$  concrete slab shields were constructed by pouring concrete into steel frames with stepped sides thus allowing adjacent slabs to overlap. To provide the needed mechanical strength so that the slabs could withstand being moved repeatedly, minimal amounts of structural steel and wire mesh were imbedded in the concrete.

To form the roof shield three slabs were laid side by side so that the stepped sides overlapped, thus eliminating the possibility of radiation streaming between the slabs. A thin layer of concrete was placed on the top surface of the silo wall immediately prior to the positioning of the first layer of roof slabs. This ensured a complete seal between the roof and silo wall thereby eliminating any possibility of streaming under the lowest layer of slabs. To minimize the effect of the steel frames on the penetration of radiation through the roof, the slabs were positioned such that the long axis of the slabs were directed toward the measurement locations. With this configuration the

frames would significantly affect only that portion of the field leaving the silo perpendicular to the source/detector axis.

The thickness of each slab was measured at six locations with a pair of specially constructed long armed capilers. The results are shown in Table 1<sup>8</sup>. In order to provide a consistent geometry, the slabs were always positioned in the same stacking pattern as shown in Fig. 15.

Table 1. Mean Thicknesses of Silo Roof Shields<sup>8</sup>

Slab No.	Thickness (cm)
1	10.77 ± 0.29
2	10.90 ± 0.48
3	10.72 ± 0.19
4	10.40 ± 0.16
5	10.34 ± 0.21
6	11.03 ± 0.34
7	10.45 ± 0.25
8	10.53 ± 0.19
9	10.45 ± 0.16
10	10.40 ± 0.22
11	10.58 ± 0.16
12	10.58 ± 0.24
Center, 9 + 12	21.03 ± 0.29
Center, 1 + 6 + 9 + 12	42.83 ± 0.53

Standard concrete test specimens were taken for all of the concrete pours of the silo wall, collimator wedges, and roof slabs. The densities of these specimens were determined by faculty members of the

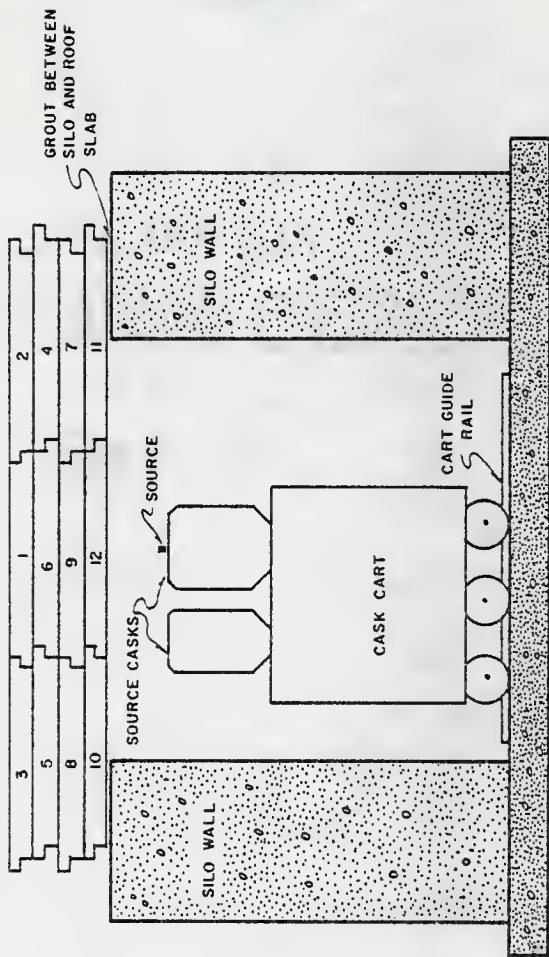


Fig. 15. Vertical section of source silo showing roof shield stacking pattern.

Civil Engineering Department at Kansas State University. These results are tabulated in Table 2<sup>8</sup>, where no correction has been made for the affect of the structural steel within the actual components.

Table 2. Measured Concrete Densities for Various Source Silo Structures<sup>8</sup>

Structure	Density (g/cm <sup>3</sup> )
Silo	2.17 ± 0.02
Roof Shields	2.13 ± 0.02
Collimator Wedges	1.93 ± 0.02

#### 2.3.4 Source Irradiators

The source irradiators were designed and manufactured by J. L. Shephard and Associates, Inc. These irradiators were mounted on a moveable platform in such a way that either cask could be positioned at the center of the silo. Plates 9 and 10 shows the two irradiator units during their installation while Fig. 16 gives the dimensions of the irradiator assembly. The larger cask contains an effective 3800 Ci Co-60 source while the smaller cask contains both the effective 10.3 and 229 Ci Co-60 sources\*. The two largest sources when in the exposed position had their midpoint the apex of the collimation cone while the 10.3 Ci source was 2" from the apex.

\* The source strengths as reported by the manufacturer were 12.2, 255, and 5220 Ci. To ascertain the effective source strengths, a "good geometry" experiment was performed at a distance of 300 m. These results were then used to cross calibrate the skyshine sources using a NBS source of known intensity as a reference. The observed reduction in intensity is presumably due to shelf-shielding effects.



Plate 9. Source irradiator prior to placement in source silo.



Plate 10. Source irradiators being installed on movable platform.

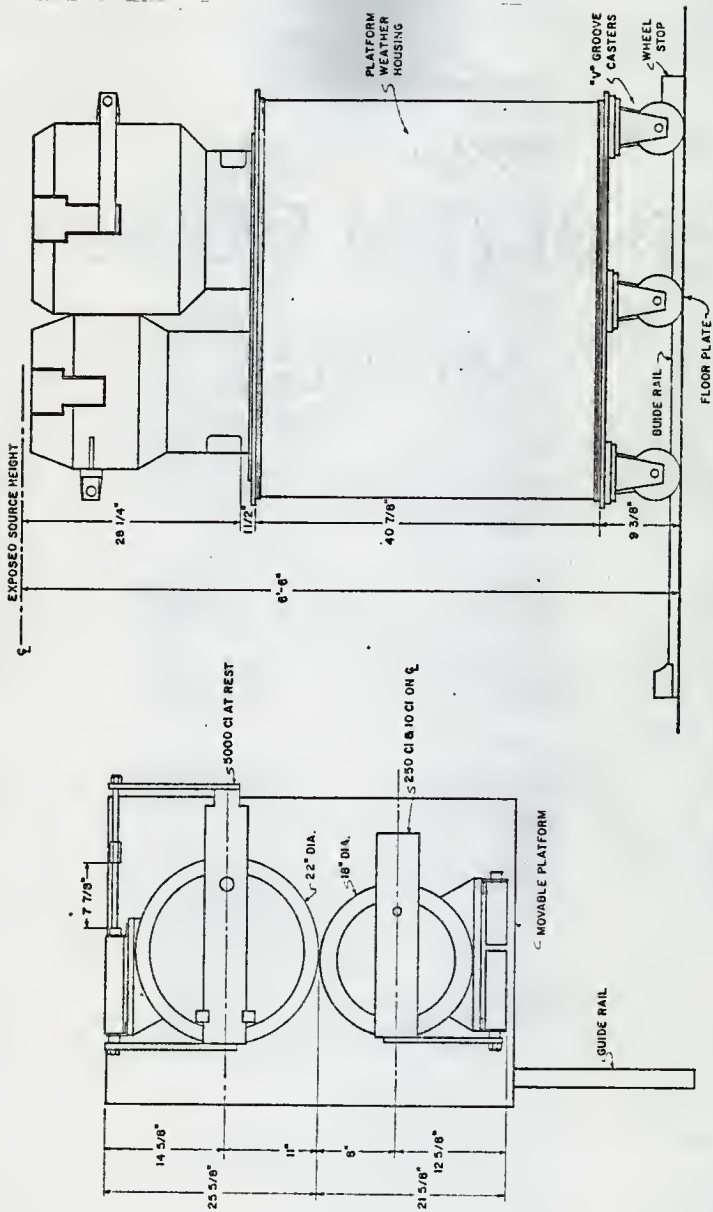


Fig. 16. Diagram of source irradiators



The irradiators can be operated from a remote console up to 100 m from the sources. During operation, the central rectangular drawer, or attenuator, at the top of each cask is withdrawn pneumatically until a vertical hole in the slide is properly positioned over the appropriate vertical source hole in each cask. Of the two source holes in the smaller cask, the one for the  $^{229}\text{Ci}$  source is on the center line of the unit while the  $^{10}\text{Ci}$  source position is 2" from that point. After the attenuator is accurately positioned, the specified source is raised pneumatically out of the irradiator to the "exposed" position. All movements of the irradiator systems are monitored by microswitches and status lights on the operator's console indicate the position of the sources.

To protect the entire irradiator assembly, a sheet metal weather housing was placed over both units and secured. Incorporated into the metal cover were two thin walled hemispherical steel domes positioned over the two source locations. Therefore regardless of the upward direction taken by the gamma photons, all radiation would experience identical amounts of mass attenuation while penetrating the weather cover.

## 2.4 Measurement Procedures

### 2.4.1 Trailer Positioning

For each skyshine spectral measurement, it was required that the detector cavity axis be horizontal and directed toward the silo. In order to adjust the attitude of the trailer, an I-beam frame was welded beneath the rear of the trailer so that hydraulic jacks could be placed

under each rear corner. In this way the entire back of the trailer could be raised and/or tilted. Also, by simply adjusting the length of the front support legs, the front end could be raised or lowered.

During the construction of the collimator assembly, the trailer was positioned using the above adjustment procedures so that the lower edge of the shadow shield was horizontal and the sides vertical. Two sets of brackets were then securely fastened to the rear and one side of the trailer so that when a level rested on them a level condition was indicated. Thus for routine positioning, adjusting the attitude of the trailer until the two perpendicular lines, defined by the two sets of brackets, defined a horizontal plane ensured that the collimator was vertical and the detector assembly axis horizontal.

In order to align the detector assembly with the source position, a transit was used to place two aiming pins on opposite ends of the peak of the environmental shed roof so that they defined a vertical plane with the cavity axis. Therefore, by positioning the trailer so that the two aiming pins and the center of the source silo were colinear ensured that the detector cavity axis was also aligned with the source silo. Since by necessity this alignment was done before the trailer was leveled, some error in alignment might have occurred although it was estimated to be less than  $2^\circ$ . It was demonstrated by experiment that the measured skyshine spectrum was totally insensitive to such small errors in the trailer orientation.

#### 2.4.2 Spectral Quality Control

To ensure that the detection system was properly calibrated, several test spectra were taken prior to any skyshine measurements. After the instrumentation had been turned on for approximately 30 minutes, a mixed isotope source was used to adjust the system to the proper calibration. Next a Cs-137 response function was taken which was analyzed with respect to the total count rate as a check on the system efficiency. This spectrum was also inspected visually to verify the spectral shape. Once it was confirmed that the system was operating properly, a background spectrum was taken after which skyshine measurements were made. After each skyshine spectrum, a mixed isotope response function and a background spectrum were taken in order to monitor the system calibration and background levels with time.

The count times for each skyshine spectral measurement were chosen so that acceptable statistical uncertainties in the measured spectra would be obtained. Additionally, duplicate measurements were made to determine the reproducibility of the results and, when possible, different sources were used as further test of reproducibility.

### 3.0 Spectral Analysis and Comparisons

A major aspect of the Benchmark Skyshine Experiment was the measurement of skyshine energy spectra with a collimated NaI(Tl) spectrometer. One of the reasons for the measurement of the skyshine spectra was to serve as a benchmark against which the results of photon transport models could be compared. However, because of the statistical nature of the energy deposition mechanisms in the crystal and the subsequent pulse shaping and amplification processes, the observed pulse-height spectrum often bears little semblance to the true incident spectrum. It is thus necessary to correct or "unfold" the measured spectra to obtain the actual energy distribution of the incident radiation. The unfolding technique used in this study to obtain the energy dependence of the original spectrum from the observed spectrum will be described in the first section of this chapter. The second section of this chapter compares the unfolded measured spectra with the energy spectra calculated with the DOT-3.5<sup>5</sup> photon transport code.

#### 3.1 Data Analysis Techniques

A common problem in an experimental measurement is the distortion of the quantity of interest by the detection device. In the case of measuring the energy distribution of a radiation field with a NaI detector, the differences between the incident and measured spectrum arise in the crystal as well as in the electronics of the system. The crystal induced distortions arise mainly from the statistical nature of the gamma-ray interactions within the crystal resulting in either total or

partial deposition of the incident photon energy. The primary component of the electronic distortion is the statistical fluctuation of the photoelectron multiplication in the photomultiplier tube (PMT). To obtain an estimate of the true energy dependence of the primary radiation field, these distortions must be corrected by "unfolding" the measured spectrum.

### 3.1.1 Spectral Characteristics

The height of the voltage pulse entering the multichannel analyzer (MCA) is directly proportional to the amount of energy deposited in the crystal by the incident photon. Although several types of interactions are possible between the photon and the crystal, three types play the dominant role in radiation spectroscopy: photoelectric absorption, Compton scattering, and pair production which predominate below .3 MeV, between .3 and 1.1 MeV, and above 1.1 MeV respectively<sup>9</sup>. All of these processes result in either the partial or complete transfer of the photon energy to a secondary electron.

An understanding of the energy deposition and signal collection, shaping and amplification processes in a NaI spectrometer form a basis for interpreting the observed pulse height distribution. Of special concern are the following processes which introduce non-ideal responses in the spectrometer system<sup>9</sup>:

- 1) partial energy deposition of the incident photon energy in the crystal,
- 2) nonlinear light production within the crystal,
- 3) non-uniformity of photoelectron collection from the photocathode, and

- 4) statistical fluctuations in the electron multiplication during the cascade through the dynodes.

A typical Cs-137 response function is shown in Fig. 17, where some of the more obvious features have been identified. The full energy peak, or photopeak, arises when the entire energy of the incident photon is deposited in the crystal within a time interval too short to be resolved by the detector. The deposition may occur in one photoelectric absorption or a series of Compton scatters followed by a photoelectric absorption.

One should notice that even though the photopeak represents the detection of a photon with a discrete energy, a Gaussian shaped response is obtained. This is the result of many factors, the dominant one being the statistical nature of the electron multiplication cascade process in the PMT. The multiplication factor for a given dynode, defined as the number of secondary electrons emitted per incident electron, is not constant but fluctuates about some mean value. This in turn causes the amplitude of the PMT output voltage pulse (produced by the deposition of energy  $E$  in the crystal) to fluctuate about some mean value. As a consequence of this, the photopeak is distributed about some mean channel corresponding to energy  $E$ . This electronic smearing is obviously not limited to the photopeak but is manifested over the entire spectrum.

Another contributing factor to the spectral broadening is non-linear crystal response with energy. If the light production within the crystal varies with the energy of the electron, the total light yield will be different from event to event, depending on how the

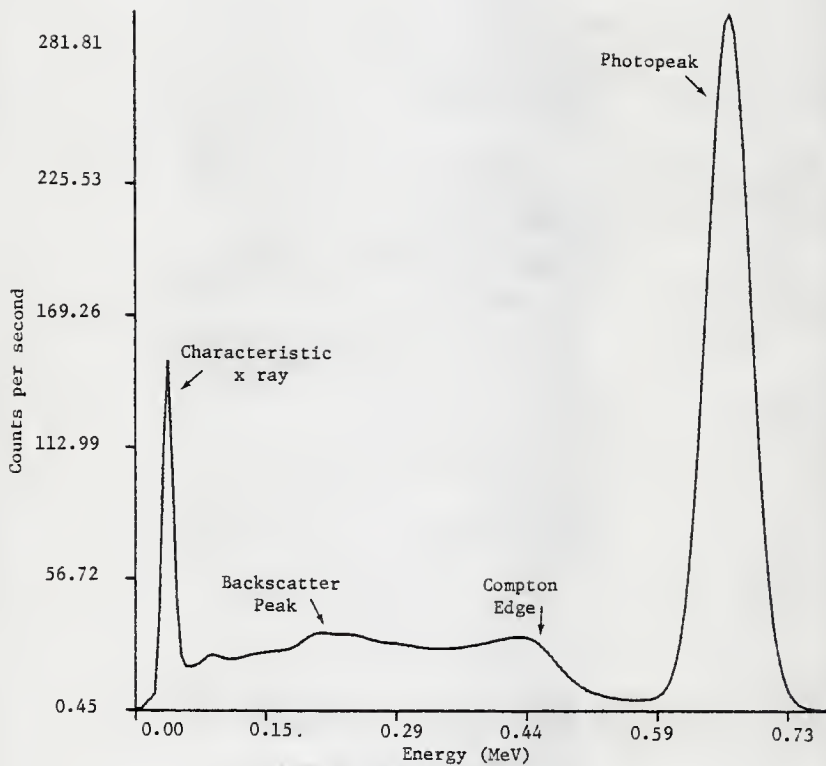


Fig. 17. Cs-137 response function

energy of the incident photon is subdivided between the various secondary electrons. This effect would be expected to be significant for initial energies above 400 keV where multiple interactions are predominant<sup>9</sup>. Some additional broadening occurs due to nonuniform photoelectron production at the photocathode and the subsequent collection at the first dynode.

The broadening of the lower side of the photopeak is influenced by the escape of the secondary photon after undergoing two or more Compton interactions. Shallow angle scattering of the incident photons before reaching the detector is another contributing factor. The shape of the high energy side of the photopeak is affected in high count rate situations by the superposition of one or more pulses at the photocathode. This distortion is commonly referred to as "pile-up".

The Compton distribution, or plateau, represents a series of events in which scattered photons escape the crystal without depositing all of their initial energy in the detector. Since the energy of the secondary photon is a continuous function of the scattering angle, the Compton plateau extends from zero energy up to the energy corresponding to the maximum amount of energy that can be transferred to an electron in a single event. This cutoff is commonly called the Compton edge and corresponds to a  $180^\circ$  angle scattering event. In practice, the Compton edge is not a sharp cutoff because of shallow angle and multiple scatters which tend to fill in the "valley" between the Compton edge and the photopeak.



The backscatter peak is caused by those photons which have experienced a large angle scattering event prior to reaching the crystal. As can be seen in Fig. 18, the energy of the recoil photon changes very slightly for scattering angles greater than  $120^\circ$ . Therefore, a peak is formed as a result of those photons depositing all of their energy in the crystal and is centered around the channel corresponding to the scattered photon energy after a  $180^\circ$  Compton scatter.

The characteristic x ray also shown in Fig. 17, is a result of an internal conversion process within the daughter of the isotope under consideration. As such, this process in itself represents a monoenergetic photon source and although sometimes proving useful in identification, often complicates the interpretation of the response of the system to the primary gamma emission at very low energies.

A very low energy "iodine escape peak" is often noticed in a NaI pulse height distribution in association with low energy photon sources. During the energy deposition process, iodine atoms within the NaI crystal are excited and emit x rays at approximately 29 keV upon reversion to the ground state. When dealing with low energy sources such as an internal conversion x ray, the point of interaction is usually close to the surface of the crystal since the attenuation coefficient for NaI increases significantly at low energies. Being produced near the periphery of the crystal, the de-excitation x rays have a high probability of escaping the crystal. The escape of the x ray causes the energy deposited in the crystal to be 29 KeV below the energy of the incident photon and an iodine escape peak is formed.

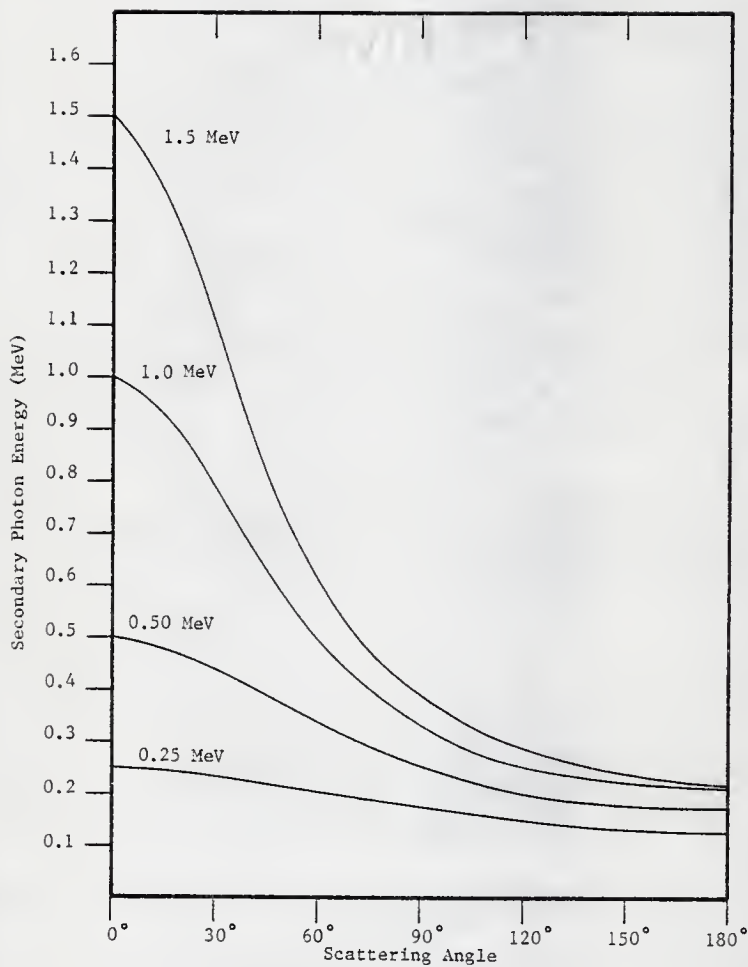


Fig. 18. Secondary photon energy as a function of scattering angle.

Two other escape peaks may be encountered when dealing with source energies above 1.1 MeV. As a consequence of pair production, two 0.51 MeV annihilation photons are produced. One or both of these photons may escape the crystal without an interaction resulting in a first- or second-escape peak, respectively.

### 3.1.2 Theory of Unfolding

The pulse height distribution of the output voltage pulses of a scintillation spectrometer,  $C(V)$ , is related to the incident gamma-ray fluence,  $\phi(E')$ , by

$$\int_0^{E_{\max}} dE' R(E', V) \phi(E') = C(V) \quad (3.1-1)$$

where  $R(E', V)$  is the probability that an incident photon of energy  $E'$  will produce an output pulse within unit voltage about  $V$ , and  $E_{\max}$  is the maximum energy of the primary spectrum. The function  $R$  is often referred to as the response surface of the spectrometer because it describes the response of the system to photons of a given incident energy,  $E'$ . The binning or discretization process performed by the MCA can be written as

$$C_i = \int_{\Delta V_i} dV \int_0^{E_{\max}} dE' R(E', V) \phi(E') \quad i=1, 2, \dots, N \quad (3.1-2)$$

or

$$C_i = \int_0^{E_{\max}} dE' \phi(E') R_i(E') \quad i=1, 2, \dots, N \quad (3.1-3)$$

where

$$R_i(E') = \int_{\Delta V_i} dV R(E', V) \quad i=1, 2, \dots, N, \quad (3.1-4)$$

is called the "spectrometer response function" and physically may be interpreted as the expected number of counts observed in channel  $i$  of the pulse height distribution due to a unit fluence of photons of energy  $E'$ . In this formulation  $N$  is the number of channels in the pulse height spectrum and  $C_i$  is the observed number of counts in channel  $i$  corresponding to the observed number of voltage pulses ranging from  $V_i$  to  $V_i + \Delta V_i$  in amplitude.

The response surface of the spectrometer, a typical representation of which is shown in Fig. 19<sup>10</sup>, can be determined in a variety of ways. Much effort has been expended in using Monte Carlo techniques to predict the response of a specific detection system to a source of monoenergetic photons<sup>11-13</sup>. Although excellent results have been obtained, the system response is highly sensitive to parameters such as detector size and collimator geometry which necessitates independent calculations for each detection system. This procedure is prohibitive in most cases because of the large computational effort involved.

A second technique involves experimentally measuring the response of the system at several discrete energies and using elaborate interpolation schemes to calculate the response at those energies which are not available experimentally<sup>14,15</sup>. This technique is widely used although the source preparation, measurements, background corrections and calibration matching also make this technique quite onerous to use.

To obtain the actual energy distribution of the incident photon fluence from the measured pulse-height distribution, it is convenient to restate Eq. (3.1-3) in matrix notation as

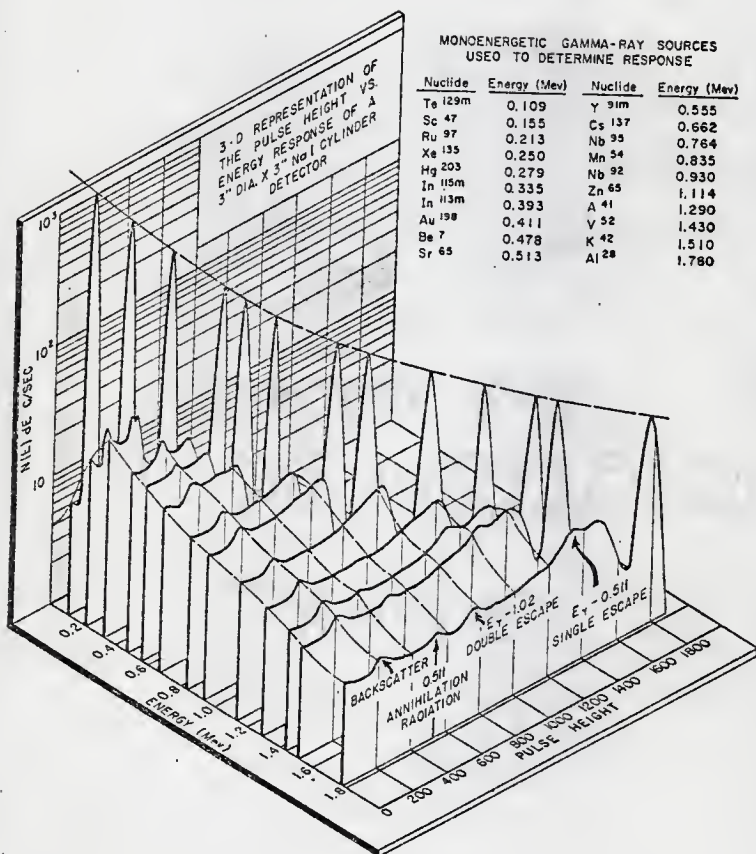


Fig. 19.— Typical spectrometer response surface. (From R. L. Heath, Ref. 10)

$$\underline{C} = \underline{R} \underline{\phi} \quad (3.1-5)$$

where  $C_i$  is the number of counts in channel  $i$ ,  $R_{ij}$  represents the number of counts in channel  $i$  per unit fluence in energy interval  $j$ , and  $\phi_j$  represents the incident photon fluence in energy interval  $j$ .

Although direct solution of Eq. (3.1-5) for  $\phi_j$  is possible using standard inversion techniques, unphysical oscillations and negative values often appear in the results<sup>14</sup>. Therefore, various iterative schemes have been devised in an effort to consistently obtain a stable, physically significant solution<sup>16-18</sup>.

### 3.1.3 Derivation of the SEGO Method

The technique used in this study to unfold the measured skyshine spectra was developed by Young and Burrus<sup>4</sup> and is designed to correct for the distortions in the spectrum due to partial energy deposition in the crystal while at the same time preserving the inherent spectral smoothing caused by the finite resolution of the detector system. In this technique, the Compton plateau and the various scattering and escape peaks are "stripped" from the observed pulse-height distribution. The resulting spectrum is an approximation to the incident radiation field which has been broadened according to the system resolution.

The observed pulse height distribution is the result of two distinct processes, the first being the deposition of energy within the crystal, the second being the broadening effect in converting the deposited energy into a voltage pulse. The energy deposition process can be formulated in terms of a function  $U$  defined as

$$U(E, E') dE' = \left( \begin{array}{l} \text{the probability that an incident photon of} \\ \text{energy } E \text{ will deposit energy in the crystal} \\ \text{within } dE' \text{ about } E' \end{array} \right)$$

Similarly, the spectral broadening can be expressed by

$$S(E, E') dE' = \left( \begin{array}{l} \text{the probability that the deposition of energy } E \text{ in} \\ \text{the crystal will produce a PMT voltage pulse} \\ \text{corresponding to a photon with energy in } dE' \text{ about } E' \end{array} \right)$$

Physically, the incident spectrum due to a monoenergetic source is ideally represented by a delta function at some source energy  $E$ . This energy is deposited, either in part or in full, in the crystal. The response of the crystal is then broadened by the trailing electronics. The assumption made in the development of the SEGO method is that the pulse height distribution obtained from the above sequence of events is equivalent to what would be observed if the incident spectrum was first smeared by the inherent resolution of the spectrometer and then detected by a detection system with perfect resolution. With this alternative viewpoint the spectrometer response function,  $R_i(E')$ , of Eq. (3.1-4) can be expressed in terms of  $U$  and  $S$  as

$$R_i(E') = \int_{\Delta E_i} dE \int_0^{E_{\max}} dE'' U(E'', E) S(E', E'') \quad i=1, 2, \dots, N. \quad (3.1-6)$$

It should be pointed out that in this formulation the smearing function  $S$ , is a function of the source energy  $E'$  and not of the energy deposited in the crystal,  $E$ . Equation (3.1-6) can be rewritten as

$$R_i(E') = \int_{\Delta E_i} dE \sum_{k=1}^N \int_{\Delta E_k} dE'' U(E'', E) S(E', E'') \quad i=1, 2, \dots, N. \quad (3.1-7)$$

If one assumes that  $U$  and  $S$  vary slowly across any energy bin  $\Delta E_k$  or  $\Delta E_i$ , Eq. (3.1-7) becomes

$$R_i(E') \approx \sum_{k=1}^N U(E_k, E_i) \Delta E_k \Delta E_i S(E', E_k) \quad i=1, 2, \dots, N. \quad (3.1-8)$$

With the definition

$$U_{ik} = \Delta E_k \Delta E_i U(E_k, E_i), \quad (3.1-9)$$

Eq. (3.1-8) can be expressed as

$$R_i(E') = \sum_k U_{ik} S(E', E_k) \quad i=1, 2, \dots, N. \quad (3.1-10)$$

Substitution of Eq. (3.1-10) into Eq. (3.1-3) yields

$$C_i = \sum_{k=1}^N U_{ik} \int_0^{E_{\max}} dE' \phi(E') S(E', E_k) \quad i=1, 2, \dots, N. \quad (3.1-11)$$

Notice that the quantity under the integral is merely the incident fluence which has been smeared according to the system resolution.

One can therefore define

$$\tilde{\phi}(E_k) = \int_0^{E_{\max}} dE' \phi(E') S(E', E_k) \quad (3.1-12)$$

as the broadened, incident spectrum. Substitution of this definition into Eq. (3.1-11) then yields

$$C_i = \sum_{k=1}^N U_{ik} \tilde{\phi}(E_k) \quad i=1, 2, \dots, N. \quad (3.1-13)$$



It is the discretized, smeared incident spectrum,  $\tilde{\phi}(E_k)$ , that is solved for in the SEGO code.

Equation (3.1-13) represents a set of  $N$  equations in  $N$  unknowns, namely the  $\tilde{\phi}(E_k)$ 's. The matrix elements  $U_{ik}$  are a discrete representation of the response surface of the ideal spectrometer (i.e., a spectrometer with perfect resolution). Physically,  $U_{ik}$  may be interpreted as the probability a count will be recorded in channel  $i$  per incident photon on the NaI crystal whose energy corresponds to channel  $k$ . The realistic assumption is made that it is impossible for a photon of energy  $E''$  to deposit an energy  $E$  in the crystal with  $E > E''$ . Therefore,  $U_{ik}$  is identically zero for those values of  $i > k$ . However, this assumption ignores the effects of sum peaks where two photons deposit their entire energy in a time interval too short to be resolved by the crystal. Also ignored are pile-up effects.

Under this assumption, the system of equations defined by Eq. (3.1-13) becomes triangular in nature. Denoting  $\tilde{\phi}(E_k)$  by  $X_k$ , Eq. (3.1-13) can be written as

$$\begin{aligned}
 U_{11}X_1 + U_{12}X_2 + U_{13}X_3 + \dots + U_{1N}X_N &= C_1 \\
 U_{12}X_2 + U_{23}X_3 + \dots + U_{2N}X_N &= C_2 \\
 U_{33}X_3 + \dots + U_{3N}X_N &= C_3 \\
 &\vdots \\
 U_{NN}X_N &= C_N.
 \end{aligned} \tag{3.1-14}$$

This system can be immediately solved by first solving for  $X_N$  and working backwards to  $X_1$ . In general, the solution can be written as

$$X_N = \frac{C_N}{U_{NN}}$$

$$X_\ell = \left( C_\ell - \sum_{n=\ell+1}^N U_{\ell n} X_n \right) / U_{\ell\ell}, \quad \ell=N-1, N-2, \dots, 1. \quad (3.1-15)$$

This solution (which is related to the true incident spectrum by Eq. (3.1-12)) gives an approximate representation of the incident fluence on the NaI crystal which is corrected for those photon-crystal interactions which do not deposit all of the photon's energy in the crystal, i.e., only interactions leading to counts in the photopeaks are retained. Moreover, the system resolution has been imposed on this unfolded spectrum since it is fruitless to try to resolve energy structure outside of the inherent resolution of the spectrometer.

In the preceding unfolding description, the statistical uncertainty in the observed values of  $C_i$  has been ignored. However, due to the statistical nature of the detection process, the measured distribution is only one member of a family of possible results. A stochastic perturbation technique is used in the SEGO code to evaluate the uncertainty in the unfolded result. This method eliminates the need for the inversion of the entire response matrix which would be required if standard error propagation techniques were used. Given a measured pulse-height distribution,  $C_i$ ,  $i=1,2,\dots,N$ , each with a corresponding standard deviation,  $S_i$ ,  $i=1,2,\dots,N$ , one can stochastically perturb the given spectrum by adding to each  $C_i$  a randomly selected normal deviate chosen from the Gaussian distribution with mean zero and standard deviation

$S_i^4$ . By generating and unfolding several of these perturbed spectra, the standard deviation of the unfolded measured spectrum can be estimated from the range of the results. In the SEGO code, three spectra generated by perturbing each channel in the above fashion, are unfolded along with the original observed spectrum.

#### 3.1.4 Description and Construction of the Response Matrix

The distinguishing characteristic of the SEGO method is that each response function,  $U_{ik}$ , is constructed through the superposition of appropriately placed rectangles as suggested by Hyodo<sup>4</sup>. This concept is illustrated in Fig. 20, where one column of the U matrix is shown in the idealized form. Notice that each feature of the response function is approximated by a discrete, sharp component. A long rectangle extending from zero energy to the Compton edge is used to approximate the Compton plateau. The "valley fill function", located immediately below the photopeak is used to approximate those counts which occur between the full energy peak and the Compton edge. Other features of the response function include the representation of the first- and second-escape peaks and the backscatter peak. Additional features could be added to account for other minor structures if necessary.

As is obvious from Fig. 20, large portions of the idealized response functions are flat. This flatness is used in the SEGO code to reduce significantly the execution time. Returning to Eq. (3.1-14) and subtracting equation (j+1) from the j-th equation for  $j=1..N$ , one obtains

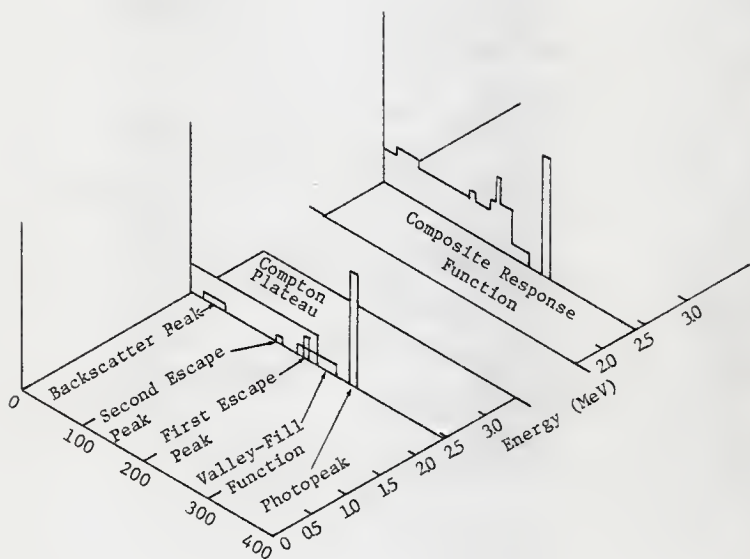


Fig. 20. Hyodo response function (After M. H. Young, et al., Ref. 4).

$$\begin{aligned}
 U_{11}X_1 + X_2(U_{12}-U_{22}) + X_3(U_{13}-U_{23}) + \dots + X_N(U_{1N}-U_{2N}) &= C_1-C_2 \\
 U_{22}X_2 + X_3(U_{23}-U_{33}) + \dots + X_N(U_{2N}-U_{3N}) &= C_2-C_3 \\
 U_{33}X_3 + \dots + X_N(U_{3N}-U_{4N}) &= C_3-C_4 \\
 \vdots &\vdots \\
 U_{NN}X_N &= C_N
 \end{aligned} \tag{3.1-16}$$

With this transformation of the system, many coefficients are now zero. The only nonzero components are located where the  $U_{ik}$ 's have discontinuities. Thus the transformed  $U$  matrix is still triangular and now is only sparsely filled. The summation in Eq. (3.1-15) needs only to be carried out over the nonzero components of which there are only ten: the upper and lower edges of the backscatter peak, the first- and second-escape peaks and the "valley fill" function, plus the Compton edge and the photopeak. This transformation is reversed during the solution of the system.

One of the advantages of the Hyodo response functions is that the spectrum features vary fairly slowly with energy. Thus it is feasible to tabulate them at a few energies and use linear interpolation to obtain the necessary values for other energies during the course of the computation. This property eliminates the need to store the entire response matrix.

Typically, eight parameters are needed to define a Hyodo-type response function for an incident monoenergetic photon source of energy  $E'$ . They are:

- 1) EF, defined as the ratio of the total counts in the spectrum to the number of photons reaching the crystal face,
- 2) PT, defined as the ratio of the area of the photopeak to the area of the total spectrum (peak to total ratio),
- 3) ES, defined as the first-escape peak to total ratio,
- 4) EC, defined as the second-escape peak to total ratio,
- 5) BK, defined as the backscattering peak to total ratio,
- 6) VH, defined as the valley to total ratio,
- 7) VU, defined as the valley upper edge energy, and
- 8) VL, defined as the valley width in energy units.

Experimental response functions were measured using Am-241, Hg-203, Cs-137, and Co-60 calibration sources which were positioned on the detector axis at a distance of 69.85 cm. Three response functions from each source were measured to ensure reproducibility. Long count times were also used in order to minimize the statistical uncertainties in the result. An appropriate background spectrum was subtracted from each experimental response function before analysis.

An initial response matrix was calculated from these 70-cm experimental response functions. Since all of the sources emitted photons of two different energies, some approximations were necessary in order to treat them as monoenergetic sources. For example, in the case of Cs-137, the area of the 32.88 keV x ray must not be included in the calculation of the unfolding parameters for the .662 MeV photon. To this end, the x ray peak was eliminated by assuming that the Compton plateau was continuous through the region beneath the peak. Since there should be very little, if any, contribution to the Compton continuum from the x ray, the resulting spectrum should very closely approximate the response of the system to a monoenergetic source of 0.662 MeV photons.

In the case of Co-60, the approximation described was not valid since source photons of both energies (1.173 and 1.332 MeV) make a significant contribution to Compton plateau. Therefore, the experimental Co-60 response function was treated as monoenergetic source with an energy of 1.253 MeV.

The valley upper edge was determined from the lower side of the photopeak. The sharply increasing region of the peak was used to define a line which would intersect at the approximate lower edge of the photopeak. The valley lower edge was at first taken to be the Compton edge, but was later adjusted to extend slightly below this point.

The initial results obtained from unfolding the four calibration spectra with the 70-cm parameters were not acceptable so individual values were adjusted by trial and error until most of the non-photopeak features were eliminated and the photopeak area was within a few percent of the expected value. The unfolded 70-cm response functions are shown in Fig. 21, where although the various secondary structures have not been completely eliminated, the area outside of the photopeak is less than 3% in all cases. The optimized 70-cm unfolding parameters are shown in Table 3.

Because the effective source/detector distance for the skyshine incident flux would be much greater than 70-cm, a significant change in the total or intrinsic efficiency of the detector would be experienced. The intrinsic efficiency,  $\epsilon_c(E)$ , defined as the probability that a photon incident upon the detector face will interact within its active

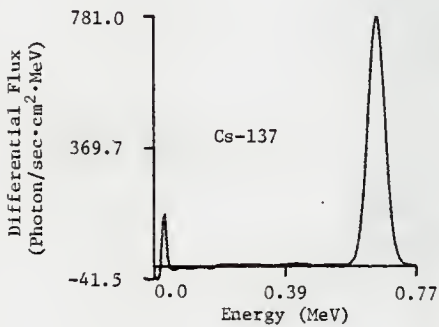
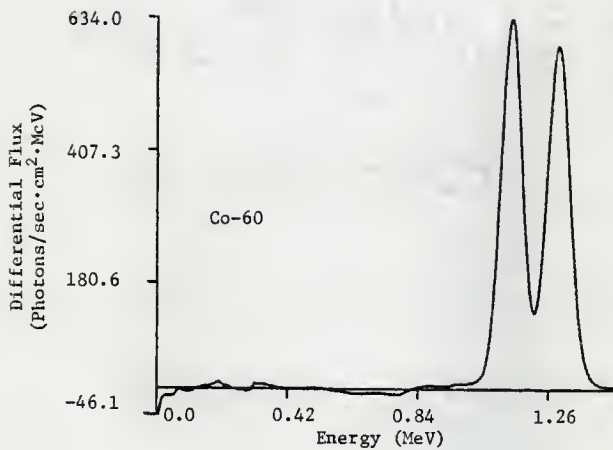


Fig. 21. Unfolded 70-cm response functions.



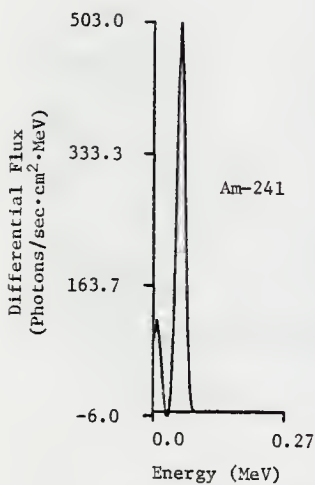
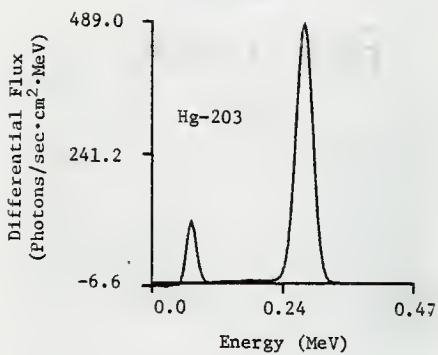


Fig. 21. continued

Table 3. Optimized 70-cm Unfolding Parameters

E (MeV)	EF	PT	ES	EC	BK	VH	VU	VL
0.0	1.113	0.9525	0.0	0.0	0.0070	0.0	0.0	0.0
0.2	1.083	0.8304	0.0	0.0	0.0110	0.1069	0.1738	0.0859
0.4	1.052	0.7239	0.0	0.0	0.0160	0.0958	0.3610	0.1240
0.6	1.0216	0.6312	0.0	0.0	0.0210	0.0898	0.5481	0.1620
0.8	.9912	0.5502	0.0	0.0	0.0250	0.0858	0.7352	0.2001
1.0	.9607	0.4797	0.0	0.0	0.0300	0.0828	0.9224	0.2381
1.2	.9301	0.4182	0.005	0.004	0.0340	0.0804	1.1095	0.2762
1.4	.8996	0.3646	0.010	0.008	0.0390	0.0785	1.2967	0.3142
1.6	.8691	0.3179	0.015	0.012	0.0440	0.0768	1.4838	0.3523

volume, can be calculated as<sup>19</sup>

$$\epsilon_t(E) = \frac{\int_{\Omega_0} (1 - e^{-\mu x}) d\Omega}{\Omega_0}, \quad (3.1-17)$$

where  $\Omega_0$  is the solid angle subtended by the crystal.

In the case of a point source located on the axis of a right cylindrical detector of height  $t$  and radius  $r$ , as illustrated in Fig. 22, Eq. (3.1-17) becomes

$$\epsilon_t(E) = \frac{\int_0^{\theta_m} d\theta \sin\theta (1 - e^{-\mu \cdot x(\theta)})}{\int_0^{\theta_m} d\theta \sin\theta} \quad (3.1-18)$$

where

$$x(\theta) = \begin{cases} \frac{t}{\cos\theta} & \text{for } 0 \leq \theta \leq \theta' \\ \frac{r-h \cdot \tan\theta}{\sin\theta} & \text{for } \theta' \leq \theta \leq \theta_m, \end{cases} \quad (3.1-19)$$

$$\theta_m = \tan^{-1}(r/h), \quad (3.1-20)$$

$$\theta' = \tan^{-1}\left(\frac{r}{t+h}\right) \quad (3.1-21)$$

and  $h$  is the source/detector distance.

The attenuation coefficient,  $\mu$ , used for these calculations is the "narrow beam, total, without coherent" ( $\left(\frac{\mu}{\rho}\right)_{\text{tot}, t\text{-coh}}$ )<sup>20</sup> since for calculations of crystal efficiencies one is interested only in

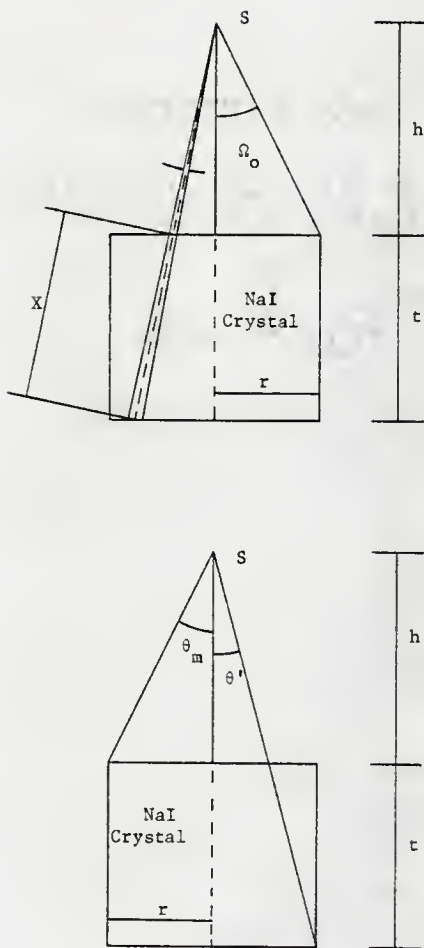


Fig. 22. Geometry for the calculation of intrinsic efficiency.

those interactions which result in the deposition of energy. From Fig. 23, it is seen that the intrinsic efficiency changes only slightly for source to detector distances greater than 400 cm. Therefore, Cs-137 and Co-60 response functions were measured at approximately 400 cm to obtain unfolding parameters to correct for this effect. These measured response functions were used to adjust the EF and PT values while leaving all other parameters unchanged.

Figure 24 shows the unfolded 400-cm response functions while Table 4 contains the optimized values of the response surface parameters used in unfolding the skyshine data. As with the 70-cm unfolded response functions, the final 400-cm results represent a compromise between obtaining the known photopeak area and correctly compensating for the Compton plateau and secondary peaks. The analysis of the second set of response functions was complicated by the presence of a large steel mass close to the sources during the measurements. This resulted in an abnormally large backscatter peak which would not appear in an ideal response function. Therefore, the unfolded 400-cm response functions should still contain a significant backscatter peak contribution to avoid over compensation when unfolding the skyshine spectra.

The negative values observed in the unfolded results point out a weakness in the SEGO method. Since the stripping proceeds from high energy to low, any errors in the response matrix formulation will be accumulated as the calculation progresses and will ultimately be manifested in the low energy portion of the spectrum. Therefore, an accurate

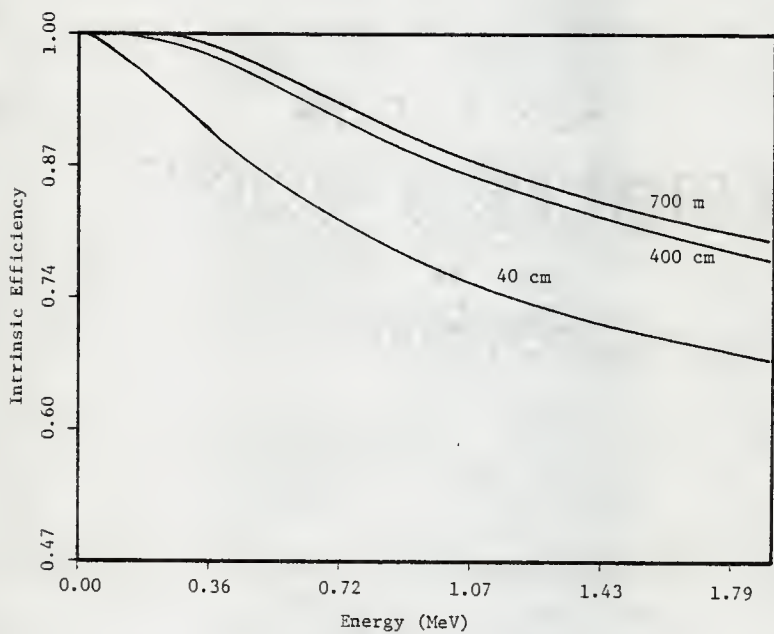


Fig. 23. Intrinsic efficiency results for the NaI crystal used in this study as a function of source/detector distance, h.

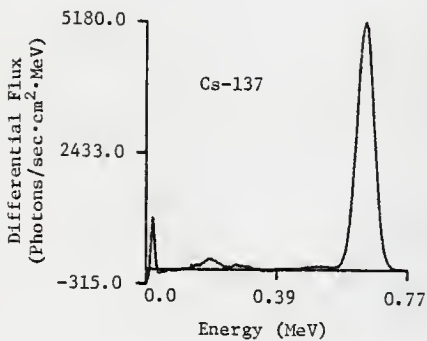
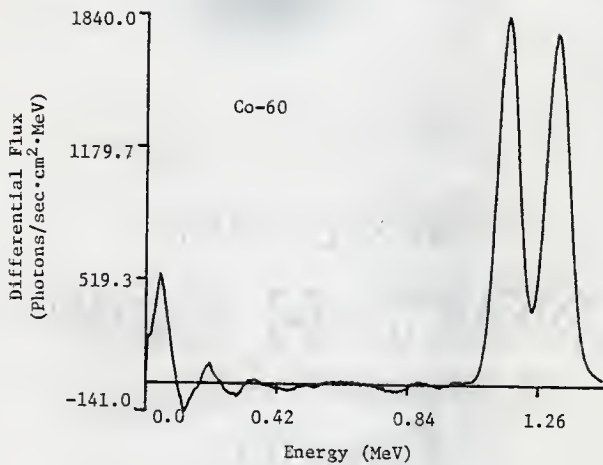


Fig. 24. Unfolded 400-cm response functions.

Table 4. Optimized 400-cm Unfolding Parameters

E(MeV)	EF	PT	ES	EC	BK	VH	VU	VL
0.0	1.1810	1.00	0.0	0.0	0.0	0.1400	0.0	0.0
0.2	1.1810	0.8034	0.0	0.0	0.0120	0.1000	0.1738	0.1050
0.4	1.1810	0.6649	0.0	0.0	0.0120	0.0600	0.3480	0.1200
0.6	1.1756	0.5719	0.0	0.0	0.0130	0.0240	0.5481	0.2000
0.8	1.1548	0.5118	0.0	0.0	0.0140	0.0225	0.7352	0.2000
1.0	1.1235	0.4720	0.0	0.0	0.0143	0.0234	0.9224	0.2200
1.2	1.0810	0.4396	0.0050	0.0040	0.0145	0.0234	1.1200	0.2300
1.4	1.0266	0.4019	0.0100	0.0080	0.0150	0.0230	1.2967	0.2400
1.6	0.9597	0.3464	0.0150	0.0120	0.0150	0.0230	1.4838	0.2500

Table 5. Unfolding Parameters Used by Radiation Research Associates<sup>3</sup>

E(MeV)	EF	PT	ES	EC	BK	VH	VU	VL
0.0	1.1750	1.000	0.0	0.0	0.0	0.1700	0.0	0.000
0.2	1.1750	0.795	0.0	0.0	0.012	0.1100	0.164	0.080
0.4	1.1720	0.680	0.0	0.0	0.012	0.0750	0.348	0.120
0.6	1.1550	0.598	0.0	0.0	0.013	.0425	0.540	0.200
0.8	1.1290	0.530	0.0	0.0	0.013	0.0355	0.736	0.200
1.0	1.1020	0.478	0.0	0.0	0.0135	0.0225	0.920	0.210
1.2	1.0800	0.435	0.005	0.004	0.0145	0.0229	1.120	0.230
1.4	1.0610	0.395	0.010	0.008	0.0145	0.0229	1.300	0.240
1.6	1.0440	0.362	0.015	0.012	0.0150	0.0229	1.495	0.250



response surface is imperative if an accurate, physically meaningful result is to be obtained, especially at low energies.

Since the originally calculated unfolding parameters yielded unsatisfactory results, a trial and error approach was used to adjust the response surface parameters to obtain better results. Complicating this procedure is the limitation of this method's accuracy due to its reliance upon discrete, idealized response functions. Therefore the experimenter is called upon to make a judgemental decision as to whether or not the best possible result has been obtained within the limitations of the technique.

It has been this author's experience that in using the SEGO code one must be satisfied with a somewhat less than ideal result. The three criteria used in adjusting the unfolding parameters were proper photopeak area and a peak-to-total ratio close to unity without any negative values in the unfolded spectra. While the former criterion was relatively easy to achieve, it was not possible to achieve the latter criteria. Thus an effort was made to minimize the negative contributions in the unfolded result although it could not be eliminated completely.

Since there is a great deal of judgement involved in generating the response matrix to be used with the SEGO code, it is to be expected that two different experimenters working with data from the same spectrometer will generate different sets of unfolding parameters. As an example, the response matrix generated in this work is not identical to the one published by Radiation Research Associates<sup>3</sup> and which is given

in Table 5. The magnitude of this effect is shown in Fig. 25, where an unfolded Cs-137 spectrum is shown using either the KSU or RRA parameters. While some differences are apparent, they are certainly not significant.

One difficulty encountered during the unfolding of the skyshine data was the presence of an iodine escape peak at approximately 20 keV. Since this feature is a result of a non-ideal detector, it should have, in principle, been removed during the unfolding. It would have been relatively easy to include this structure in the Hyodo response functions except that none of the experimentally measured response functions contained an iodine-escape peak. Since data was not available from which to incorporate the iodine-escape peak into the response matrix, this peak was artificially suppressed by linearly extrapolating the spectrum to zero using the two channels immediately above the peak to define the expected rapid decrease in the energy flux as the spectrum energy decreases to zero.

### 3.1.5 Determination of Gain and Zero Channel

In order to unfold the skyshine spectra, the gain and zero-intercept of each spectrum must be accurately known so that the channel/energy relationship may be calculated. A calibration spectrum containing five major photopeaks was taken before and after each skyshine spectral measurement. The centroid of each photopeak was calculated by performing a least squares fit of the photopeak to a Gaussian. An average spectrum gain and zero intercept was then obtained by performing a linear least-squares fit to the combined data from both calibration spectra. In this way, any gain shift that might have occurred during the measurement due

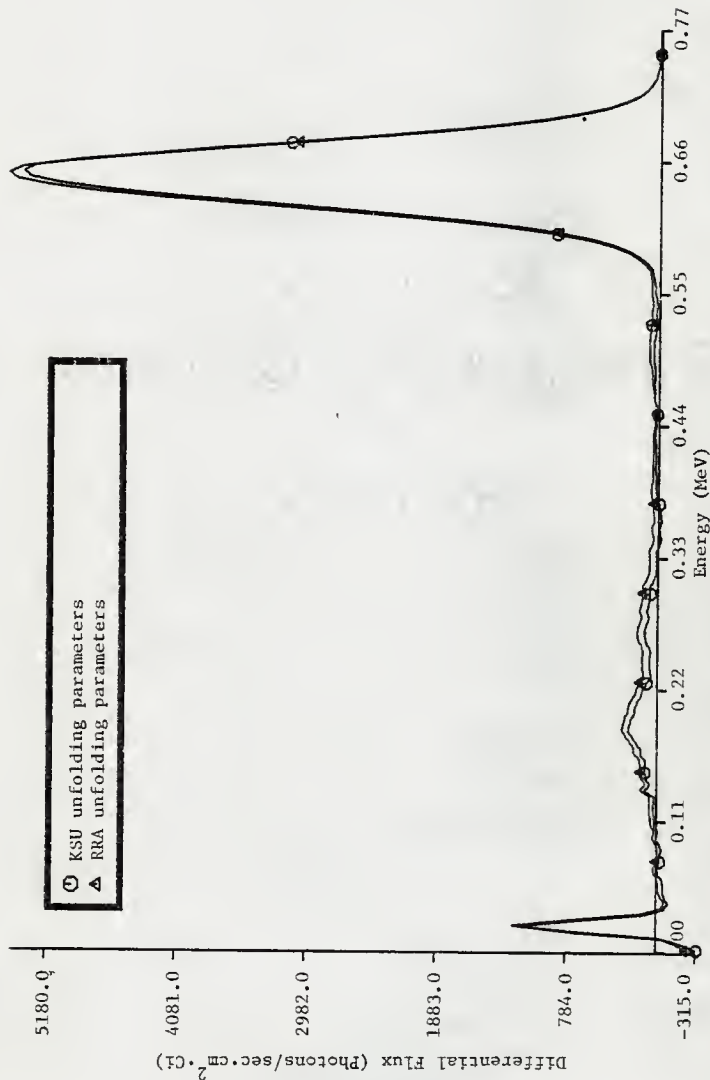


Fig. 25. Comparison of unfolded Cs-137 spectra using either the KSU or RRA unfolding parameters.

to an instrument or ambient temperature change, will be partially compensated for by averaging the calibration data in this manner.

### 3.2 Spectral Comparisons

One of the primary purposes of the skyshine experiment was to obtain skyshine energy spectra against which calculated results could be compared. With such comparisons, the accuracy of various photon transport models can be assessed.

From August through November, 1977, three sets of spectral measurements were made of the skyshine radiation field produced by the three source configurations described in Chapter 2. Source/detector distances for these measurements ranged from 100 to 700 meters (at 100 m intervals) for the unshielded and 8" shielded source measurements but extended only to 500 meters for the 16" shield cases before the background signal overshadowed the skyshine signal.

Two dimensional, discrete ordinates transport calculations were performed by Radiation Research Associates<sup>3</sup>, using the DOT-3.5 code<sup>5</sup> for all source/detector distances and source configurations. In this section the spectral results of these calculations are compared to the unfolded spectra obtained with the NaI spectrometer.

#### 3.2.1 Comparison of Unshielded Spectra

The unshielded source configuration consisted of an upward collimated 150° conical beam of Co-60 radiation. The unfolded skyshine spectra (corrected for background) for this configuration are shown in Fig. 26 for all source/detector distances. One immediately notices that the spectral shape remains relatively constant as the source/detector

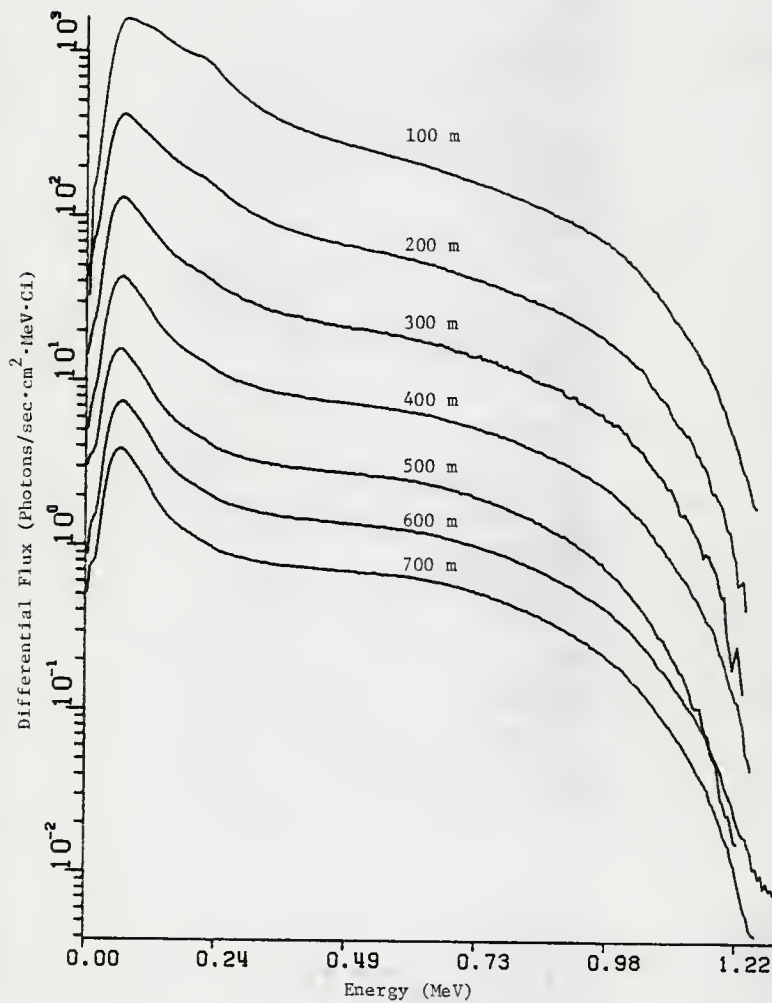


Fig. 26. Comparison of unfolded NaI spectra for the unshielded source configuration.

distance varies although some changes occurs as the source/detector distance increases. The slightly larger low energy component in the 100 m spectrum as compared to the 700 m result is primarily due to in-silo scattering of the source photons. The result of this scattering would be that the upward collimated radiation field would contain multiply scattered low energy photons, as well as uncollided C<sup>60</sup>-60 gamma photons. Each spectrum is also observed to contain a rather dominant plateau region between 0.25 and 0.75 MeV. While being somewhat distorted in the 100 m case, it is readily apparent in the 700 m example.

The effect of the in-silo scattering phenomena on the total skyshine exposure rate has been investigated by Ryufuku<sup>21</sup> of the Japan Atomic Energy Research Institute (JAERI) using an eleven group energy structure with the DOT-3 transport code. The effect of in-silo scattering on the skyshine energy spectrum is shown in Fig. 27 for the NaI detector geometry. As was expected, the inclusion of in-silo scattering results in a slight softening of the spectrum, particularly at small source/detector distances. However, as shown in Fig. 28, this source of scattered photons has a negligible effect upon the total exposure rate.

Two sets of DOT calculations were performed by RRA for the unshielded source configuration using a two dimensional r-z geometry. First, a 39 energy group structure was used with an S<sub>16</sub> angular mesh and a P<sub>5</sub> cross section representation. Vacuum boundary conditions were used except at r=0 where a reflection condition was imposed. To minimize streaming effects in the calculations, a first collision source distribution was determined and used in the subsequent DOT calculations.



Fig. 27. Comparison of energy spectra with and without in-silo scattering. Source to detector distance is 100 meters.

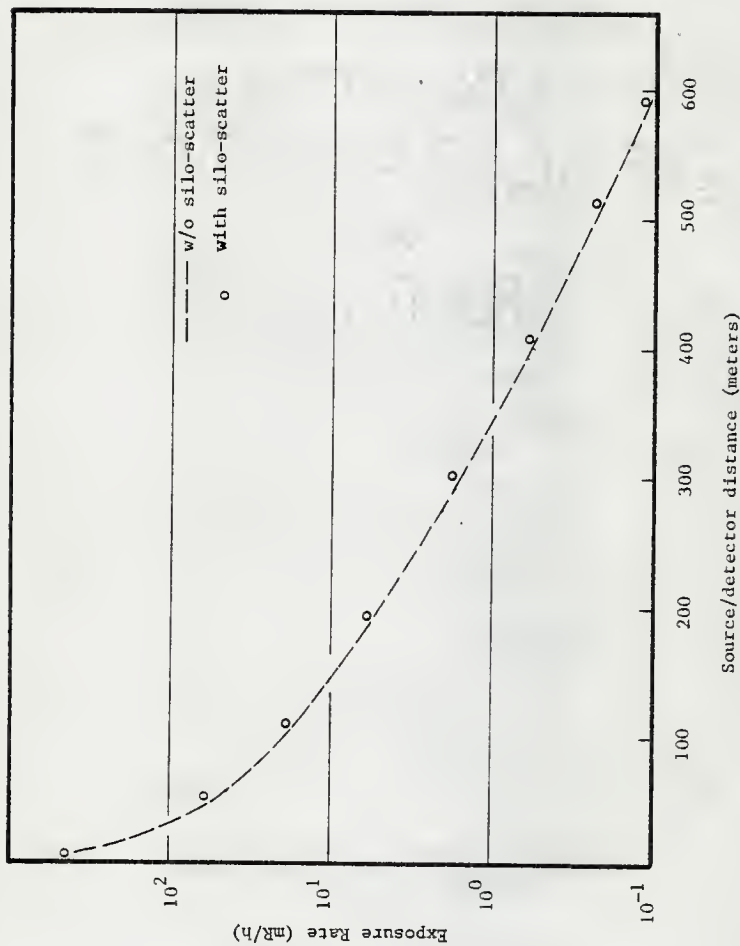


Fig. 28. Effect of in-silo scattering on skyshine exposure rate.



Second, since the 39 group calculations were extremely expensive, it was decided to use a less expensive (and presumably less accurate) 10 energy group model for routine analysis. In an effort to preserve some of the accuracy of the fine group calculations, a sensitivity study was done in which the original 39 group energy structure was collapsed into 10 groups, each of which contributed approximately the same amount to the total exposure rate. This optimized 10 group structure was used with a reduced angular grid and cross section representation ( $S_{12}$  and  $P_3$ , respectively) in DOT-3.5, again with a first collision source distribution. Complete details of the modeled geometry and computational steps are given in Reference 3.

To aid in the comparison of the 39 group results with the measured spectra, a Gaussian smoothing technique was applied to the calculated group fluxes. With this procedure, the calculated spectra (in the form of a histogram) can be smoothed, or smeared, with the same resolution as the NaI spectrometer which was determined experimentally. Specifically, the resolution of the NaI spectrometer system,  $K(E)$ , was found to be represented by<sup>3</sup>

$$K(E) = 0.0745E^{-0.44} \quad (3.2-1)$$

where  $R(E)$  is the fractional resolution, or line width, defined as<sup>19</sup>

$$K(E) = \frac{FWHM}{C_{max}} \quad (3.2-2)$$

where  $C_{max}$  is the pulse height (MeV) corresponding to the centroid of the photopeak and FWHM is the pulse height width (MeV) between the

points at which one-half the maximum value occurs (i.e., the full width at half maximum). Since the photopeak for a NaI spectrum can be well represented by a Gaussian, the quantity  $K$  can be related to the standard deviation of a normal distribution with mean  $E_j$  by<sup>19</sup>

$$K(E_j) = \frac{2.35 \sigma(E_j)}{E_j} \quad (3.2-3)$$

Therefore, denoting the smoothed differential flux in channel  $i$  by  $\tilde{\phi}_i$ , and the calculated (histogram) differential flux in group  $j$  by  $\phi_j$ , the smoothed spectrum can be represented by

$$\tilde{\phi}_i = \sum_{j=1}^{NG} S_{ij} \phi_j \quad i=1,2,\dots,N \quad , \quad (3.2-4)$$

where  $NG$  is the number of group fluxes in the calculated spectra,  $N$  is the number of channels in the smeared spectrum, and

$$S_{ij} = \frac{\Delta E_j}{\sigma_j \sqrt{2\pi}} \exp \left[ -(E_i - E_j)^2 / 2\sigma_j^2 \right] \quad . \quad (3.2-5)$$

The result of this smearing procedure on the calculated group fluxes is a "smooth spectrum" which should very closely approximate the unfolded results if the transport model is sufficiently accurate. Unfortunately this procedure could not be applied to the 10 group results because the energy group width used in the calculations was much larger than the resolution width of the spectrometer and such a smoothing technique would introduce artificial structure into the smoothed spectrum.

A comparison between the calculated and unfolded incident unshielded skyshine energy spectra is shown in Fig. 29 for three representative source/detector distances. The smooth curves with identifying symbols are the unfolded NaI results. (The symbols are located at every fifteenth data point.) The other smooth curves (without symbols) are the 39 group Gaussian smoothed results calculated by DOT, while the histograms represent the 10 group results. In the 100 meter case, the agreement is very good for energies above 0.50 MeV. Below this point the measured spectrum is considerably softer than that of the DOT results. This difference was expected since in-silo scattering was not included in the DOT calculations done by RRA. The 10 group calculation agrees fairly well but slightly overestimates the measured result in the first few groups and is also deficient in describing the 70 keV characteristic skyshine peak. Both of these effects are apparently attributable to the energy bins being too wide to closely approximate the actual incident spectrum.

The agreement between the predicted and measured spectra is excellent in the 400 meter case. The 10 group result again slightly overestimates at high energies and also lacks sufficient detail in predicting the low energy peak. The Gaussian smoothed, 39 group, calculated result is almost indistinguishable from the measured spectra. The in-silo scattering effect should be negligible at this distance since the lower energy, silo-scattered photons are preferentially removed from the skyshine radiation at large source/detector distances.

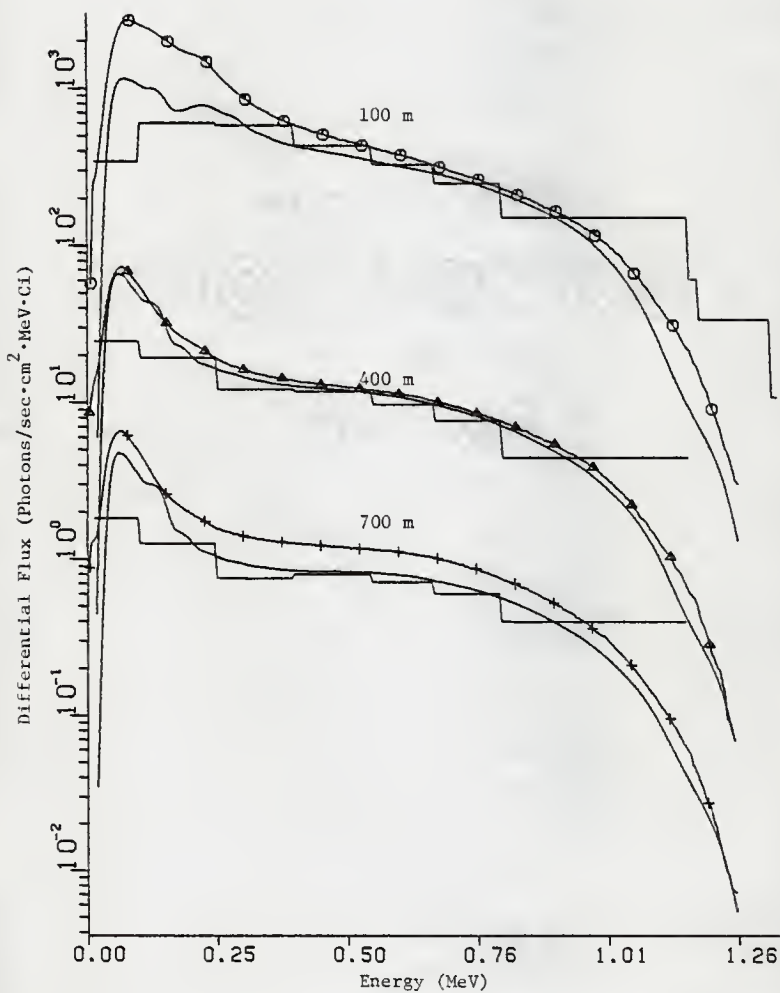


Fig. 29. Comparison of representative calculated and unfolded measured spectra for the unshielded source configuration.

The agreement in the 700 meter results is somewhat difficult to interpret since the source/detector distance at which the measurement was made is approximately 5% less than the distance used in the corresponding DOT calculation. Disregarding the differences in distances, the results appear to agree very well.

### 3.2.2 Comparison of Shielded Spectra

The shielded source configurations consisted of a Co-60 source covered first by 8" and then 16" of concrete. Only ten group, DOT calculations were performed for the shielded cases. Again an  $S_{12}$  angular grid and  $P_3$  cross section representation were used. To reduce further the computation time, the calculations were broken into several stages by RRA. First, the radiation penetrating the source shield was calculated with the one dimensional, discrete ordinates transport code, ANISN.<sup>22</sup> This shield penetration radiation was then used as a source for an air skyshine calculation using DOT.

The unfolded results for the 8" and 16" shielded source configurations are shown in Figs. 30 and 31, respectively. As with the unshielded results, each spectrum peaks at approximately 75 keV, but the middle energy range plateau is no longer present. Instead the unfolded spectra drop off in an almost perfect exponential fashion above the low energy peak resulting in somewhat softer spectra than in the unshielded case. Although the 100 meter spectra are still slightly distorted by the in-silo scattered component, this scattered source effect is considerably decreased by the silo roof shields compared to the unshielded skyshine results.

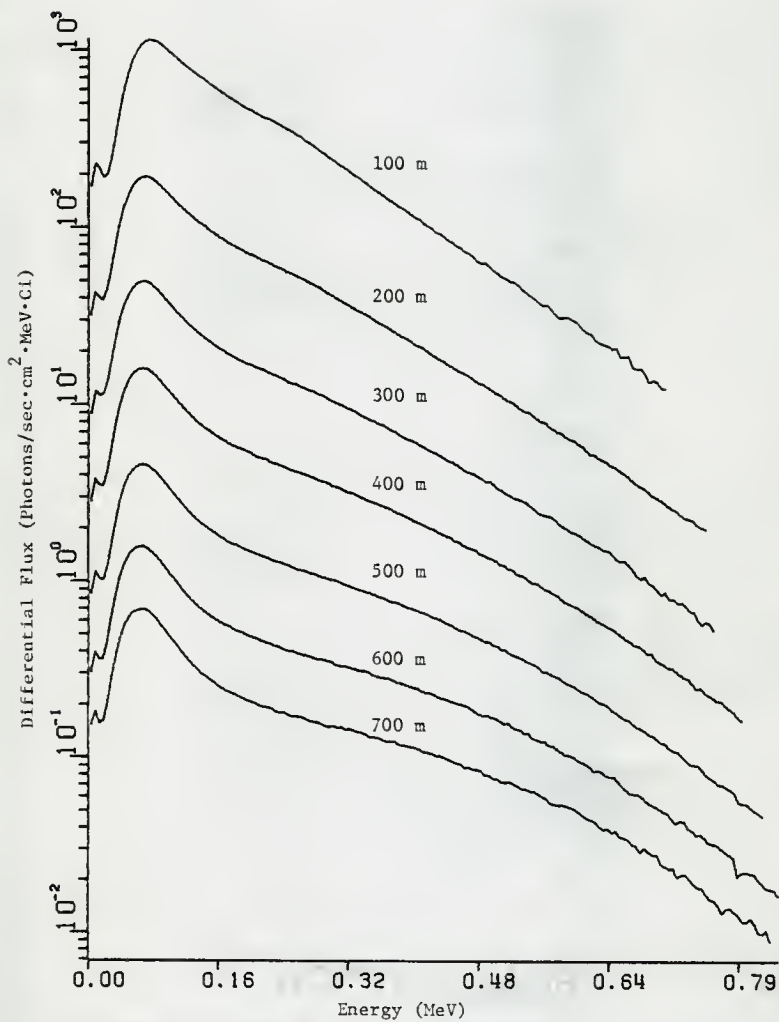


Fig. 30. Comparison of unfolded NaI spectra for the 3" shielded source configuration.

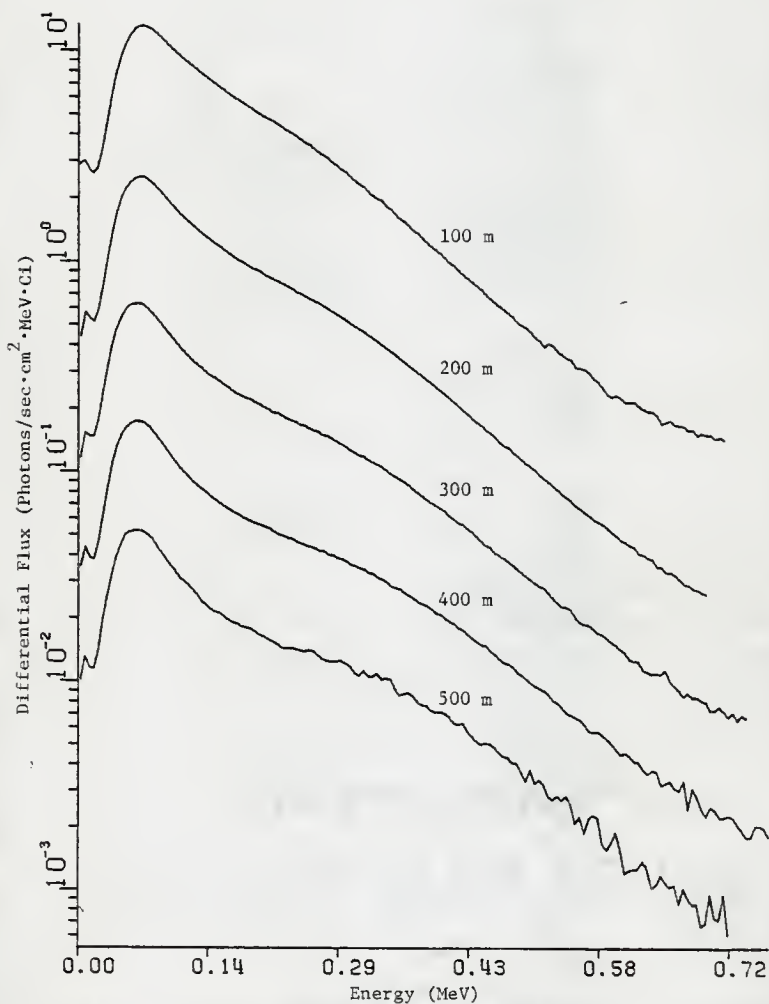


Fig. 31. Comparison of unfolded NaI spectra for the 16" shielded source configuration.

In Fig. 32 an unfolded skyshine spectrum measured at 100 meters with the 16" shielded source configuration is shown. The feature to note in this spectrum is the plateau occurring between 0.80 and 1.30 MeV, presumably caused by direct penetration of the silo wall by source photons. This effect was also studied by Ryufuku<sup>21</sup> to determine its contribution to the measured exposure rate. Again using the DOT-3 transport code, it was found that for source/detector distances less than five meters, the direct penetration component accounts for approximately 15% of the total exposure rate while at eighteen meters this contribution falls below 1%. These results for the wall-penetration component are shown in Fig. 33 along with some experimental results obtained with a high pressure ionization chamber (which is described in detail in Chapter 4). The large differences between these calculated and measured values probably arises because of the sensitivity of the calculated results to the assumed problem geometry which was an approximation of the actual source-silo configuration. The effect of this geometrical approximation would undoubtedly be most pronounced at small source/detector distances. Nevertheless, these results indicate that the silo wall penetration component is undoubtedly small compared to the skyshine component.

Representative spectra for the 8" shielded source configuration are shown in Fig. 34. Again it is seen that the 10 group calculations seriously underpredict the 70 keV peak in the measured spectra. The apparent close agreement for intermediate and high energies is somewhat misleading because of an error in the DOT modeling of the roof shield in the 8" shield configuration. The actual thickness of the shield in this



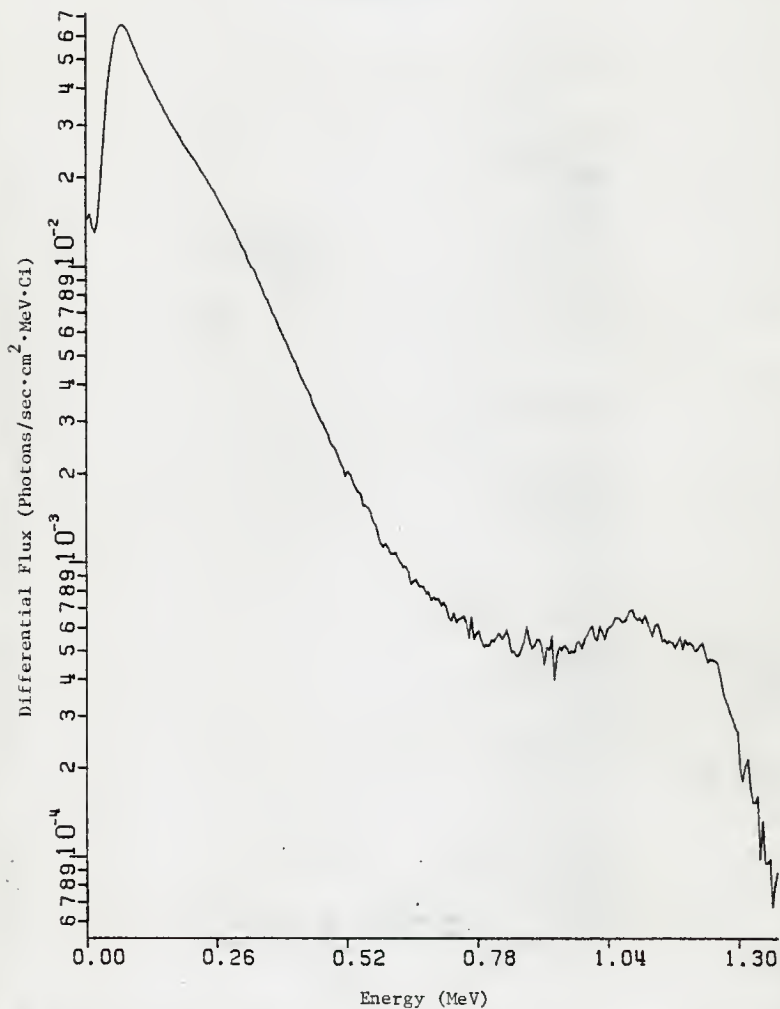


Fig. 32. Unfolded NaI spectrum showing direct penetration plateau for the 16" shielded source configuration. Source to detector distance is 100 meters.

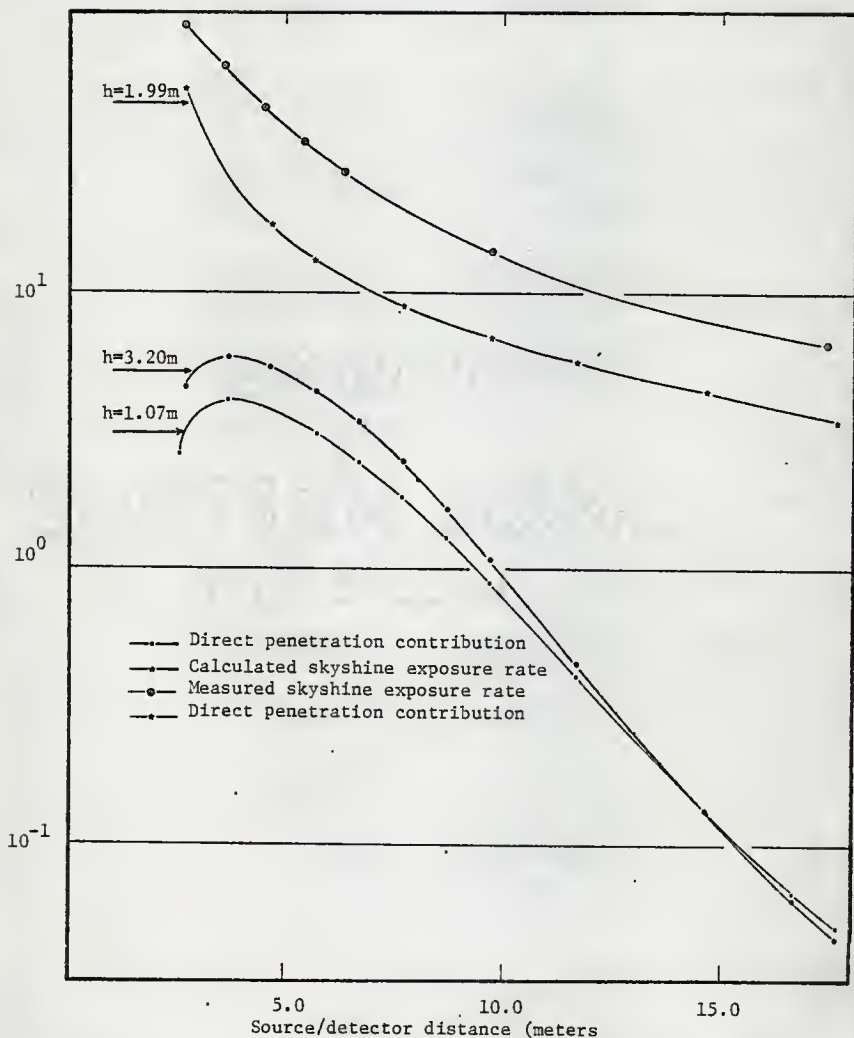


Fig. 33. Direct penetration exposure rate contribution for various detector heights,  $h$ , above grade.

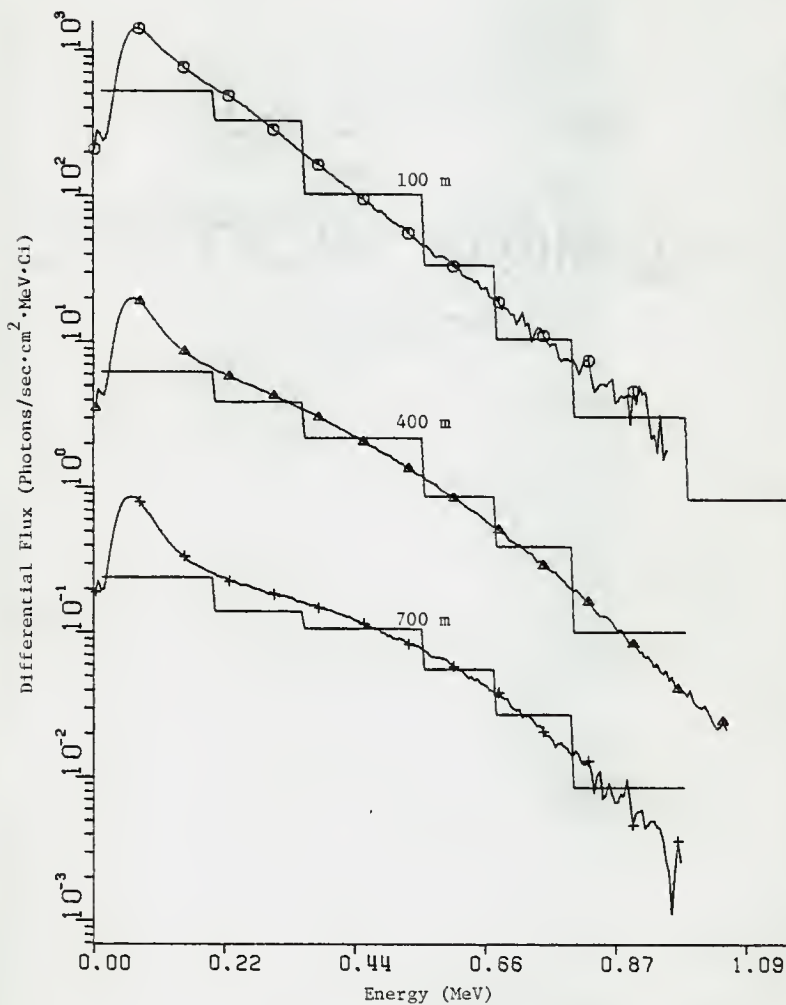


Fig. 34. Comparison of representative calculated and unfolded measured spectra for the 8'' shielded source configuration.

configuration was 21.03 cm whereas 20.03 cm was used in the DOT calculations. By performing a simple two-point exponential fit to the exposure rates, it was estimated that this error causes an overprediction of 10 to 20%. Other estimates place the error at 15%<sup>3</sup>.

Finally, Fig. 35 shows a comparison of representative 16" shielded results. As expected, the agreement is very good for all energy regions except below 100 keV.

It should be noted that for all source configurations, the shape of the DOT calculated spectra are extremely good, especially in the 39 group results. However, the normalization, or magnitude, of these spectra is inadequate for the 10 group calculated spectra. Additionally, negative flux values were obtained in the first few energy groups of the calculated results, which were suppressed to zero in this analysis.

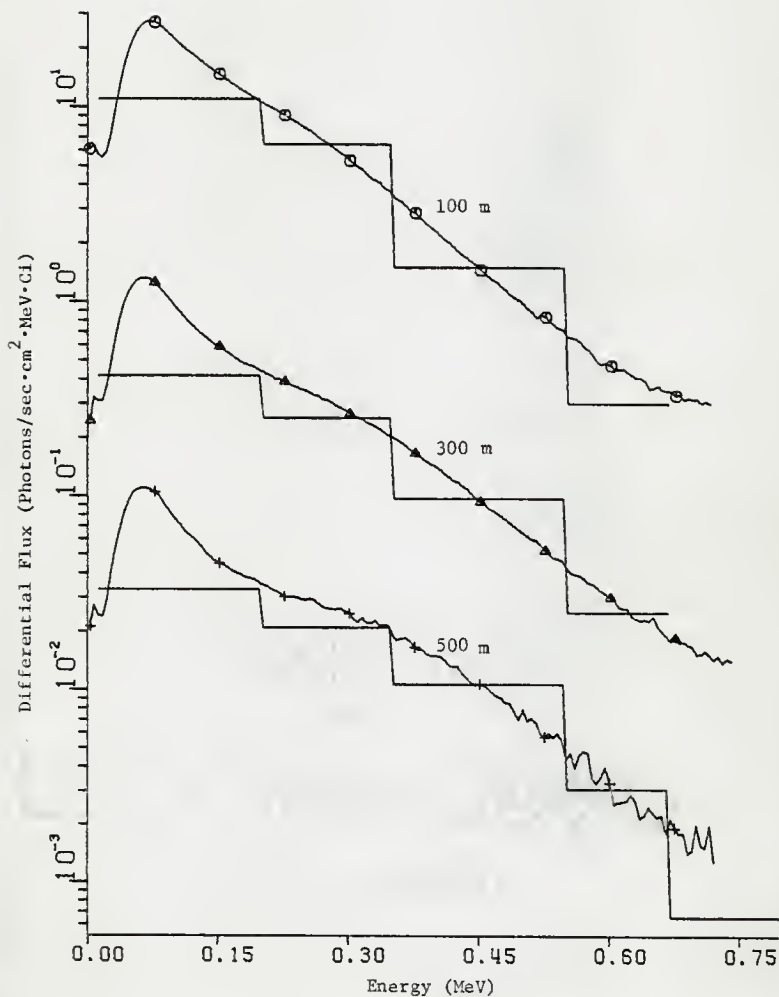


Fig. 35. Comparison of representative calculated and unfolded measured spectra for the 16'' shielded source configuration.

#### 4.0 Measurement and Comparison of Exposure Rates

In addition to the skyshine spectral measurements which served as a test of the various photon transport models, the second major objective of the skyshine experimental program was the measurement of the total skyshine exposure rate as a function of source/detector distance for both the shielded and unshielded source configurations. Such exposure rate measurements serve as additional benchmark data against which various calculational schemes for the prediction of the skyshine exposure rates can be compared. These measurements may also be used directly as design data for facilities in which skyshine radiation is of concern.

In this phase of the experiment, a high pressure ionization chamber (HPIC) was used to measure the  $4\pi$  skyshine exposure rate (i.e., omnidirectional exposure rate) over a 700 meter range of source-to-detector distances. The source configurations employed are the same as those used for the skyshine spectral measurements<sup>23</sup>. A 10 inch (25.4 cm) diameter, spherical, twenty-five atmosphere (2.5 MPa) argon-filled ionization chamber (Reuter-Stokes Area Monitor System, Model RS-111)<sup>24,25</sup> was used to measure the exposure rate resulting from the skyshine radiation field. Results and details of these measurements are given elsewhere<sup>3,23</sup>.

The exposure rate measured with the Reuter-Stokes detector must be corrected to obtain the true exposure rate because the system response is not linear with energy, especially below 300 keV. Although

the system response curve was supplied by the manufacturer, the incident energy spectrum is also required to calculate a correction factor which compensates for the non-ideal behavior of the system. Initial tests indicated that the ionization chamber was insensitive to the direction of the incident radiation and, therefore, only the energy dependence of the scalar flux is necessary for the calculation of this correction factor.

While the NaI spectral measurements provided some information about the energy spectrum of the incident radiation field, the NaI detector was collimated and hence the energy spectrum of only a portion of the total radiation field was obtained. Consequently, the original correction of the exposure rate data by RRA for non-ideal response of the HPIC<sup>3</sup> was based on the DOT-3.5 calculated  $4\pi$  energy spectra. In this chapter, the calculation of the spectrum correction factors for the HPIC results is re-examined and compared to a correction procedure which uses NaI spectral measurements. The NaI spectral measurements are also used to predict an exposure rate for the  $4\pi$  skyshine radiation field. These collapsed NaI measurements then serve as an independent determination of the total exposure rates against which the corrected Reuter-Stokes HPIC values may be compared.

#### 4.1 Correction of Observed Exposure Rates

##### 4.1.1 Theoretical Considerations

In general, the exposure,  $X$ , for a given photon fluence is

defined as<sup>26</sup>

$$X = \frac{\Delta Q}{m} \quad (4.1-1)$$

where  $\Delta Q$  is the sum of the electrical charges on all the ions of one sign produced in air when all the electrons (negatrons and positrons) liberated by photons in a volume element of air, whose mass is  $\Delta m$ , are completely stopped in air. The unit of exposure is the roentgen (R) which is equivalent to  $2.58 \times 10^{-4}$  Coulombs/kg. It follows that the exposure rate is simply the amount of exposure per unit time and may be calculated as

$$\dot{X} = \frac{E\phi e}{\bar{W}^{\text{air}}} (\mu_{\text{en}}/\rho)^{\text{air}}, \quad (4.1-2)$$

where  $E$  is the energy of the incident photons,  $\phi$  is the photon flux,  $e$  is the electron charge ( $1.6 \times 10^{-19}$  C),  $\bar{W}^{\text{air}}$  is the average amount of energy required to create one ion-electron pair (equal to approximately 34 eV over the photon energy range of interest), and  $(\mu_{\text{en}}/\rho)^{\text{air}}$  is the mass energy absorption coefficient for air. The use of this particular coefficient implies the loss of all secondary photons, e.g., bremsstrahlung. The substitution of numerical values into Eq. (4.1-2) yields

$$\dot{X} = 65.664 E \phi (\mu_{\text{en}}/\rho)^{\text{air}}, \quad (4.1-3)$$

where  $\dot{X}$  is in  $\mu\text{R}/\text{h}$ ,  $E$  in MeV,  $\phi$  in  $\text{cm}^{-2} \text{sec}^{-1}$  and  $(\mu_{\text{en}}/\rho)^{\text{air}}$  in  $\text{cm}^2 \text{g}^{-1}$ . When the incident spectrum is represented by discrete components (e.g., a pulse height spectrum), Eq. (4.1-3) can be formulated as



$$\dot{X} = 65.664 \sum_{i=1}^{NC} E_i \phi_i (\mu_{en}/\rho)_i^{air} \quad , \quad (4.1-4)$$

where NC represents the number of components in the spectrum,  $E_i$  and  $(\mu_{en}/\rho)_i^{air}$  are appropriately averaged values for the  $i$ -th energy interval in the spectrum, and  $\phi_i$  is the energy-integrated flux over the  $i$ -th interval.

In an ionization chamber such as the one used in the skysshine experiment, the exposure rate is inferred from the current produced by the radiation-ionized filling gas. In the ideal case, the response of the detector would be directly related to the radiation intensity by some conversion constant, regardless of the energy of the ionizing radiation. In practice, the response of the system is not ideal because the steel sphere filled with pressurized argon does not respond as would a detector composed totally of air, i.e., it is not "air equivalent". Therefore, in general, an energy dependence correction factor must be derived to correct the observed exposure rate readings.

The current collected from the ionized filling gas  $I(E)$ , in amperes, due to an incident radiation field,  $\phi(E)$ , is given by

$$I(E) = K(E) \cdot X(E) \quad , \quad (4.1-5)$$

where  $X(E)$  is the exposure rate as a function of photon energy in  $\mu R/h$  and  $K(E)$  is a conversion constant which can be expressed as

$$K(E) = CF(E) \quad . \quad (4.1-6)$$

In the above equation,  $C$  is a proportionality constant determined at some specific reference energy and  $F(E)$  is the response of the argon-filled sphere with energy compared to the reference. The measured

energy sensitivity of the system,  $F(E)$ , is shown in Fig. 36, for the chamber size and filling pressure used in this experiment.

From Eq. (4.1-5), the total current collected,  $I_Y$ , due to an incident polyenergetic radiation field is

$$I_Y = \int_0^{E_{\max}} dE I(E) = \int_0^{E_{\max}} dE K(E) \dot{X}(E) \quad , \quad (4.1-7)$$

where  $E_{\max}$  is the maximum photon energy in the spectrum. After substitution of Eq. (4.1-6),  $I_Y$  can be written as

$$I_Y = C \int_0^{E_{\max}} dE F(E) \dot{X}(E) \quad . \quad (4.1-7)$$

To obtain an expression for  $\dot{X}(E)$ , Eq. (4.1-3) may be expressed in terms of continuous functions as

$$\dot{X}(E) = 65.664 \{E\phi(E)(\mu_{\text{en}}(E)/\rho)\} \quad , \quad (4.1-8)$$

and upon substitution in Eq. (4.1-7),  $I_Y$  becomes

$$I_Y = 65.664C \int_0^{E_{\max}} dE F(E)E\phi(E)(\mu_{\text{en}}(E)/\rho) \quad . \quad (4.1-9)$$

For convenience, an average system sensitivity,  $\bar{F}$ , may be defined as

$$\bar{F} = \frac{\int_0^{E_{\max}} dE F(E)E\phi(E)(\mu_{\text{en}}(E)/\rho)}{\int_0^{E_{\max}} dE E\phi(E)(\mu_{\text{en}}(E)/\rho)} \quad (4.1-10)$$

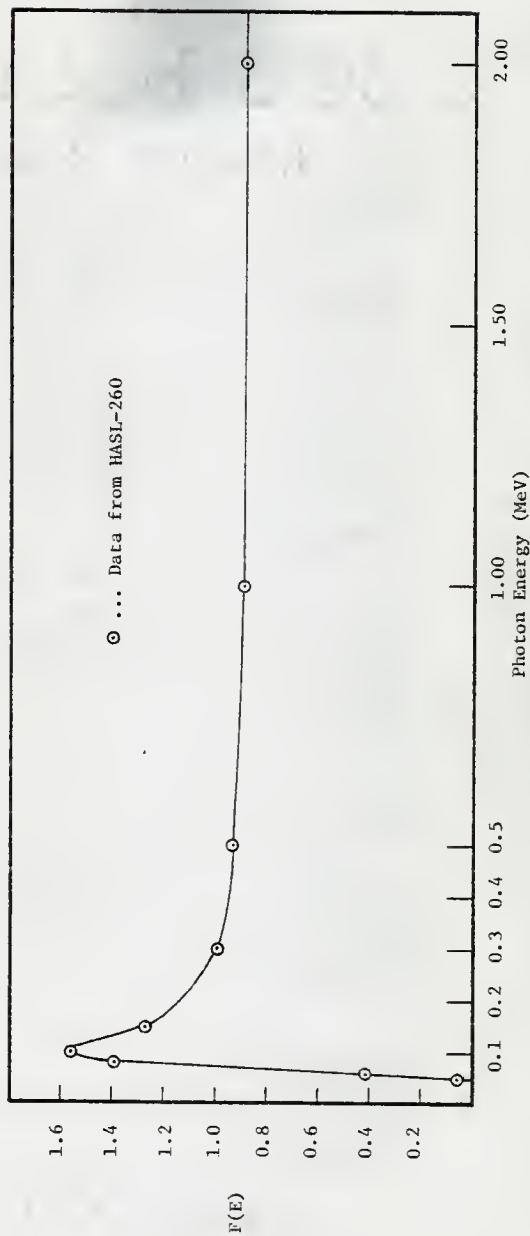


Fig. 36. Energy Sensitivity of the Reuter-Stokes High Pressure Ionization Chamber

which can be physically interpreted as the ratio of the observed exposure rate with a non-ideal system sensitivity to the exposure rate obtained with an ideal system sensitivity. With this definition, Eq. (4.1-9) becomes

$$I_Y = \overline{CFX} \quad , \quad (4.1-11)$$

where

$$\dot{X} = \int_0^E dE E \phi(E) (\mu_{en}(E)/\rho) \quad . \quad (4.1-12)$$

Since the argon-filled sphere is surrounded by a cubical aluminum protective housing which was not present in the original determination of  $F(E)$ , an additional minor correction needs to be made to account for the attenuation of the incident radiation by this housing. Therefore, Eq. (4.1-10) is modified to

$$\overline{F} = \frac{\sum_{i=1}^{NC} F_i E_i \phi_i (\mu_{en}/\rho)_i^{air} e^{-(\mu_a)_i \Delta l}}{\sum_{i=1}^{NC} E_i \phi_i (\mu_{en}/\rho)_i^{air}} \quad , \quad (4.1-13)$$

where  $\overline{F}$  has been expressed in terms of a discrete energy representation and  $t$  is the wall thickness of the aluminum shell.

An expression for the exposure rate,  $\dot{X}$ , can now be obtained from Eq. (4.1-11) as

$$\dot{X} = \frac{I_Y}{\overline{CF}} \quad . \quad (4.1-14)$$

For a specific reference or calibration energy, denoted by  $c$ , Eq. (4.1-6) becomes

$$K_c = CF_c e^{(\mu_a)_c^{Al} \cdot t} \quad (4.1-15)$$

where the effect of the attenuation by the aluminum housing has been included. Thus

$$C = \frac{K_c e^{-(\mu_a)_c^{Al} \cdot t}}{F_c} \quad (4.1-16)$$

Substitution of Eq. (4.1-16) into Eq. (4.1-14) then yields

$$X = \frac{I_\gamma F_c e^{(\mu_a)_c^{Al} \cdot t}}{K_c \bar{F}} \quad (4.1-17)$$

Furthermore, it should be noted that the current measured by the ion chamber is the sum of two components. The first,  $I_\gamma$ , is due to the ionization of the argon filling gas by the incident radiation field. The second,  $I_b$ , is a result of inherent system noise and background radiation. Thus

$$I_\gamma = I_t - I_b \quad (4.1-18)$$

where  $I_t$  is the total current collected. Substitution of this expression into Eq. (4.1-17) yields

$$X = \frac{(I_t - I_b) F_c e^{(\mu_a)_c^{Al} \cdot t}}{K_c \bar{F}} \quad (4.1-19)$$

From this result, it is observed that the true exposure rate as given by Eq. (4.1-19) is composed of two parts, the first being the observed or measured exposure rate,

$$\dot{X}_{\text{meas.}} = \frac{I_t - I_b}{K_c}, \quad (4.1-20)$$

and the second being a correction factor to account for the non-ideal response of the system with energy. Equivalently,

$$\dot{X} = \bar{f} \frac{(I_t - I_b)}{K_c} \quad (4.1-21)$$

where  $\bar{f}$  is a "system energy correction factor" defined as

$$\bar{f} = \frac{F_c e^{(\mu_a)_c^{A\lambda} \cdot t}}{\bar{F}} \quad (4.1-22)$$

This correction factor,  $\bar{f}$ , is thus used to correct the HPIC reading to yield the true exposure rate. Notice that to obtain a value for  $\bar{f}$  (or  $\bar{F}$ ), both the system energy sensitivity,  $F(E)$ , and the incident energy spectra,  $\phi(E)$ , must be known. The effect of this non-ideal behavior on the exposure rate is shown in Figs. 37-39 for the unshielded, 8" shielded and 16" shielded skyshine source configurations, respectively. The quantities shown on these graphs are the exposure rate contributions for measured NaI energy-dependent fluxes (unfolded) as computed for both the ideal (i.e.,  $F(E)=1$ ) and the non-ideal system energy sensitivities. The non-ideal, or Reuter-Stokes HPIC exposure rate contribution from the flux in energy interval  $i$  is defined as

$$\dot{X}_{\text{contr}, i+\frac{1}{2}}^{\text{NI}} = 65.66 \left\{ F_{i+\frac{1}{2}} E_{i+\frac{1}{2}} \phi_{i+\frac{1}{2}} (\mu_{\text{en}}/\rho)_{i+\frac{1}{2}} \right\} \quad (4.1-23)$$

while the ideal exposure rate contribution is calculated with  $F_{i+\frac{1}{2}}=1$  for all  $i$ . The subscript " $i+\frac{1}{2}$ " denotes the value of the function

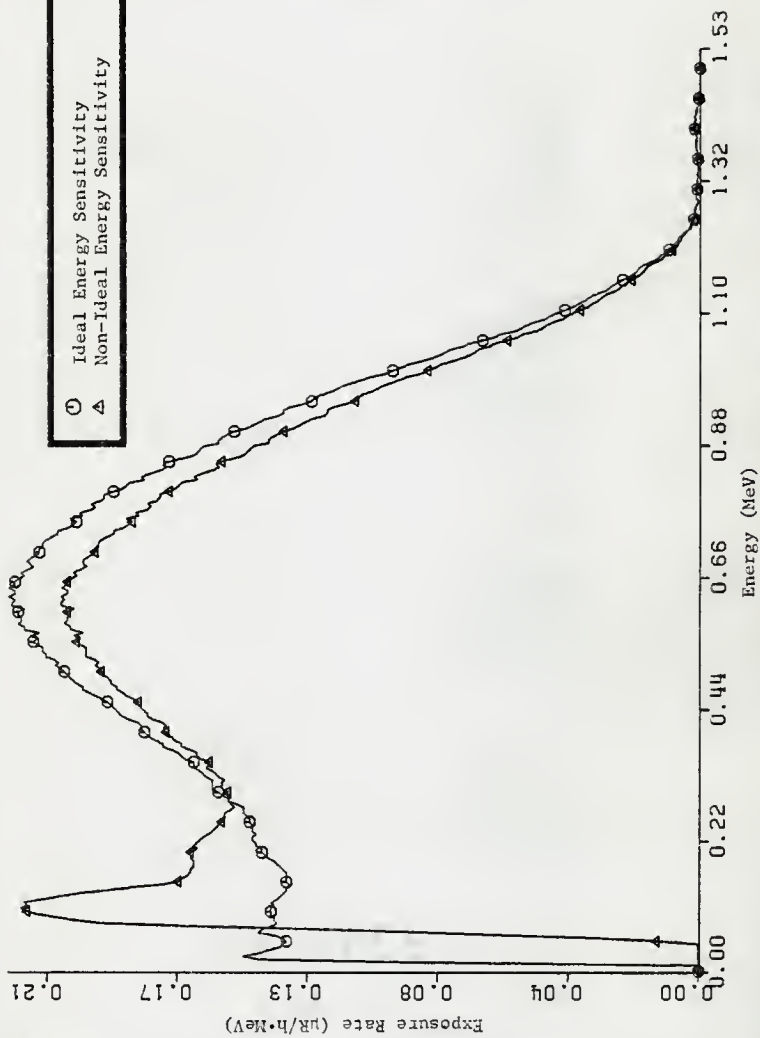


Fig. 37. Effect of non-ideal energy sensitivity on the distribution of exposure rate contribution for the unshielded source configuration at 400 m.

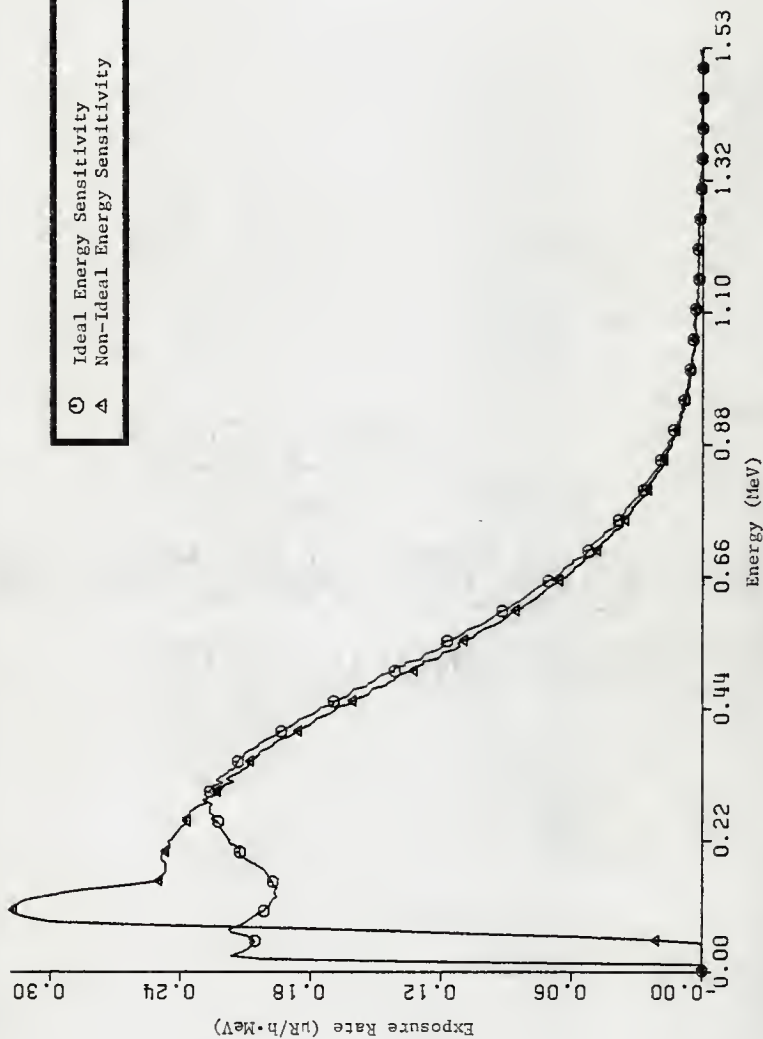


Fig. 38. Effect of non-ideal energy sensitivity on the distribution of exposure rate contribution for the 8" shielded source configuration at 400 m.



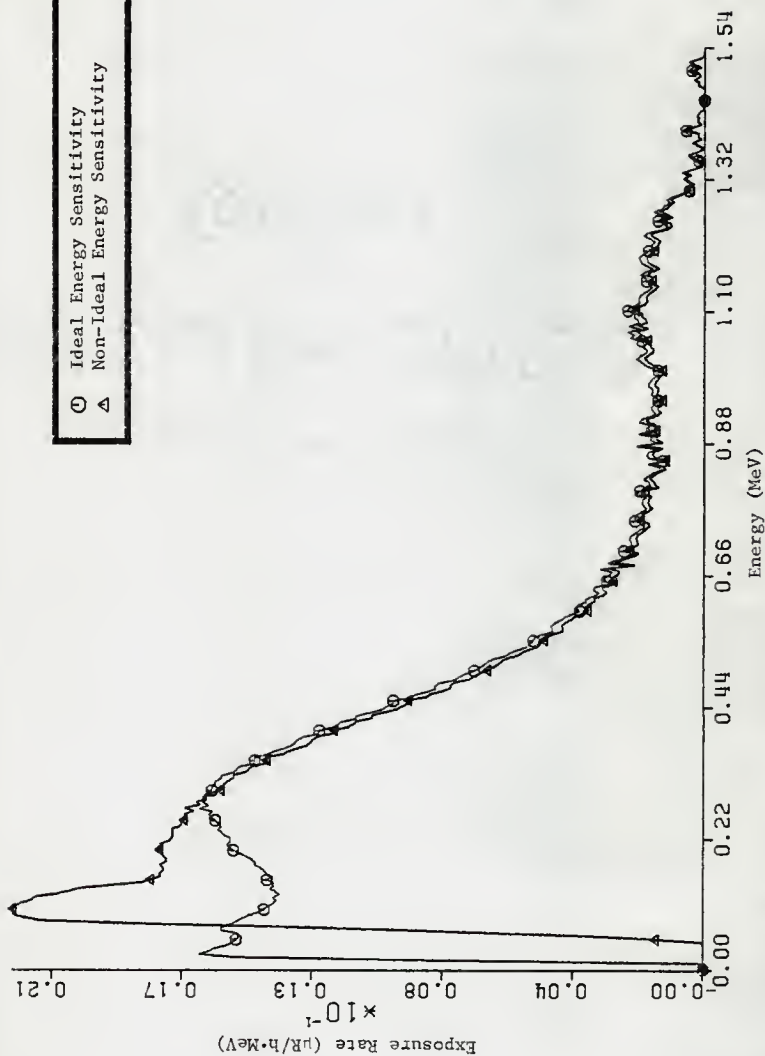


Fig. 39. Effect of non-ideal energy sensitivity on the distribution of exposure rate contribution for the 16" shielded source configuration at 400 m.

evaluated at the center of the energy interval which for these figures had a width of 5 keV. In these figures, the area under the ideal contribution curve is equal to the true exposure rate as would be calculated from the unfolded NaI spectrum, while the area under the non-ideal response curve is equal to the exposure rate which would have been measured by the Reuter-Stokes HPIC detector, if it had experienced the same degree of collimation as did the NaI detector.

Because of the peaked nature of  $F(E)$  at approximately 100 keV, the Reuter-Stokes detector overemphasizes the low energy contribution to the exposure rate. As opposed to this, the middle and high energy contributions are underestimated because the value of  $F(E)$  is less than unity in these regions (.88 at 1.25 MeV). The extreme low energy contributions ( $E < 50$  keV) is completely lost to the Reuter-Stokes chamber because of the cutoff in the sensitivity at this energy. Since, as discussed in Chapter 3, the skyshine spectra peaked at approximately 70 keV, the ionization chamber may miss a significant portion of the incident spectrum. However, this cutoff in the detector sensitivity did not turn out to be serious since, as can be seen in Figs. 37-39, the maximum contribution to the exposure rate comes at 600 and 300 keV for the unshielded and shielded skyshine source configurations, respectively.

#### 4.1.2 Calculation of the Correction Factor $\bar{f}$

Two problems are encountered in the calculation of the HPIC correction factor  $\bar{f}$ . The first problem is that the true incident spectrum,  $\phi(E)$ , or  $\phi_1$ , is generally not known. Secondly, large errors may be incurred

by the representation of the rapidly varying continuous quantities in Eq. (4.1-7) by the discrete or energy-group averaged values in Eq. (4.1-13).

The simplest method of obtaining group values for the discrete representation is to evaluate the continuous function at the midpoint of the energy bin and thereafter assume that it is constant for that particular energy range. Such a simple discretization procedure may be acceptable if the energy mesh or bin width is sufficiently fine. A more sophisticated and accurate way of treating this problem is to use spectral weighting to average a particular parameter across each energy bin. For example, given some energy dependent quantity  $\beta(E)$ , the group averaged value is given by

$$\beta_g = \frac{\int_{E_g}^{E_g + \Delta E_g} dE \beta(E) \phi(E)}{\int_{E_g}^{E_g + \Delta E_g} dE \phi(E)} \quad (4.1-24)$$

where  $E_g$  in the present application corresponds to the lower edge of some energy bin "g" and  $\Delta E_g$  is the width of that bin.

Just as in Eq. (4.1-10), Eq. (4.1-24) involves the incident spectrum,  $\phi(E)$ , which is generally unknown and therefore an approximate representation must often be used. The philosophy of spectral weighting involves the use of a "hyper-fine" discrete representation of  $\phi(E)$  to calculate group constants to be used with coarse energy group representations of the incident spectrum. The bin widths in the hyper-fine

representation need to be sufficiently small so that the variation of  $\beta(E)$  can be considered negligible across any one bin and therefore mid-point values can be used.

Two hyper-fine mesh approximations to  $\phi(E)$  were available in this analysis, the first being the Gaussian smoothed 39 group DOT results and the second being the unfolded NaI spectra. The Gaussian smoothed calculated spectra represented the best estimates available of the incident flux for the unshielded source configuration. As discussed in Chapter 3, the 39 group spectra agreed extremely well with the unfolded NaI results and thus one assumes that the prediction of the  $4\pi$  geometry incident flux would be equally good although experimental data were not available for a direct comparison.

However, unfolded NaI spectra represented the only hyper-fine mesh estimate of the incident flux for the shielded source configurations, since only coarse mesh, 10 group DOT calculations were performed for these cases. Because the  $4\pi$  energy spectra were expected to be "softer" than the collimated geometry spectra (an observation from the 39 group DOT results), some error may be incurred by approximating the  $4\pi$  incident flux by a collimated result.

The calculation of  $\bar{f}$  for the unshielded source configuration provided an excellent opportunity to determine the sensitivity of the group constants to the assumed spectral shape used for weighting since the values obtained using the collimated NaI spectra as weighting functions could be compared to those obtained using the Gaussian smoothed 39 group

results as the weighting spectra. The unshielded calculations also provided an excellent determination of the sensitivity of the result to the coarse group approximation of  $\phi(E)$  used in Eq. (4.1-13). With the 39 group results as a benchmark, the results obtained with the 10 group approximation could thus be examined. It was imperative that the sensitivity of the calculated  $\bar{F}$ 's to these parameters be determined with the calculated unshielded spectra because the 39 group calculations, which serve as the best estimate of the  $4\pi$  spectrum, were not performed for the shielded source configurations.

The procedure followed in the determination of the group constants required for the calculation of  $\bar{F}$  was to develop discrete hyper-fine mesh representations of  $F$ ,  $(\mu_{en}/\rho)^{air}$ ,  $(\mu_a/\rho)^{Al}$ , and  $\phi$ . The representations of  $\phi$  have already been discussed. It was assumed that the bin width of the hyper-fine mesh structure was sufficiently narrow so that negligible error was incurred by approximating continuous functions by their value at the centroid of each bin, i.e.,

$$\frac{\int_{E_g}^{E_g + \Delta E_g} dE \beta(E) \phi(E)}{\int_{E_g}^{E_g + \Delta E_g} dE \phi(E)} = \beta(E_g + \Delta E_g / 2) \quad , \quad (4.1-25)$$

for sufficiently small  $\Delta E_g$ .

The data used in the construction of the hyper-fine mesh representation of the photon coefficients were taken from Reference 20. A two-point exponential fit was used successively between these data

points to obtain values at 5 keV intervals corresponding to the mid-points of the energy bins in the hyper-fine structure.

The discrete representation of  $F(E)$  was accomplished through the use of data from Reference 25 which are tabulated in Table 6. As described above, a two-point exponential fit was used successively between the data points in the energy regions from 50 to 80 keV and from 0.15 to 2.0 MeV. A three-point quadratic fit was used between 80 and 150 keV to approximate the peaked portion of  $F(E)$ . The value of  $F_c$  and  $(\mu_a)_c^{Al}$  were taken at the average Co-60 emission energy of 1.25 MeV.

Table 6. Data Used in Construction of  $F(E)$ <sup>25</sup>

Energy (keV)	$F(E)$
50	0.064
60	0.408
80	1.390
100	1.562
150	1.270
300	0.982
500	0.940
1000	0.886
2000	0.886

Since the data in this analysis consisted of discrete components, Eq. (4.1-24) must be written as

$$\beta_g = \frac{\sum_{i=1}^{NB} \beta_i \phi_i}{\sum_{i=1}^{NB} \phi_i} \quad (4.1-26)$$

before performing the spectral weighting. In Eq. (4.1-26), NB stands for the number of hyper-fine bins in energy group g. As can be seen from Eq. (4.1-13), two sets of group constants are necessary for the calculation of  $\bar{F}$ . With reference to Eq. (4.1-26), the first set of group constants corresponds to

$$\beta_i = F_i E_i (u_{en}/\rho)_i e^{-(u_a)_{i1}^{A\lambda} \cdot t}, \quad (4.1-27)$$

while the second set corresponds to

$$\beta_i = E_i (u_{en}/\rho)_i. \quad (4.1-28)$$

Selected results of this sensitivity study for the unshielded skyshine case are presented in Table 7. The quantities tabulated are the  $\bar{F}$  correction factor calculated from Eq. (4.1-18) as a function of source/detector distance and weighting spectrum. Results are also shown comparing the values obtained when the 10 group approximation to  $\phi(E)$  is used in Eq. (4.1-8) instead of the fine mesh 39 group spectra. The second subscript on  $\bar{F}$  refers to the weighting spectrum used while the superscript and the first subscript refer to the approximation to  $\phi(E)$  used in Eq. (4.1-8). For example,  $\bar{F}_{10,100mGS}^{4\pi}$  signifies an  $\bar{F}$  calculated using a  $4\pi$  geometry, 10 group DOT calculated approximation to  $\phi(E)$  with group constants computed from a 100 meter Gaussian smoothed weighting spectrum.

Table 7. Results of Preliminary  $\bar{f}$  Calculations

Radial Distance (m)	$\bar{f}_{39,100\text{mGS}}^{-4\pi}$	$\bar{f}_{10,100\text{mGS}}^{-4\pi}$	$\bar{f}_{39,700\text{mGS}}^{-4\pi}$	$\bar{f}_{10,700\text{mGS}}^{-4\pi}$
100	.8814	.9135	.8819	.9202
200	.8917	.9079	.8925	.9168
300	.9017	.9034	.9026	.9152
400	.9083	.9119	.9092	.9244
500	.9124	.9146	.9133	.9277
600	.9152	.9143	.9162	.9258
700	.9170	.9179	.9179	.9306
Weighting Spectrum used	100 mGS 4 $\pi$	100 mGS 4 $\pi$	700 mGS 4 $\pi$	700 mGS 4 $\pi$
	100 mGS coll.	100 mGS coll.	700 mGS coll.	700 mGS coll.



As can be seen from the results, the variations in the  $\bar{F}$  values are negligible regardless of whether a  $4\pi$  or collimated geometry weighting spectrum is used. This is somewhat surprising since the shapes of the two spectra are significantly different. It is also observed that the value of  $\bar{F}$  changes only slightly when a 10 group spectrum, with properly average group constants, is used in Eq. (4.1-8) instead of the 39 group approximation. The  $\bar{F}$  values shown in Table 8 are taken from Reference 3 for the unshielded source configuration. The differences between the values produced in this work and those shown in Table 8 are less than 5%. The calculational steps used in obtaining the values in Table 8 are not described in Reference 3 and therefore, it is not known why these apparent differences arise. There is certainly room for error in the construction of  $F(E)$  due to the sparseness of data supplied in Reference 25.

The close agreement of the results contained in Table 1 suggests that for the analysis of skyshine data one may use collimated unfolded NaI spectra in the calculation of group constants when a  $4\pi$  weighting spectrum is unavailable. Since 39 group calculations were done only for the unshielded source configuration, unfolded NaI spectra must be used as weighting spectra in the calculation of the group constants for the shielded source configurations. Additionally, the relatively good agreement between the 10 and 39 group calculated  $\bar{F}$ 's for the unshielded case gives one a certain amount of confidence in the results obtained with the same technique for the shielded source configurations.

Table 8. Published Values of the Energy Dependence Correction Factor for the Unshielded Source Configuration<sup>3</sup>

Radial Distance (m)	$\bar{F}$
50	.885
100	.905
200	.901
300	.895
400	.890
500	.887
600	.883
700	.883

#### 4.1.3 Correction Factor Values for the Unshielded Source Configuration

To correct the HPIC measurements for the non-ideal energy response of the system,  $\bar{f}$  values were calculated at 100 meter intervals along the 700 meter measurement baseline. The weighting spectra used were the Gaussian smoothed, 39 group,  $4\pi$  geometry DOT results. The results of these calculations are given in Table 9 where they are also compared to those given in Reference 3. From these results it is observed that the  $\bar{f}$  values obtained in this work increase slightly with increasing source/detector distance. There are two competing processes which contribute to this trend which can be seen in Fig. 37. The peak portion (70-200 keV) of the non-ideal energy sensitivity curve tends to force  $\bar{f}$  below unity since the exposure rate as seen by the HPIC is larger than reality. However, the opposite effect occurs above approximately 250 keV where the true exposure rate is underestimated by the HPIC thus tending to make  $\bar{f}$  greater than unity.

Both of these processes are significant in the unshielded source configuration results. As can be observed in Fig. 26, the number of photons in the region immediately above the 75 keV maximum decreases with increasing source/detector distance thus tending to make  $\bar{f}$  closer to unity. The ratio of the number of photons at 75 keV to the number of photons at 750 keV is increasing with source/detector distance which tends to make  $\bar{f}$  less than unity. The former effect dominates in these bare skyshine spectra which explains the observed upward trend in the  $\bar{f}$  values (although the latter effect tends to dampen this variation). It is interesting to note that

the RRA calculated values exhibit the opposite behavior, a trend which seems to have little physical justification.

Table 9. Comparison of Unshielded  $\bar{F}$  Values

Radial Distance (meters)	This Work	RRA <sup>3</sup>
100	.881	.905
200	.892	.901
300	.902	.895
400	.909	.890
500	.913	.887
600	.916	.883
700	.918	.883

#### 4.1.4 Correction Factor Values for the Shielded Source Configurations

Unfolded NaI spectra were used as the weighting spectra in calculating the  $\bar{F}$ 's for the shielded source configurations. As in the unshielded case, these values were calculated at 100 meter intervals along the 700 meter measurement baseline. The results of these calculations for the 8" shielded source configuration are shown in Table 10 as well as the corresponding results presented in Reference 3. As is obvious from Table 10, the values obtained by RRA are constant which indicates a constant spectral shape. However, the results obtained from this work range from .85 at 100 meters to .96 at 700 meters which indicates a significant change in the spectral shape with distance as is observed in Fig. 30.

Table 10. Comparison of  $\bar{f}$  Values for the 8" Shielded Source Configuration

Radial Distance (meters)	This Work	RRA <sup>3</sup>
100	.845	.89
200	.884	.89
300	.914	.89
400	.912	.89
500	.922	.89
600	.936	.89
700	.958	.89

Finally, Table 11 compares the  $\bar{f}$  values obtained for the 16" shielded source configuration. The larger variation of the  $\bar{f}$  values for the shielded source configurations is easily understood from Figs. 38 and 39. Since the shielded source configuration spectra fall off almost exponentially, the middle and high energy portions of the spectra contribute very little to the total exposure rate thus practically eliminating the mitigating effect on the upward trend of the  $\bar{f}$  values which was discussed in the previous section.

Table 11. Comparison of  $\bar{f}$  Values for the 16" Shielded Source Configuration

Radial Distance (meters)	This Work	RRA <sup>3</sup>
100	.855	.885
200	.883	.885
300	.908	.885
400	.912	.885
500	.918	-

Again, the values obtained by RRA are constant with source/detector distance while the values obtained in this work range from 0.86 to 0.92 over the 500 meter measurement baseline. Considering the slight changes in the spectral shape observed in Fig. 31, the upward trend of the results obtained here seem well-justified. As was seen in Figs. 30 and 31, the number of photons lying immediately above the 75 keV maximum decreases with increasing source/detector distance. Consequently, the amount by which the HPIC overestimates the total exposure rate decreases, thereby causing  $\bar{f}$  to approach unity.

#### 4.2 Comparison of Measured and Calculated Exposure Rate Values

The exposure rates for the collimated detector geometry were calculated from the unfolded NaI spectra using Eq. (4.1-4). These values were then reduced by 2% to take into account the non-ideal collimator effectiveness described in Chapter 2. The value of this correction for the non-ideal behavior of the detector collimator was estimated by comparing the area under the actual collimator traverse curve (Fig. 11) to that expected in the ideal case<sup>3</sup>.

Exposure rates were calculated from the DOT 3.5 fluxes tabulated in Reference 3, again using Eq. (4.1-4). Exposure rate values obtained from these calculated spectra are also given in Reference 3 for  $4\pi$  geometry. In general, the values presented in this work are approximately 3% lower than those calculated by RRA<sup>3</sup>, the only exception being the 16" shield configuration results which were in

much closer agreement. These minor discrepancies are probably due to differences in the material constants (e.g.,  $\mu/\rho$ , etc.) used.

A small error was made for the 8" shielded source configuration in the DOT 3.5 transport calculations<sup>3</sup>. Instead of the proper concrete source shield thickness of 21.03 cm (8.28"), 20.03 cm (7.89") was used. In an attempt to correct for this oversight, a two-point exponential fit was done between the 42.83 cm (16.86") and the 20.03 cm exposure rate results and used to interpolate a value for a 21.03 cm shield. For those source-detector distances where the 42.83 cm results were not available, the unshielded configuration results were used. This correction resulted in an approximately 15% reduction of the 20.03 cm values when the interpolation was made between the two shielded data points. When the unshielded and 20.03 cm data points were used, the reduction was approximately 20%. Those values obtained using the shielded data points are expected to be more accurate since the source configurations are more closely related.

#### 4.2.1 Comparison of Collimated Detector Results

A comparison of the exposure rates for a collimated detector are shown in Fig. 40 for the seven source/detector distances used in this experiment. The solid line shows the trend of the 10 group results while the dotted line follows the 39 group predictions. The quantity plotted on the ordinate is the exposure rate multiplied by the square of the source/detector distance, normalized to a unit source

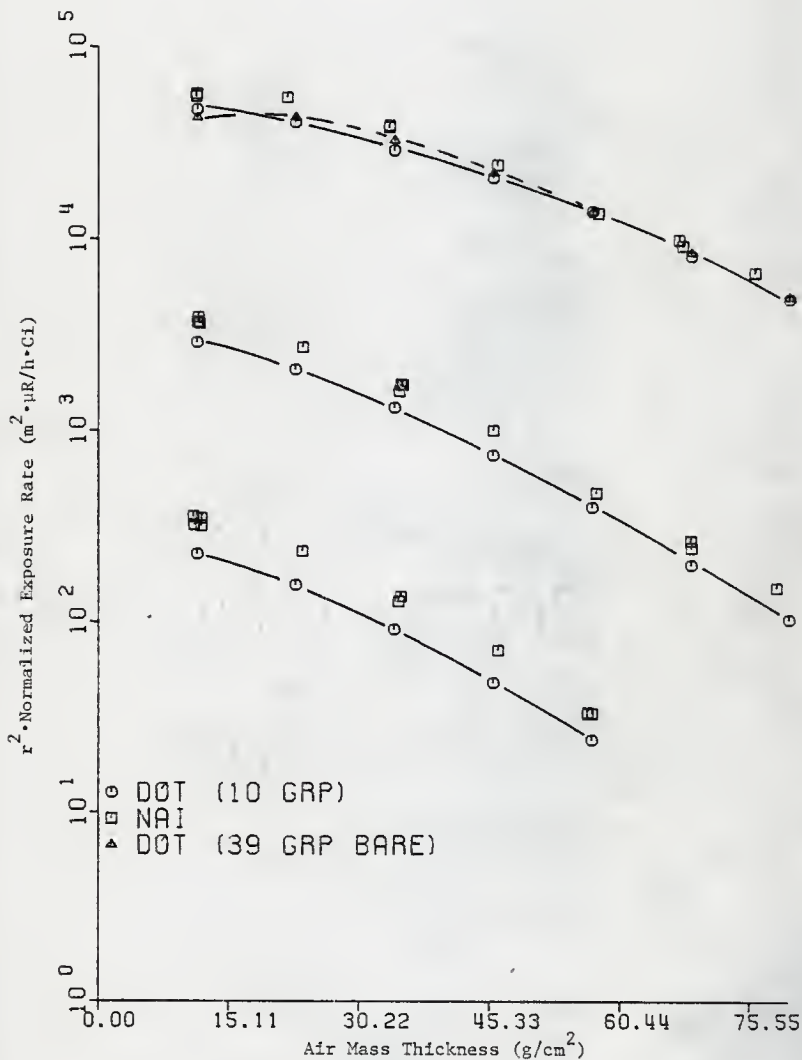


Fig. 40. Comparison of measured and calculated exposure rates for the collimated detector geometry.



strength. Multiplication of the exposure rate by  $r^2$  removes the effect of the geometric attenuation factor (i.e.,  $1/r^2$ ) and thus the plot of the results is a fairly slowly varying function.

Since the air density was not constant for each measurement, a more accurate indication of the distance from the source in terms of mass attenuation is the air density,  $\rho$ , times the source/detector distance, referred to as the air mass thickness. The density of the moist air,  $\rho$  in g/l, with relative humidity,  $R$ , in percent and at temperature,  $T$ , in °K was calculated as<sup>3</sup>

$$\rho_{\text{air}} = \frac{1.2929 (273.13)}{2} \left\{ \frac{P}{1013} - \frac{0.3783e_s}{1013} \cdot \left( \frac{R}{100} \right) \right\} \quad (4.2-1)$$

where  $P$  is the atmospheric pressure in millibars and  $e_s$  is the saturation vapor pressure of water at temperature  $T$ <sup>27</sup>.

As can be seen, the 10 group results underpredict the collimated geometry exposure rate by approximately 15 to 20% for the unshielded and 8" shielded source configurations. The errors in the 16" shield configuration results are closer to 30%. This is not surprising since as was discussed in Chapter 3, the calculated 10 group energy spectra fell slightly below the unfolded NaI results. The 39 group results agree very well with the values obtained from the measured NaI spectra except at some of the closer measurement locations where the effect of the in-silo scattered component is significant.

One source of error in the 10 group DOT results is the fact that the ground was not considered in these calculations. Instead, the lower boundary was treated as a vacuum. It has been estimated that the exclusion of the ground from these calculations causes an under-prediction of approximately 10%<sup>3</sup>.

#### 4.2.2 Comparison of 4 $\pi$ Geometry Results

As an independent verification of the HPIC measurements, an attempt was made to infer the 4 $\pi$  geometry exposure rate from the unfolded NaI spectra. This technique relies heavily upon the DOT results to calculate a geometry correction factor, C, which is defined as

$$C = \frac{\dot{X}(\text{collimated geometry})}{X(4\pi \text{ geometry})} \quad (4.2-2)$$

Therefore, the exposure rate that would have been measured by the NaI detector in 4 $\pi$  geometry,  $\dot{X}_{\text{NaI}}^{4\pi}$ , is given by

$$\dot{X}_{\text{NaI}}^{4\pi} = \frac{\dot{X}_{\text{NaI}}^{\text{coll.}}}{C} \quad (4.2-3)$$

where  $\dot{X}_{\text{NaI}}^{\text{coll}}$  is the exposure rate calculated from the unfolded NaI spectra (i.e., collimated geometry). In general, C is a function of source/detector distance and source configuration.

The calculation of C is very sensitive to any errors in normalization of the DOT calculated exposure rates. If the error in the magnitude of the results is identical for the collimated detector geometry results and the 4 $\pi$  values, then the error in the value of C obtained by

taking the ratio of these two quantities will be minimal. However, if the normalization error is different for the two calculated exposure rate values then the error incurred in the calculated value of C will be significant.

Three sets of C values were calculated in this analysis, one for each source configuration. The C's used in the inference of the unshielded  $4\pi$  exposure rates were calculated at 100 meter intervals by taking the ratio of the DOT calculated exposure rates for the collimated and  $4\pi$  geometry. The values of C used in the shielded configurations were calculated using DOT exposure rates for the shielded results. The results of these calculations are shown in Table 12. Quadratic interpolation was used between the values tabulated in Table 12 to obtain values for those source/detector distances at which measurements were taken.

Table 12. Calculated Geometry Correction Factors

Radial Distance (meters)	Shield Thickness		
	0.0	8"	16"
100	.559	.472	.499
200	.523	.455	.496
300	.505	.467	.454
400	.496	.461	.445
500	.486	.374	.424
600	.485	.347	-
700	.480	.313	-

The calculated and measured  $4\pi$  geometry exposure rates are shown in Fig. 41. Again, the solid line follows the trend of the 10 group results while the dotted line follows the 39 group predictions.

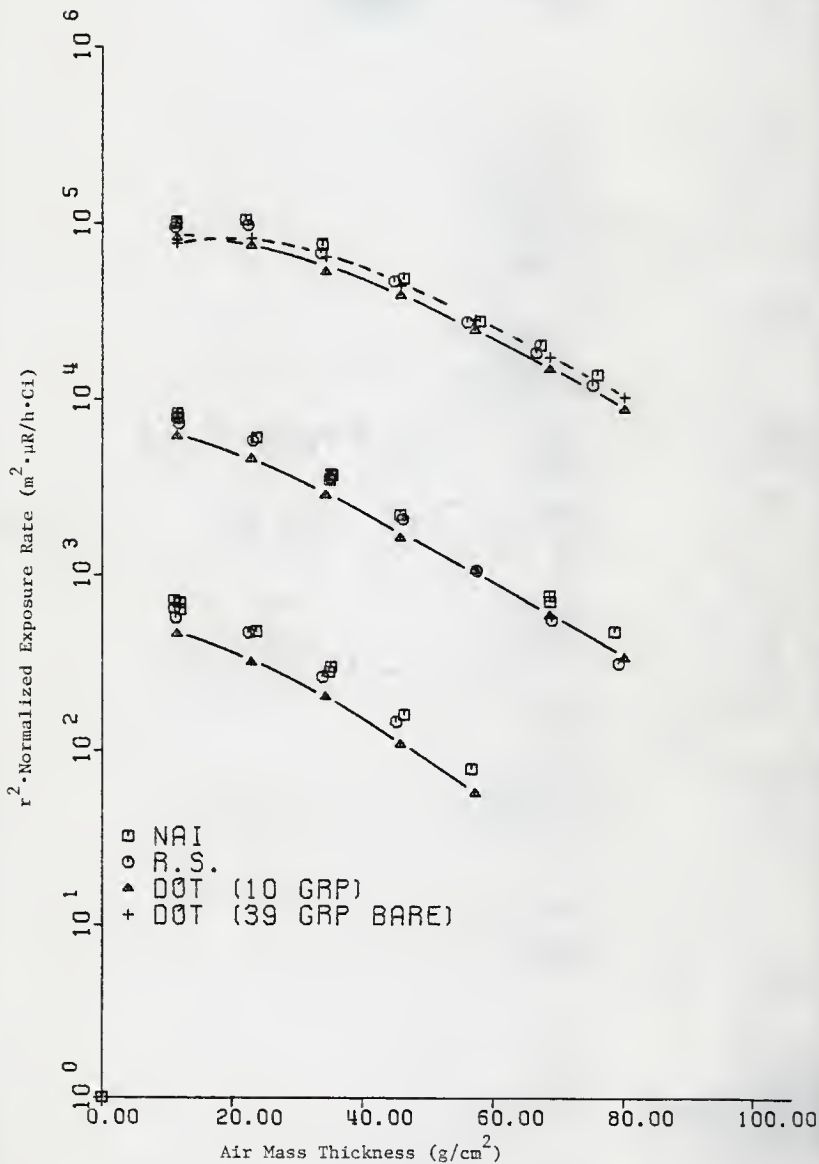


Fig. 41. Comparison of measured and calculated  $4\pi$  exposure rates.

The Reuter-Stokes data represents an average of at least two and at most six values. As in the collimated geometry results, the 10 group values underestimate the Reuter-Stokes HPIC values by approximately 10% at all locations for the unshielded configuration. This trend also occurs in the 16" shielded configuration results where the differences range from 20 to 25% at 100 and 400 meters, respectively.

The 39 group results start slightly lower than the 10 group values. An error of almost 20% is observed at 100 meters when the 39 group result is compared to the Reuter-Stokes datum. At 500 meters the 39 group value is approximately 4% higher than the measured value.

The trend observed in the 8" shield case is somewhat different. Although the DOT calculations still slightly underestimate the inferred NaI values, the Reuter-Stokes results are much lower than expected at 600 and 700 meters. A possible explanation for the sudden decrease in the measured exposure rate values is the terrain at the particular measurement positions. At both locations, the detector was positioned on a small ridge. At the 600 meter location, small valleys were situated on either side of the detector while at the 700 meter location, a rather large valley was positioned directly in front of the collimator opening. The absence of the earth-air interface in the vicinity of the detector resulted in a significant loss of ground scattered photons, and therefore an approximately 10%<sup>3</sup> reduction in the exposure rate.

The agreement between the Reuter-Stokes HPIC results and those values inferred from the unfolded NaI spectra is excellent. In most

cases the results are practically indistinguishable from each other. The only instances where there are significant differences between the two sets of values occur at 600 and 700 meters for the 8" shielded source configuration. Here it is observed that the NaI results continue the trend established by the values at the closer source/detector distances lending credibility to the estimated affect of ground-scattered photons on the total exposure rate. The angular distribution of the low energy, ground scattered photons could be such that the majority of them are shielded from the NaI detector and play an insignificant role in the collimated geometry results. The close agreement between these two sets of data makes a clear argument for the accuracy of the experimental results and the deficiency of the approximations used in the photon transport calculations.

The almost constant separation between the measured and calculated exposure rate values causes one to question the source strength values used in the normalization of the results to a unit source strength. Figure 42 presents the  $4\pi$  exposure rates obtained for the unshielded source configuration. Contained in Fig. 42 are the data shown in the top curve of Fig. 41, but now the sources used for the NaI measurements are identified. A comparison between the results obtained with the small source (10 Ci) and the medium source (250 Ci) is observable at 300 meters ( $\rho_r = 34.32 \text{ g/cm}^2$ ). Although there is a slight discrepancy between the values, it is certainly no larger than the uncertainty in the reproducibility of the results. The same comments are applicable to the comparison between the medium and big (3800 Ci) sources at

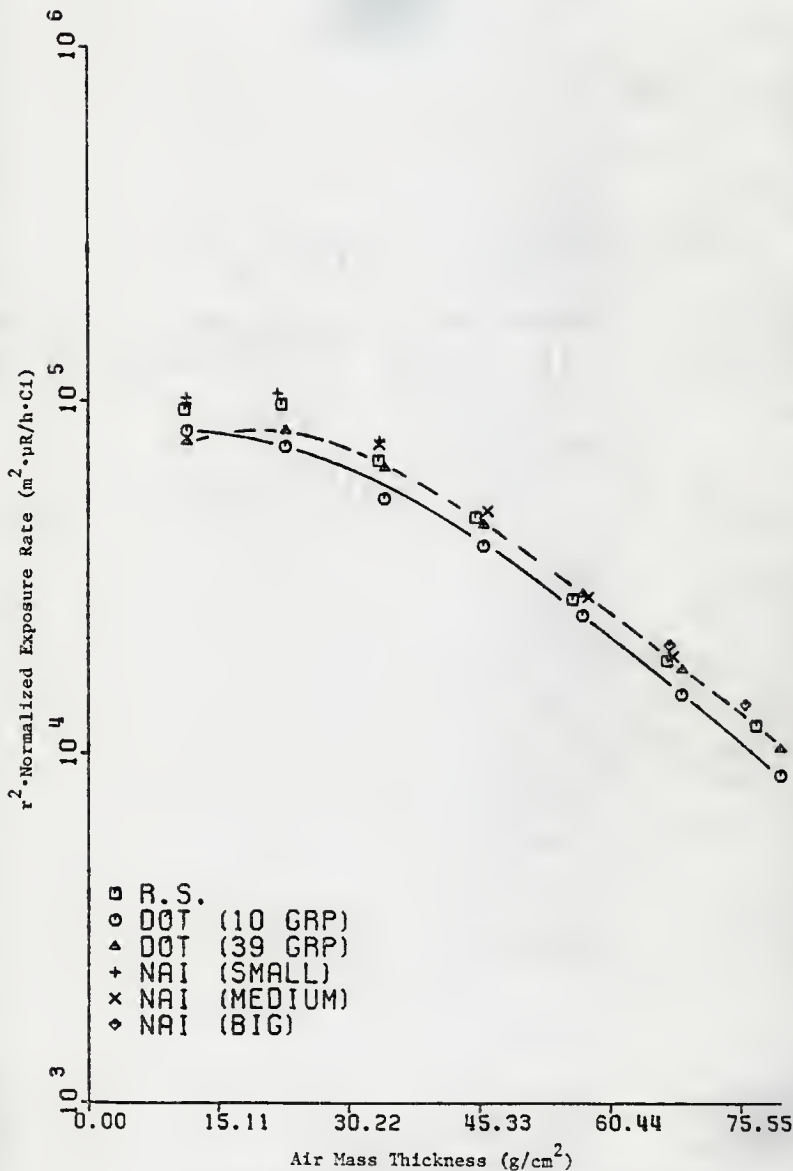


Fig. 42. Comparison of  $4\pi$  exposure rates for the unshielded source configuration showing sources used.

600 meters ( $\rho r = 68 \text{ g/cm}^2$ ). Thus, the discrepancies between the calculated and measured results apparently reflect a deficiency in the calculational method and not a normalization error.

The  $4\pi$  exposure rate values for the unshielded, 8", and 16" shielded source configurations are tabulated in Tables 13, 14, and 15, respectively.



Table 13A.  $4\pi$  Geometry NaI Exposure Rates for the Unshielded Source Configuration

Air Mass Thickness (g/cm <sup>2</sup> )	$r^2 \cdot \dot{X}$ (m <sup>2</sup> · $\mu$ R/h·Ci)
11.375	1.020 (5)*
11.340	9.859 (4)
22.001	1.047 (5)
33.754	7.676 (4)
33.740	7.536 (4)
46.224	4.868 (4)
58.873	2.786 (4)
67.620	1.889 (4)
67.207	2.032 (4)
75.987	1.377 (4)

\* 1.020 (5) =  $1.020 \times 10^5$

Table 13B.  $4\pi$  Geometry DOT Calculated Exposure Rates for the Unshielded Source Configuration

Air Mass Thickness (g/cm <sup>2</sup> )	$r^2 \cdot \dot{X}$ (m <sup>2</sup> · $\mu$ R/h·Ci)	
	(39 Group)	(10 Group)
11.44	7.668 (4) *	8.216 (4)
22.88	8.217 (4)	7.411 (4)
34.32	6.462 (4)	5.279 (4)
45.76	4.447 (4)	3.867 (4)
57.20	2.845 (4)	2.458 (4)
68.64	1.738 (4)	1.470 (4)
80.08	1.031 (4)	8.656 (3)

\* 7.668 (4) = 7.668 x 10<sup>4</sup>

Table 13C.  $4\pi$  Geometry Corrected HPIC Exposure Rate Measurements for the Unshielded Source Configuration

Air Mass Thickness (g/cm <sup>2</sup> )	$r^2 \cdot \dot{X}$ (m <sup>2</sup> ·μR/h-Ci)
11.58	9.282 (4) *
11.44	9.298 (4)
10.88	9.123 (4)
10.88	9.293 (4)
10.96	9.663 (4)
11.20	9.965 (4)
22.88	9.788 (4)
21.92	9.697 (4)
32.88	6.675 (4)
34.32	9.957 (4)
34.32	6.567 (4)
32.88	6.833 (4)
45.76	4.392 (4)
43.84	4.947 (4)
57.20	2.565 (4)
54.80	2.917 (4)
67.44	1.724 (4)
67.44	1.824 (4)
65.76	1.949 (4)
77.77	1.200 (4)
76.72	1.194 (4)

\* 9.282 (4) = 9.282 x 10<sup>4</sup>

Table 14A.  $4\pi$  Geometry NaI Exposure Rates for the 8" Shielded Source Configuration

Air Mass Thickness (g/cm <sup>2</sup> )	$r^2 \cdot \dot{X}$ (m <sup>2</sup> · $\mu$ R/h · Ci)
11.46	7.923 (3)*
11.57	8.249 (3)
11.68	7.696 (3)
23.71	6.007 (3)
35.08	3.729 (3)
34.68	3.444 (3)
35.28	3.700 (3)
45.73	2.175 (3)
57.67	1.263 (3)
68.68	6.994 (2)
68.60	7.585 (2)
78.59	4.718 (2)

$$*7.923 (3) = 7.823 \times 10^3$$

Table 14B.  $4\pi$  Geometry DOT Calculated Exposure Rates for the 8" Shielded Source Configuration

Air Mass Thickness (g/cm <sup>2</sup> )	$r^2 \cdot \dot{X}$ (m <sup>2</sup> · $\mu$ R/h · Ci)
11.44	6.092 (3)*
22.88	4.553 (3)
34.32	2.826 (3)
45.76	1.611 (3)
52.70	1.052 (3)
68.64	5.810 (2)
80.08	3.334 (2)

$$*6.092 (3) = 6.092 \times 10^3$$

Table 14C. Corrected HPIC Exposure Rate Measurements for the 8" Shielded Source Configuration

Air Mass Thickness g/cm <sup>2</sup>	$r^2 \cdot \dot{X}$ (m <sup>2</sup> ·μR/h·Ci)
11.08	6.853 (3)*
11.62	7.015 (3)
12.13	7.350 (3)
12.13	7.752 (3)
23.92	5.778 (3)
22.24	5.798 (3)
23.14	5.793 (3)
35.74	3.436 (3)
35.74	3.536 (3)
33.49	3.637 (3)
34.57	3.686 (3)
47.64	1.889 (3)
44.64	2.321 (3)
46.08	2.012 (3)
59.31	9.588 (2)
55.63	1.147 (3)
57.20	1.053 (3)
66.51	5.970 (2)
69.15	5.379 (2)
78.14	3.100 (2)
80.35	3.120 (2)

\*6.853 (3) = 6.853 x 10<sup>3</sup>

Table 15A.  $4\pi$  Geometry NaI Exposure Rates for the 16" Shielded Source Configuration

Air Mass Thickness (g/cm <sup>2</sup> )	$r^2 \cdot \dot{X}$ (m <sup>2</sup> · $\mu$ R/h·Ci)
10.99	7.136 (2)*
11.95	6.329 (2)
11.96	6.926 (2)
11.06	6.451 (2)
23.67	4.774 (2)
35.09	2.989 (2)
34.83	2.816 (2)
46.34	1.599 (2)
56.74	7.806 (1)
56.71	7.701 (1)
57.21	7.751 (1)

$$*7.136 (2) = 7.136 \times 10^2$$

Table 15B.  $4\pi$  Geometry DOT Calculated Exposure Rates for the 16" Shielded Source Configuration

Air Mass Thickness (g/cm <sup>2</sup> )	$r^2 \cdot \dot{X}$ (m <sup>2</sup> · $\mu$ R/h·Ci)
11.44	4.561 (2)*
22.88	3.162 (2)
34.32	2.007 (2)
45.76	1.077 (2)
57.20	5.638 (1)

$$*4.561 (2) = 4.561 \times 10^2$$

Table 15C.  $4\pi$  Geometry Corrected HPIC Exposure Rate Measurements for the 16" Shielded Source Configuration

Air Mass Thickness (g/cm <sup>2</sup> )	$r^2 \cdot \dot{X}$ (m <sup>2</sup> · $\mu$ R/h·Ci)
11.10	5.807 (2)*
11.18	5.544 (2)
11.42	5.588 (2)
22.19	4.702 (2)
22.35	4.621 (2)
23.01	4.669 (2)
33.29	2.732 (2)
33.64	2.583 (2)
34.61	2.523 (2)
44.52	1.589 (2)
44.83	1.473 (2)
46.15	1.281 (2)

\*5.807 (2) = 5.807 x 10<sup>2</sup>

## 5.0 Conclusions and Suggestions for Further Study

The data collected in this experiment represent a significant contribution to the body of knowledge in the area of radiation shielding. These data should prove invaluable in the development of new methods and the verification of old techniques for predicting skyshine exposure rates. Furthermore, the results of this experiment may be used directly as design data in the construction of nuclear facilities where skyshine radiation is of concern.

The SEGO unfolding code used in the analysis of the experimental data appeared to work very well on the smooth spectra encountered. The comparatively small number of experimentally determined response functions necessary to define the Hyodo response surface simplified the implementation and use of this technique. The unfolded results also seemed fairly insensitive to minor changes in the response matrix. The only problem encountered during the spectral unfolding was the iodine-escape peak which had to be artificially suppressed since the response surface used did not include this feature.

The agreement between the unfolded NaI spectra and the calculated spectra was, in general, very good. Excellent results were obtained from the 39 group calculations both with regard to spectral shape and normalization. However, the 10 group calculations were somewhat deficient in describing the spectral shape and as a consequence underpredicted the total exposure rate by approximately 20 to 30%.



The excellent agreement between the corrected Reuter-Stokes high pressure ionization chamber (HPIC) measurements and the collapsed NaI spectra, both independent determinations of the total exposure rate, lends credibility both to the approximations used in the calculation of the energy dependence correction factor,  $\bar{F}$ , and to the accuracy of the experimental measurements themselves.

Several portions of this experiment certainly require additional analysis. Certainly more refined transport calculations should be performed in an effort to resolve the apparent discrepancies between the calculated coarse group results and the measured values. The effect of the vacuum boundary condition used as an approximation for the actual ground interface in these transport calculations should be studied in some detail. Additional verification of the  $\bar{F}$  calculational procedures used in this study could be obtained by performing the 39 group calculations for the shielded source configurations.

Further analysis of the spectral unfolding technique would undoubtedly prove interesting. Verification of the unfolded results could possibly be obtained through the use of a different unfolding procedure. There also appears to be a slight philosophical weakness in the underlying assumptions of the SEGO code. As formulated in Eq. (3.1-6), the system resolution is a function of the incident photon energy alone while physically the smoothing is a function of the amount of energy actually deposited in the crystal. Thus Eq. (3.1-6) should read

$$R_i(E') = \int_{\Delta E_i} dE \int_0^{E \max} dE'' U(E', E'') S(E'', E) \quad i=1, 2, \dots, N. \quad (5.0-1)$$

An effort should be made to reconcile the two approaches.

Finally, much work remains in the development of accurate point kernel techniques to predict skyshine exposure rates. The use of a buildup factor in a finite media problem will inevitably lead to some error as the source/detector distance increases. Perhaps a more appropriate buildup factor could be constructed from the available transport theory results.

### Acknowledgement

The author wishes to express his sincere appreciation to Dr. J. K. Shultis and Dr. R. E. Faw for their help and guidance during the course of this work. The support of the staff and faculty of the Department of Nuclear Engineering is also gratefully acknowledged. Special thanks are due to Mr. M. L. Roseberry for his organization and supervision during the experimental portion of this endeavor.

The author also wishes to thank his wife for enduring the difficulties associated with completing a work of this magnitude. Her presence, support and encouragement were necessary factors in order to bring this work to a close.

## References

1. "Summary of an Interim Report Presented by the Study Committee on Air-Scattered Gamma Rays in Nuclear Facilities," Nuclear Safety Research Association (March, 1977).
2. J. K. Shultis, C. E. Clifford, R. E. Faw, W. Yoon, M. Roseberry and R. Nason, "A Benchmark Gamma-Ray Skyshine Experiment: Measurements and Calculations," American Nuclear Society Transactions, Volume 28, San Diego, California (June, 1978).
3. C. E. Clifford, W. Y. Yoon, R. E. Faw and J. K. Shultis, "Skyshine Benchmark Experiment," RRA-T78802-1 and 2, Radiation Research Associates, Fort Worth, Texas (1978).
4. M. H. Young and W. R. Burrus, "A Digital Filter for Unfolding Pulse-Height Distributions," Nucl. Instr. Methods, 62, 82 (1968).
5. W. A. Rhoades and F. R. Mynatt, "The DOT-3 Two-Dimensional, Discrete Ordinates Transport Code," CRNL-TM-4280 (1973).
6. J. K. Shultis and R. E. Faw, "System Integration and Calibration of the Canberra 8180 Multichannel Analyzer and the Associated NaI Detector," KSU Skyshine Report No. 1 (1977).
7. J. K. Shultis and R. E. Faw, "Description of the NaI Detector Cavity and Collimator Used in Skyshine Spectral Measurements," KSU Skyshine Report No. 7 (1977).
8. J. K. Shultis and R. E. Faw, "Design and Construction of the Source Silo and Associated Components," KSU Skyshine Report No. 8 (1977).
9. G. F. Knoll, Radiation Detection and Measurement, John Wiley and Sons Publishing Co., New York (1979).
10. R. L. Heath, "Scintillation Spectrometry Gamma-Ray Spectrum Catalogue," IDO-16880-1 (August, 1964).
11. W. J. Snow, "The Response of Monoenergetic Gamma Rays in Finite Media," ANL-3714.
12. C. D. Zerby and H. S. Moran, "Calculation of the Pulse-Height Response of NaI(Tl) Scintillation Counters," ORNL-3169 (January, 1962).
13. W. T. Urban, "Monte Carlo Calculation of the Response of a Collimated Sodium Iodide Gamma-Ray Spectrometer to Plane Sources of Radiation," Ph.D. Thesis, Kansas State University, Manhattan, Kansas (1971).

## References - continued

14. R. L. Heath, "Computer Techniques for the Analysis of Gamma-Ray Spectra with NaI and Lithium-Ion Drifted Germanium Detectors," Nucl. Inst. Methods, 43, 209 (1966).
15. J. A. Baran, "Reflection of Co-60 Gamma Rays from Concrete," Ph.D. Thesis, Kansas State University, Manhattan, Kansas (1968).
16. H. Kendrick and S. M. Sperling, "An Introduction to the Principles and Use of the FERDOR Unfolding Code," GA-9882 (1970).
17. W. R. Burrus, "Utilization of 'A Priori' Information by Means of Mathematical Programming in the Statistical Interpretation of Measured Distributions," ORNL-3743 (1965).
18. F. G. Perey, "Least-Squares Dosimetry Unfolding," ORNL/TM-6062 (1977).
19. W. J. Price, Nuclear Radiation Detection, McGraw-Hill Book Company, New York (1964).
20. E. Storm and H. I. Israel, "Photon Cross Sections from 1 keV to 100 MeV for Elements Z=1 to Z=100," LA-3753 (1967).
21. Private Communication with H. Kadatoni, Century Research Corporation, Japan (1978).
22. W. W. Engle, Jr., "A User's Manual for ANISN, A One-Dimensional Discrete Ordinate Transport Code with Anisotropic Scattering," RSIC-CCCB2/ANISN.
23. J. K. Shultis and R. E. Faw, "High Pressure Ion Chamber Measurements of <sup>60</sup>Co Gamma-Ray Skyshine Exposure Rates," KSU Skyshine Report No. 10 (1977).
24. Reuter-Stokes Instruments, Inc., "Operational Manual: RSS-111 Area Monitor System," 18530 South Miles Parkway, Cleveland, Ohio.
25. J. A. DeCampo, H. L. Beck and P. D. Raft, "High Pressure Argon Ion Chamber Systems for the Measurement of Environmental Exposure Rates," HASL-260 (1972).
26. K. Z. Morgan and J. E. Turner, Principles of Radiation Protection, Robert E. Drieger Publishing Co., New York (1973).
27. H. R. Byers, General Meteorology, McGraw-Hill Book Co. (1959).

ANALYSIS OF SKYSHINE SPECTRAL MEASUREMENTS

by

Randall Robert Nason

B.S., Kansas State University, 1977

---

AN ABSTRACT OF A MASTER'S THESIS

submitted in partial fulfillment of the  
requirements for the degree

MASTER OF SCIENCE

Department of Nuclear Engineering

KANSAS STATE UNIVERSITY

Manhattan, Kansas

1979

## Abstract

A benchmark gamma-ray skyshine experiment was performed to obtain skyshine exposure rate and spectral data against which numerical models may be compared. To obtain skyshine radiation fields of measureable intensity over the 700 meter measurement baseline, three  $^{60}\text{Co}$  sources were used of nominal strengths 10, 250, and 5000 Ci. Three source configurations were employed; first with the source radiation collimated into a vertical conical beam and then with the sources covered with eight and sixteen inches of concrete.

Spectral measurements were made at 100 meter intervals from the Co-60 source with a collimated NaI(Tl) scintillation spectrometer. The detector was housed in an eight ton collimator-shield assembly and mounted on a semi-trailer. Total skyshine exposure rates were also measured over the 700 meter baseline with a ten-inch diameter, 25 atmosphere argon filled Reuter-Stokes high pressure ionization chamber.

The measured NaI spectra were unfolded with the SEGO code using experimentally determined response functions. These unfolded spectral results are compared with results of detailed DOT-3.5 transport calculations and found to agree to within 20%.

A factor was calculated using the unfolded NaI spectra to correct the Reuter-Stokes detector measurements for its non-ideal energy response. Additionally, the unfolded NaI spectra are used to obtain an independent determination of the total skyshine exposure rate. These independently

measured values agreed to within 5-10%, while values calculated by the DOT code were consistently 10 to 20% lower.